Chemical and Electrochemical Behavior of Graphene-Covered Silicon Photoanodes

Thesis by

Adam Christopher Nielander

In Partial Fulfillment of the Requirements for the Degree of

Doctor of Philosophy

Caltech

California Institute of Technology

Pasadena, CA, USA

2016

(Defended January 11th, 2016)

To Mom, Dad and Sister

Acknowledgements

The number of people that I need to acknowledge for helping me reach a point where I could write an acknowledgements section for a Ph.D thesis is almost overwhelming. Of course, most of those people probably weren't expecting this day to ever actually arrive, so if I miss someone by the end of this, I suspect no one will be the wiser.

First, I need to thank my committee. I can say with certainty that without their signatures, these past five years would not have had quite the same purpose. So to Harry, Bruce, and Mitchio: thank you for your support over the past five years. I know you are all busy people, and I truly appreciate you taking the time to help me progress through my graduate career. Harry, you have been a great committee chair, and you have always supported me and my career plans wonderfully. I appreciate all the advice you have given me as well all the times you let me tag along with your group for a drink or dinner in the BI or at the Ath. Bruce, that you have attained the success that you have in science and life, yet still manage to find time to fix the water chiller as well as explain charge transfer at metal-electrolyte interfaces and Auger spectroscopy to errant graduate students, is a real inspiration and I hope someday I can be half as valuable to a community as you are to ours.

The number of great mentors I've had during my time at Caltech has been extraordinary. I picked up a habit early in my career of latching on to postdocs, and in particular, I stole a significant amount of time from Drs. Nick Strandwitz, Shane Ardo, Ron Grimm, and Rob Coridan that they certainly could have put to better use than talking to me. Nick, thank you for answering all my materials science questions when I didn't know the first thing about materials science. And thanks for getting me starting with Cold Fusion softball and preventing me from getting into the first fight of my life on the softball field. Shane, I'm not sure anyone has put more effort into wearing out the white boards in the halls of Noyes than us. Thanks for listening to me when I needed to work through ideas and showing me why I was wrong so many times. Ron, I'll always aspire to be as good at building things as you are. You really have a gift, and I appreciate you sharing as much as you could with someone with hands like mine. Rob, your critical thinking ability is second to none. I attribute this to your studies in a real scientific field (physics), but I appreciate you coming down to imbue your knowledge on the chemists of the world. I still wake up in the middle of the night with the fear that someone is going to ask for one more round of corrections on that paper. I also had a wonderful amount of help from Drs. Leslie O'Leary, Liz Santori, James McKone, and Emily Warren. To each of you: thank you for making me feel like a welcome member of the group when I joined and for being my role models as to how a graduate student should act. I'll never forget the overwhelming feeling when you all graduated that the group had basically fallen apart. I hope I am lucky enough to stay in touch with all of you as our careers progress. Mita, thanks for all your advice on how to keep my career moving forward and for being a real role model in terms of how to act as a real scientist. Matt Bierman and Nick Petrone, thank you for your help and advance on how to work with graphene. Finally, I would be remiss if I didn't mention my advisor and my graduate student mentor from UVa, Dean Harman and Dan Harrison. I wouldn't have made it here without your support and advice.

I’ve also learned as much from the people who I was ostensibly supposed to help learn as those who helped me. Suyeon, you were my first SURF. I clearly had no clue how to mentor an undergrad when we were together, but you stuck it out anyway and I really appreciate all your hard work. Jackie, I swiped you from Heather, which ended up being one of the better decisions I made as a graduate student. Thank you for listening to me ramble on about band bending and electrochemistry; I’m sorry for trying to change your project without your prior written consent. I’d like to think that I had some role in shaping your abilities at least as a 2B, and I look forward to watching your career progress at Berkeley. Annelise, I’m mostly confident that I would have gone insane and never graduated if you hadn’t joined our project. I’m fully confident that you are going to do some very exciting work with graphene, or any project you end up pursuing, and I think the lab is going to be in your hands sooner than you realize.

Both in and out of the lab, I was lucky to have a number of amazing colleagues. Joseph Beardslee, your ability to fix the XPS under any circumstance will always be legendary, and I couldn’t have asked for a better Portal 2 partner. Matt Shaner, what can I say about you that hasn’t already been said? Our semiconductor discussions were always illuminating, but more than that I will always envy your ability to pursue your interests so intensely. Thanks for including me on some of your adventures. Ben, Jacob, and Adam, I really am sorry for being so bad at LoL, but thanks for letting me play anyway and for always being good roommates. Matt Kovach, Matt Chao, Tom Teets, and the rest of the Buckets, we showed some real hustle out on the basketball court. Guy, you are the ultimate glue player on and off the court. Dan Torelli, take care of Cold Fusion for me. Chris Roske, you are an amazing scientist and I can’t wait to see what you end up doing with your talent. So many of my colleagues in the Lewis group have been instrumental in my growth as a scientist. In no particular order, Matt McDowell, Ke Sun, CX, Fan Yang, Jesus Velasquez, Jonathan Thompson, Azhar Carim, Michael Lichterman, Fadl Saadi, Sonja Francis, Xinghao Zhou, Noah Plymale, Josh Wiensch, Stefan Omelchenko, Amanda Shing, Shu Hu, Paul Nunez, Chance Crompton, Sisir Yalamanchili, Ethan Simonoff, Victoria Dix, Ivan Moreno, Jingjing Jiang, and Kyra Lee, thanks to all of you for helping make the group run the way it does. Finally, to Aaron, Wes, and James: we spent an inordinate amount of time together over the past couple years. You guys were there for me when times were good and when they were tough. I will always reflect fondly on our white board discussions both in the Orange room and at home and I hope we find a way to continue them as we go our separate directions. Maybe we can set up a whiteboard at a blackjack table in Vegas.

Of course, there are two key people who have shaped my time at Caltech more than anyone else. The first is Barbara Miralles. Barbara, you are the glue that keeps our team together and I can only imagine the disaster that the Lewis group would be without you keeping us in order. The second is, of course, Nate. Nate: You have lived up to the hype. You always supported me both when times were good and when times were bad, as well as in the beginning and at the end. Your ability to consistently think logically from the start of a problem to the end is an inspiration, and I hope one day I'm lucky enough to run my group the same way you run yours. I'm sorry we didn't start playing tennis sooner, but hopefully we haven't hit for the last time.

Finally, I need to thank my friends and family here and home. To Brian, Alex, Alex, Chris, Aaron, Adam, Eddie, and Julien: you guys have always been there for me whether I was living next door or 3,000 miles away, and dealing with the trials of becoming an adult would have been impossible with you all. I'll see you in Vegas. To Grover: you are a dog. You can't read this, but I hope somehow you know that the love you have shown me has helped me through many hard times. To my mom, dad, and sister: thank you for all of your love and support over the years, both on the phone and with trips out here. Dad, thanks for convincing me to stay out in California when I was ready to move home after a week, and Mom, thanks for reminding me that if I had to come home that my life wouldn't actually collapse. In the end, it looks like I am going to cross the finish line.

As an undergraduate, I never understood why the graduate students seemed to be so frustrated all the time. Now I do. That a Ph.D is an extended lesson in psychology is truer than I could have possibly imagined, and I certainly would not have earned mine without the help of each of you and many others. You will forever have my gratitude.

-Adam

Abstract

This dissertation describes efforts over the last five years to develop protective layers for semiconductor photoelectrodes based on monolayer or few-layer graphene sheets. Graphene is an attractive candidate for a protective layer because of its known chemical inertness, transparency, ease of deposition, and limited number of electronic states. Monolayer graphene was found to effectively inhibit loss of photocurrent over 1000 seconds at n-Si/aqueous electrolyte interfaces that exhibit total loss over photocurrent over 100 seconds. Further, the presence of graphene was found to effect only partial Fermi level pinning at the Si/graphene interface with respect to a range of nonaqueous electrolytes. Fluorination of graphene was found to extend the stability imparted on n-Si by the monolayer sheet in aqueous $Fe(CN)_6^{3-/4-}$ electrolyte to over 100,000 seconds. It was demonstrated that the stability of the photocurrent of n-Si/fluorinated graphene/aqueous electrolyte interfaces relative to n-Si/aqueous electrolyte interfaces is likely attributable to the inhibition of oxidation of the silicon surface.

This dissertation also relates efforts to describe and define terminology relevant to the field of photoelectrochemistry and solar fuels production. Terminology describing varying interfaces employed in electrochemical solar fuels devices are defined, and the research challenges associated with each are discussed. Methods for determining the efficiency of varying photoelectrochemical and solar-fuel-producing cells from the current-voltage behavior of the individual components of such a device without requiring the device be constructed are described, and a range of commonly employed performance metrics are explored.

Contents

List of Figures and Schemes

Chapter 2

Chapter 3

Chapter 4

Chapter 5

Chapter 6

List of Tables

Chapter 3

Chapter 4

Chapter 5

Chapter 1

Introduction

1.1 Purpose and Scope

This dissertation describes my research efforts in the field of photoelectrochemistry in the Lewis group between January 2011 through December 2015. It has been written in part to fulfill the requirements of a doctoral degree in chemistry from the California Institute of Technology. It has also been written with the hope that future researchers in the fields of photoelectrochemistry and solar fuels find its contents useful in furthering their own work; it also serves as an archive of the research that I was unable to publish during my time at Caltech and as a mechanism by which I hope to convey my opinions on the strengths and well as weaknesses of the work that I have performed.

Chapter 1 serves as a brief overview of the rest of this dissertation and includes a discussion of the work described in Chapters 2-5 from a personal viewpoint.

Chapters 2 and 3 describe my efforts to address controversial topics in the field of photoelectrochemistry. Chapter 2 focuses on defining nomenclature and taxonomy sufficient to differentiate solar fuels generator devices into two groups:

1. Those that are essentially photovoltaic devices whose electrochemical properties are independent of the electrolyte with which they operate.
2. Those that are photoelectrochemical devices whose properties and efficiency actively depend on the nature of the electrolyte environment in which they operate.

Because these different devices have varying advantages as well as research challenges associated with them, identifying a device as such allows researchers to quickly understand the context in which new systems of either variety should be viewed. Chapter 3 discusses methods necessary to determine the efficiency of a hypothetical solar fuels generator device without requiring that the device of interest actually be constructed. Because actual device construction entails significant engineering efforts, the ability to determine the efficiency of a hypothetical system facilitates comparison of the efficacy of new components in solar fuels generating devices to previously reported components without concern that inconsistent engineering may prevent a one-to-one comparison. The bulk of the work in both chapters was published in 2015 in *Energy and Environmental Science*.

Chapters 4 and 5 describe my efforts to understand the photoelectrochemical activity of graphene-covered silicon photoelectrodes. In particular, chapter 4 discusses the activity of pristine graphene monolayers on n-Si electrodes and demonstrates that stability in aqueous electrolyte is imparted to n-Si electrodes by the presence of a graphene protective layer. However, this stability is only demonstrated over 1,000 seconds, as demonstration of further stability was hindered by inconsistent results.

Chapter 5 discusses the related photoelectrochemical behavior of fluorinated graphene (F-Gr) on n-Si electrodes. The fluorination of graphene was found to improve the stability of the photoelectrochemical activity of F-Gr-covered n-Si surfaces in aqueous electrolyte to over 100,000 seconds, representing a two order-of-magnitude increase over pristine graphene. The bulk of the work described in chapter 4 was published in *The Journal of the American Chemical Society* in 2013 and the work in Chapter 5 is currently prepared for submission to peer review as of January 2016.

Chapter 6 reviews a number of additional efforts that I undertook that, because of incompleteness or lack of reproducibility, have yet to be prepared for peer review. These efforts include the following: work to understand the effect of multilayer graphene at Si interfaces, demonstration of the use of pristine graphene monolayers to prevent silicide formation, a survey of efforts to understand the impurities left behind by different graphene transfer methods, and a brief foray into the use of ALD to modify pristine graphene surfaces. I believe each of these, with sufficient care, are worthy of future efforts, and I hope chapter 6 can serve as a starting point for other researchers in this regard.

1.2 Personal Summary

The vast majority of the experimental work that I have performed in the Lewis group has related to understanding the chemical and photoelectrochemical behavior of n-type silicon photoanodes covered by monolayer sheets of graphene. The idea for this project was originally formulated by Nate just prior to my arrival at Caltech, and I began work on it in conjunction with a postdoc in the Lewis group and a graduate student at Columbia University, Matt Bierman and Nick Petrone, in May of 2011 after four months of work on measuring the kinetics of the surface reaction on silicon surfaces.

This project immediately proved to be promising, as n-Si electrodes covered by monolayer graphene showed significantly improved stability in aqueous electrolytes relative to uncovered n-Si electrodes. Furthermore, it was clear that the graphene did not fully pin the Fermi level of the silicon surface relative to nonaqueous redox couples. This was particularly exciting, as it suggested that graphene might be an ideal protective layer for a range of semiconductors in a photoelectrochemical motif since the graphene Fermi level could be modified by modification of the electrochemical potential of the electrolyte solution. With this in mind, another postdoc in our group, Fan Yang, began working on understanding the photoelectrochemical behavior of graphene-covered GaAs surfaces in aqueous electrolyte. While graphene did also inhibit deleterious reactions at the GaAs surface in contact with aqueous electrolyte, the protective ability of graphene on GaAs was limited in comparison to Si due to corrosion of GaAs at graphene imperfections leading to undercutting and eventual loss of graphene from the surface. This was in comparison to the passivation of Si that occurred at graphene imperfections.

However, despite the success that we found using graphene as a protective layer for silicon surfaces, problems existed. Specifically, the stability imparted by graphene to the Si was inconsistent from batch-to-batch of CVD grown graphene. This made further study of this interface challenging as the fabrication time per electrode was high. I tried a number of avenues to solve this issue. Among them, Ron Grimm and I built our own CVD chamber to grown graphene in an attempt to control the quality of the graphene employed in these experiments. Additionally, extensive effort was poured into understanding the nature of impurities and imperfections at the Si/graphene interface using Raman and XP spectroscopy. Unfortunately, in spite of these efforts, inconsistent results, particularly with regard to the imparted stability by graphene coverage on Si, is the major limiting factor in further studying graphene/Si interfaces in photoelectrochemical devices. This is perhaps not surprising as we are working with single-atom thick sheets of material in a non-cleanroom environment; however, based on the promising results that I have observed, I believe that these limitations are purely practical in nature. In retrospect, focusing on fabrication of micro- or ultramicroelectrodes of graphene-on-silicon surfaces via lithographic methods in an attempt to isolate a pristine, defect-free, impurity-free, graphene/silicon interface would have been a rational decision.

Concurrently with this work, I embarked on understanding the details of the field of photoelectrochemistry, which eventually led to my collaboration with Nate, Matt Shaner, and Rob Coridan, on the work that is discussed in chapters 4 and 5. Writing these papers was extremely satisfying as it forced us to carefully evaluate our understanding of the underpinnings of our field as well as provide a guide for researchers new to the field to orient themselves with.

Meanwhile, two enterprising graduate students, Chris Roske and Annelise Thompson, came up with the idea that perhaps fluorination of the graphene surface would improve its performance both in terms of protection of silicon from oxidation as well as the quality of rectification and charge separation at the interface. As related in chapter 5, we found that fluorination of graphene that otherwise was ineffective as a protective layer for Si allowed for protection of underlying silicon in aqueous solution. This relieved some, but not all, of the problems associated with the inconsistencies we had found with graphene. Furthermore, Jackie Maslyn demonstrated that these fluorinated graphene surfaces were capable of acting as physical barriers to prevent other deleterious reactions at the semiconductor surface as well, including the formation of metal silicides during evaporation of metals onto Si surfaces. As of January 2016, Annelise is continuing to try and understand the advantages and limitations, as well as the fundamental properties, of 2D materials at semiconductor/electrolyte interfaces.

Chapter 2

A Taxonomy of Solar Fuels Generators

2.1 Introduction and Background

A number of approaches to solar-fuels generation are being developed, each of which has associated advantages and challenges. Many of these solar fuels generators are identified as “photoelectrochemical cells” even though these systems collectively operate based on a suite of fundamentally different physical principles. To facilitate appropriate comparisons between solar fuels generators, as well as to enable concise and consistent identification of the state-of-the-art for designs based on comparable operating principles, we have developed a taxonomy and nomenclature for solar fuels generators based on the source of the asymmetry that separates photogenerated electrons and holes. Three basic device types have been identified: photovoltaic cells, photoelectrochemical cells, and particulate/molecular photocatalysts. We outline the advantages and technological challenges associated with each type, and provide illustrative examples for each approach as well as for hybrid approaches.

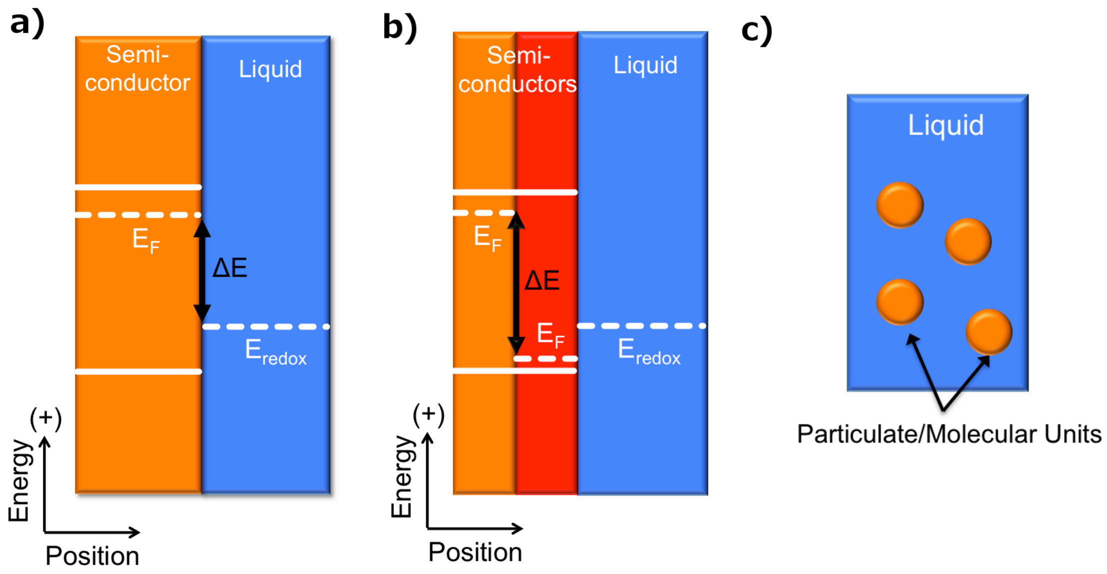

Figure 2.1: Illustrations of the different categories of solar fuels generators. a) Semiconductor/electrolyte junction in the dark and prior to equilibration in which the photovoltage and photocurrent are determined in whole or in part by the difference between Fermi level of the semiconductor (E_F) and the electrochemical potential of the electrolyte solution (E_{redox}), denoted as ΔE. b) Semiconductor buried junction in the dark and prior to equilibration in which the photovoltage and photocurrent are determined by the difference between the Fermi levels (E_F) of the two solid-state contacting phases (ΔE), shown here as two semiconductors. The ΔE is independent of any difference between the Fermi level of the solid contacting the electrolyte and the electrochemical potential of the electrolyte. The highly doped phase (in red) allows for ohmic contact between it and the contacting electrolyte phase. c) Particulate/Molecular photocatalyts suspended or dissolved in solution. Each unit individually absorbs light, generates excited carriers, and effects the desired chemical reactions at the particulate/molecular electrolyte interface.

The development of an artificial photosynthetic process, whereby the energy from sunlight is captured and stored in the chemical bonds of a fuel, has been an active area of research for decades. This field of research, however, has recently undergone rapid expansion due to the promise of a scalable solar fuels generator that would provide a carbon-neutral source of energy capable of addressing concerns about the impact of carbon emissions on the climate while providing a measure of environmental and energy security. Researchers have developed a diverse set of designs for solar fuels generators (Figure 2.1), each of which presents unique challenges associated with the research and development required to obtain a fully operational system. Furthermore, the maturity of the technologies being implemented in the various designs varies widely. Despite these differences, a variety of solar fuels generators are often grouped together and denoted as "photoelectrochemical cells". The focus of this chapter is to establish a differentiating nomenclature and taxonomy for solar fuels generators that clearly identify the principles underlying the designs. We hope that adoption of this taxonomy (Scheme 2.I) will bring clarity and precision to discussions and comparisons of solar fuels devices while facilitating concise and consistent identification of the research challenges and state-of-the-art for each type of system.

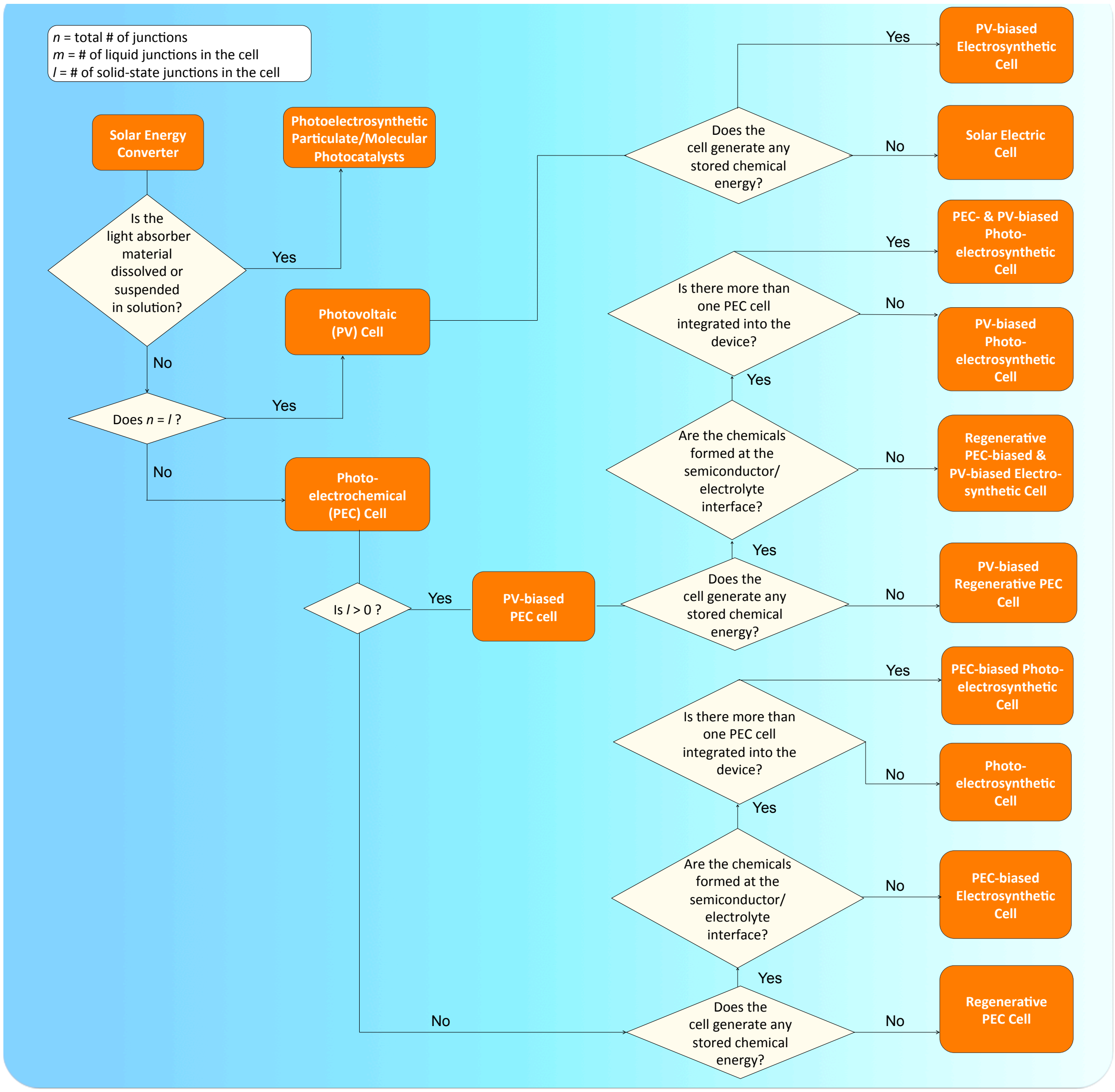

Scheme 2.1: A taxonomy for the classification of solar cells and solar fuels generators. For a device of interest, identify *n* (total number of junctions), *m* (number of semiconductor/electrolyte junctions), and *l* (number of buried junctions), then proceed through the flow chart to determine the appropriate name for the device.

All solar fuels generators require an electrical asymmetry to separate and transport photogenerated charge carriers vectorially.[1-4] Without vectorial separation and transport, the charge carriers, and thus the chemical products, would have no net directionality and thus would undergo no net separation. Therefore, deleterious recombination of charge carriers and/or a loss of chemical potential in the resulting fuel/oxidant mixture would result. The required vectorial separation can be effected by chemical and/or electrical potential gradients as well as by kinetic asymmetries at the interface between two unlike materials.[1-4] We refer to this interface as a 'junction'. We note that our usage of the term "junction" differentiates such an interface from an interface between two unlike materials that does not result in an asymmetry which produces a vectorial charge separation.[5] We propose that the various solar-fuels generators can be differentiated at a fundamental level based on the underlying principles used to accomplish vectorial charge separation and by the method in which the separated charge is used to effect the synthesis of chemical fuels.

2.2 Photovoltaic Cells

One fundamentally identifiable approach to charge separation in solar fuels devices is through the use of solid-state, or buried, junctions. Buried junctions are exclusively formed at the interface between two electronic conductors (as opposed to ionic conductors*, vide infra*) and are the basis for the operation of *photovoltaic* (PV) *cells* (Figure 2.2a).[6-8] In a device utilizing a buried junction, the photovoltage and photocurrent produced in the presence of illumination arise from charge separation mediated by a difference in electrochemical potential (Figure 2.1b) and/or by a difference in charge-transfer kinetics between two unlike solids that are in mutual electrical contact.

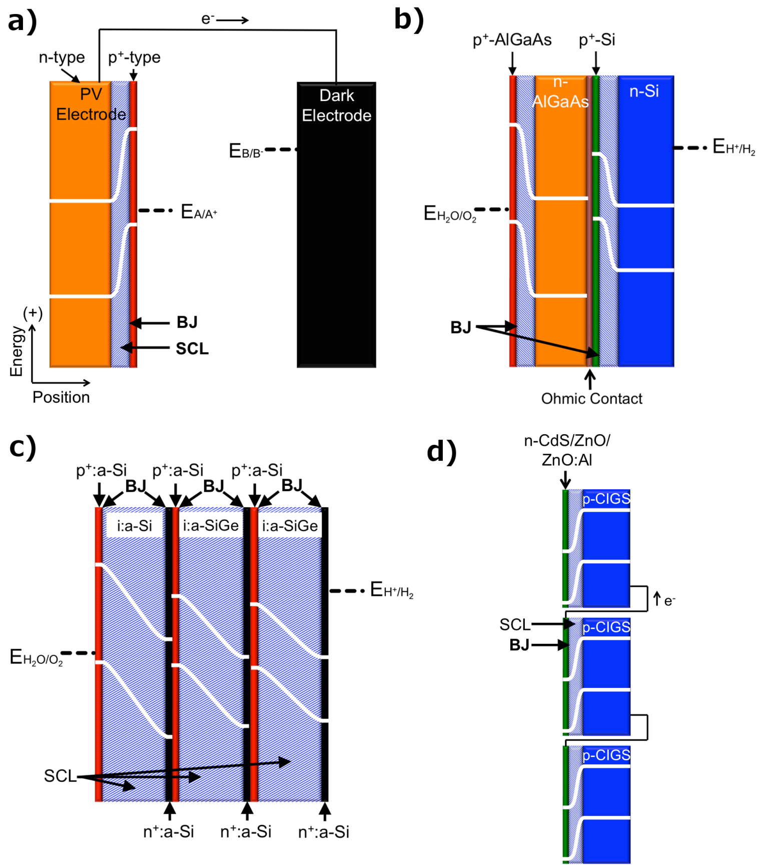

Figure 2.2: Illustrations of photovoltaic cells in the dark after equilibration, with the physical position of the buried junction (BJ), and the electric potentials of the conduction and valence bands shown in each diagram. The expected direction of electron flow under illumination is also indicated. a) A general photovoltaic electrode in a complete photovoltaic cell with generic half reactions at each electrode. b) An example of a PV-biased electrosynthetic cell that uses a monolithic tandem junction cell made of AlGaAs/GaAs coupled to Pt and RuO_2 electrocatalysts (not shown) to split water. c) An example of a PV-biased electrosynthetic cell that uses a monolithic triple junction cell made of amorphous hydrogenated Si and alloys with Ge, which has been coupled to hydrogen- and oxygen-evolution catalysts (not shown) to split water. d) A recent example of a PV-biased electrosynthetic cell that uses three separate side-by-side $CuInGaSe_2$ single-junction cells coupled to electrocatalysts (not shown) to split water.

The photocurrent vs. voltage behavior of a PV cell is independent of the character of any solid/electrolyte interfaces in the system. Therefore, measurements of the photocurrent-voltage characteristics of the PV cell can be performed independently of any electrochemical reaction, and can be used in concert with the current-voltage characteristics of various electrocatalysts to accurately predict the performance of a complete solar fuels generator that is based on a PV cell. PV cells will also produce the identical photocurrent-voltage behavior when both terminals of the device are contacted with wires connected to electrocatalysts vs. when all of the components of the structure (light absorbers and electrocatalysts) are integrated, contacted intimately, and immersed in an electrolyte solution. The operating principles of photovoltaic electrodes have been well documented for incorporation into full PV cells that either produce electricity or fuels.[3]

PV cells that produce electricity are referred to as *solar electric cells* and are widely available commercially. PV cells that produce fuels are referred to as *PV-biased electrosynthetic cells* and can consist of any number of buried junctions arranged electrically in series with electrocatalysts submerged in an electrolyte. The electrocatalysts may or may not be in physical contact with the PV electrodes, but in all such systems the photovoltage generated by the structure is independent of the nature of the electrocatalyst/electrolyte interface. Examples of PV-biased electrosynthetic cells include AlGaAs/GaAs tandem structures,[9] amorphous hydrogenated Si (a-Si:H) triple-junction structures,[10-12] triple-junction structures based on $CuInGaSe_2$ (Figure 2.2b-d),[13] and n-Si/SiO_x/In-doped Tin Oxide (ITO) structures.[14]

The advantages of PV-based solar fuels generators are the high reported solar-to-fuels efficiencies and the independence of the power-producing junction with respect to the formal potential for the reactions of interest.[15] The challenges associated with PV-based cells include achieving a cost advantage for a system with the functioning photovoltaic cell immersed in the electrolyte, relative to a system that utilizes a discrete photovoltaic cell in dry conditions wired to a discrete fuel-forming device, as well as finding catalyst/ electrolyte interfaces that are transparent, conductive, and stable under operational, fuel-forming conditions. [11, 12, 15-18] Thus, the key research needs involve the development of cost-competitive photovoltaic cells, the integration of components, discovery of materials, development of low-cost fabrication methods, and the stabilization of electrodes through the use of materials that act as transparent and conductive protecting layers.

2.3 Photoelectrochemical Cells

Another fundamentally identifiable approach to effect the separation of charge carriers is through the use of a solid/ionic-conductor junction. Devices utilizing solid/ionic-conductor junctions, also referred to as solid/electrolyte junctions, are called *photoelectrochemical* (PEC) *cells* (Figure 2.3a). The solid in a PEC cell is commonly a semiconductor and may or may not have an attached photosensitizer. Other solids, including metals such as platinum and mercury, have also been observed to produce a photovoltage at a solid/ electrolyte interface when the appropriate electrolyte is present.[19,2019, 20]

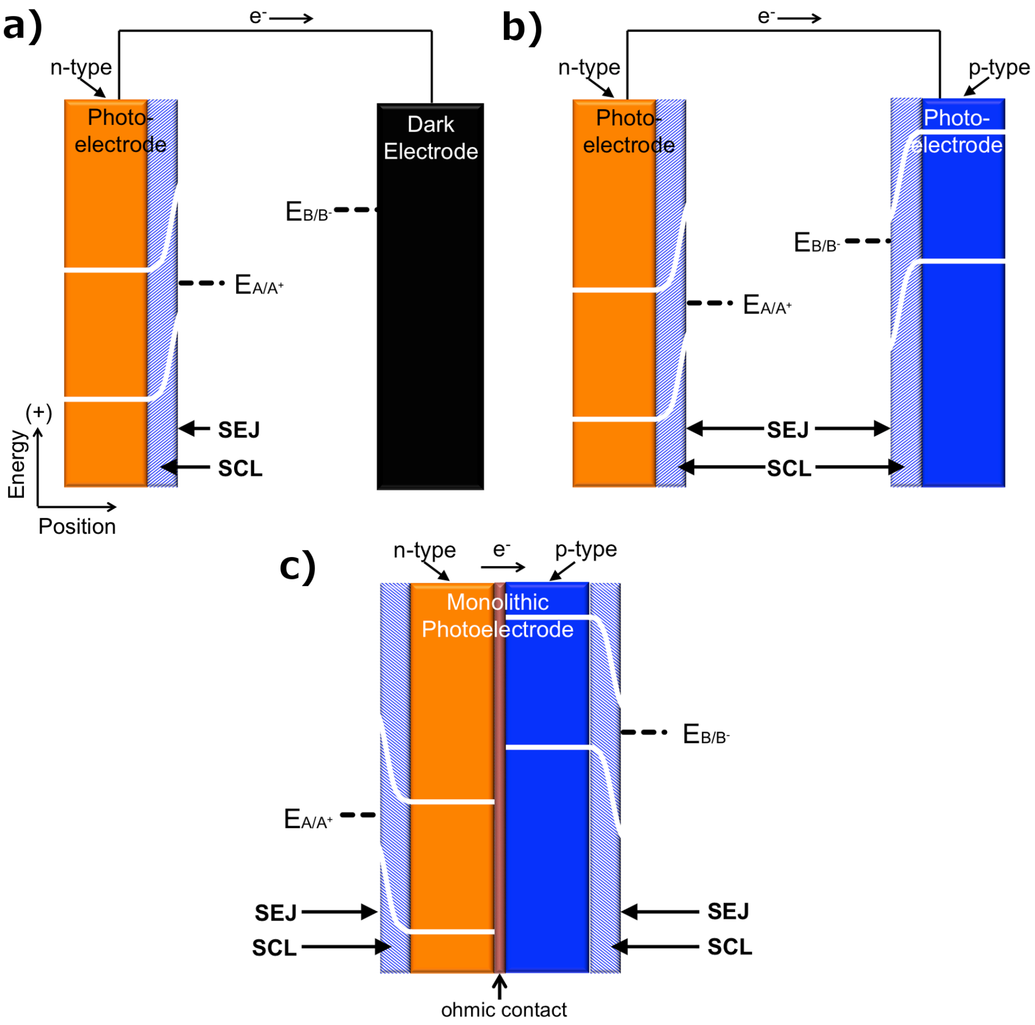

Figure 2.3: Illustrations of photoelectrochemical cells that effect two general half-reactions with a) one photoelectrode and a dark electrode, b) two separate (dual) photoelectrodes, and c) a monolithic structure with two junctions oriented in series with respect to the incoming light (tandem photoelectrodes). The physical location of the semiconductor/electrolyte junction (SEJ) and the electric potentials of the conduction and valence bands are shown in each diagram.

In a device utilizing a solid/electrolyte junction, the photovoltage and photocurrent produced in the presence of light arise from differences in the electrochemical potentials of the solid and the electrolyte as well as from asymmetries in the charge-transfer kinetics for electrons and holes across the junction. The operating principles of photoelectrodes have been well documented for incorporation into full PEC cells that either produce electricity or fuels.[21] The properties of such photoelectrodes are determined routinely from a conventional three-electrode potentiostatic experiment using a half-cell configuration, with the understanding that the photoelectrode can be incorporated into an operational, two-electrode, full PEC cell. Unlike PV cells, for a given PEC-based solar fuels generator, photocurrent-voltage measurements cannot be made independently of the reaction of interest.

PEC cells that utilize a semiconducting electrode can consist of one photoelectrode that has a semiconductor/electrolyte junction, in conjunction with a "dark" counter electrode (Figure 2.3a); of two photoelectrodes, each with a semiconductor/electrolyte junction (Figure 2.3b); or of a monolithically integrated combination of two photoelectrodes in a single structure that performs both the anodic and cathodic half-reactions simultaneously (Figure 2.3c).

PEC cells that only produce electricity are referred to as *regenerative photoelectrochemical cells* (Figure 2.4a), because the species that is reduced or oxidized at the working photoelectrode is regenerated at the counter electrode, ideally yielding zero net change in the composition of the solution.[4, 7, 8, 22] PEC cells that produce fuels at the semiconductor/electrolyte junction are referred to as *photoelectrosynthetic cells*

(Figure 2.4b).[7, 23, 24] An example of a regenerative PEC cell is the n-Si/CH_3OH-1,1'dimethylferrocene/ITO cell (Figure 2.4c, n-Si is the photoelectrode).[25] Dye-sensitized solar cells (DSSCs) are also commonly operated as regenerative PEC cells.[26] Examples of photoelectrosynthetic PEC cells include n-$SrTiO_3$/NaOH(aq)/Pt cells for water splitting (Figure 2.4d, $SrTiO_3$ is the photoelectrode) [27], n-MoS_2/Pt cells for the production of H_2 and I_2 from HI(aq) (Figure 2.4e, n-MoS_2 is the photoelectrode) [28], and DSSC's including TiO_2 photosensitized with a catalytic molecular $[(PO_3H_2)_2bpy)_2Ru(4\text{-}Mebpy\text{-}4\text{-}bimpy)Ru(tpy)(OH_2)]^{4+}$ unit for water splitting, as well as others. [29-31]

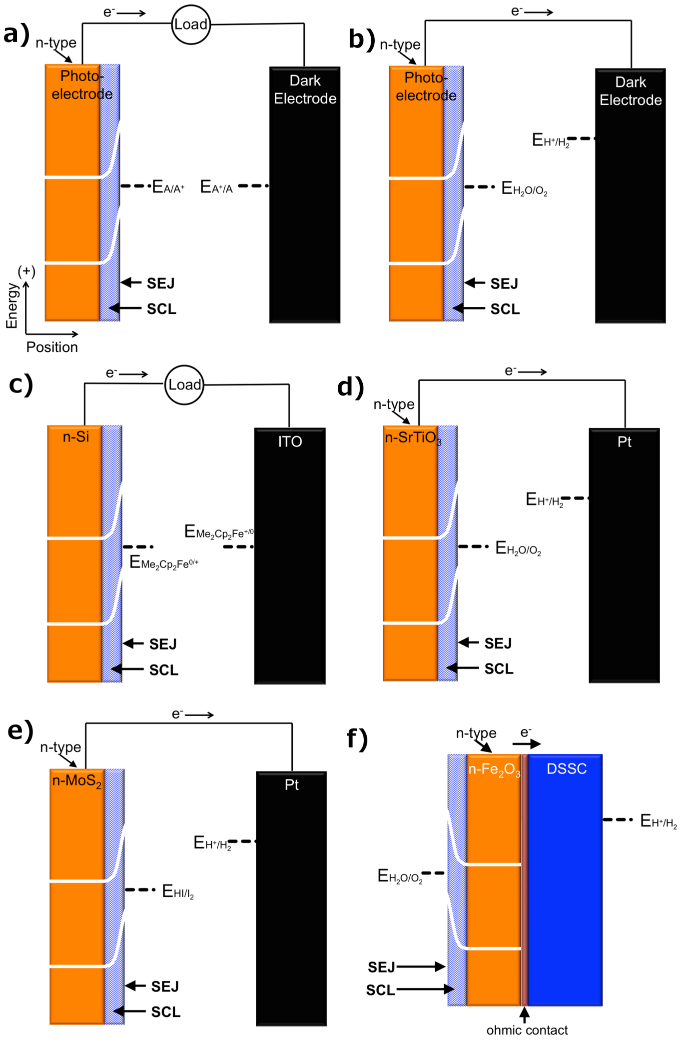

Figure 2.4: Illustrations of photoelectrochemical cells in the dark after equilibration, with the physical position of the semiconductor/electrolyte junction (SEJ) and the electric potentials of the conduction and valence bands shown in each diagram. The expected direction of electron flow under illumination is indicated. The axes in each panel are the same as those in panel a. a) A general regenerative photoelectrochemical cell with one photoelectrode and one dark electrode effecting two half-reactions that collectively yield zero net reaction. This cell produces electrical power, as indicated by the load in the circuit. b) A general photoelectrosynthetic cell that splits water as an example of solar-driven catalysis of a chemical reaction with $\Delta G>0$. c) An example of a regenerative photoelectrochemical cell that uses an n-Si photoelectrode and an ITO dark electrode to produce electrical power using a ferrocenium/ferrocene redox couple. d) An example of a photoelectrosynthetic cell that uses an n-$SrTiO_3$ photoelectrode and a Pt dark electrode to split water. e) An example of a photoelectrosynthetic cell that uses an n-MoS_2 photoelectrode and a Pt dark electrode to effect the unassisted splitting of HI. f) An example of a PEC-biased photoelectrosynthetic cell that uses a monolithic DSSC/n-Fe_2O_3 combination to split water.

The product of coupling a regenerative PEC cell to metallic electrodes produces a *PEC-biased electrosynthetic cell*, whereas the product of coupling a regenerative PEC cell to a photoelectrosynthetic PEC cell is referred to as a *PEC-biased photoelectrosynthetic cell*. Photoelectrochemical cells, like photovoltaic cells, can be used to bias both PEC and PV cells to assist in fuel formation. An example of a PEC-biased photoelectrosynthetic cell is a DSSC placed electrically in series with an Fe_2O_3/electrolyte junction cell for water splitting (Figure 4f). [32] Here, the DSSC is a free-standing, two-terminal device whose photocurrent and photovoltage are independent of the fuel-forming reactions of interest, but which operates as a PEC nonetheless because the photocurrent and photovoltage are not independent of the solution at the interface of the two terminals of the DSSC itself.

The performance of photoelectrodes consisting of semiconductor/electrolyte junctions, in the absence of bulk semiconductor limitations, is determined by the energetics and kinetics of the semiconductor/electrolyte interface. The interfacial energetics determine the photovoltage through the difference between the formal potential of the fuel-forming reaction of interest and the electrochemical potential of the semiconductor, [18, 33, 34] and also determine the driving force needed to produce a given current density. Commonly, an electrocatalyst is incorporated at the semiconductor/electrolyte interface to improve the interfacial charge-transfer kinetics; however, for the device to remain categorized as a PEC cell, the nature of the electrolyte must affect the performance of the cell.[35] Examples of PEC cells with electrocatalysts incorporated at the semiconductor/electrolyte interface include H_2-evolving photocathodes made from metal islands or thin metallic films on p-Si or p-InP photoelectrodes, because the work function of the metal, and thus the barrier height at the semiconductor surface, depends on the concentration of H_2 in the electrolyte.[36, 37] Semiconductor/electrolyte junctions with ion-permeable, redox-active electrocatalysts would also be considered PEC cells because of the electrolyte-dependent behavior of the device.[35] In addition, recent progress on stabilization schemes based on thin coatings on the surface of the semiconductor has produced examples of photoelectrodes in which the solution potential affects the photovoltage even though the photoelectrode is not in direct physical contact with the solution.[38, 39] Conversely, electrocatalysts deposited on semiconductors, such as CoPi on Fe_2O_3, are reported to convert what would otherwise be photoelectrosynthetic cells into photovoltaic electrosynthetic cells, by formation of a Schottky junction at the semiconductor/catalyst junction.[40-42] Careful evaluation is often necessary to determine whether a device is a PV or PEC cell when electrocatalysts are present on the surface. Data, including the current-voltage characteristics of the catalyst alone, the photocurrent-voltage characteristics of the semiconductor with and without the presence of the electrocatalyst, the photocurrent-voltage behavior of the semiconductor with and without electrocatalyst in contact with electrolytes of varying composition and electrochemical potential, and laser spectroscopic data on the electron-hole recombination mechanism in the presence or absence of electrocatalyst, may be necessary to ascertain whether such a system is properly classified as a PV or PEC cell.

The principal advantages of PEC cells are their simplicity of fabrication and the finding that inexpensive polycrystalline semiconductor/electrolyte junctions can often perform nearly as well as their single crystalline counterparts.[43-45] The challenges associated with PEC cells include obtaining a combination of materials that are operationally stable and also possess appropriate interfacial energetics and band gaps, as well as the development and integration of electrocatalysts into the semiconductor/electrolyte junction. Thus, the key research needs for solar fuels generators based on PEC cells involve the discovery and development of semiconducting materials that possess both the proper band gaps for effective sunlight absorption and well-positioned band energetics, and the development of methods for incorporating efficient electrocatalysts into semiconductor/electrolyte interfaces that are stable under operational, fuel-forming conditions.[18, 46-49]

2.3.1 Photovoltaic-Biased Photoelectrochemical Cells

The product of coupling a PV cell with a PEC cell, resulting in a cell that contains both a buried junction and a semiconductor/electrolyte junction, is a *PV-biased PEC cell* (Figure 2.5a). In this hybrid approach, the advantages of both cells are combined through increased flexibility in materials availability. Like their parent cells, PV-biased PEC cells can produce electricity or fuel.

PV-biased PEC cells that produce electricity are referred to as a *PV-biased regenerative PEC cell*. PV-biased PEC cells that produce fuels and that include at least one buried junction may fall into a number of categories, which are systematically named based on whether fuel formation occurs at a solid/electrolyte junction in the device and the presence or absence of additional two-terminal regenerative PEC cells. *PV-biased photoelectrosynthetic cells* are PV-biased PEC cells in which fuel formation occurs at the solid/electrolyte junction. PV-biased PEC cells that produce fuels that are formed away from a solid/electrolyte junction, but include at least one isolated regenerative PEC cell, are referred to as *Regenerative PEC- and PV-biased electrosynthetic cells*. PV-biased

PEC cells that include at least one isolated regenerative PEC cell, but that produce fuels that are formed at a solid/electrolyte junction, are referred to as *Regenerative PEC- and PV-biased photoelectrosynthetic cells.* Examples of PV-biased PEC cells include the “Turner Cell”, a GaAs buried junction electrically in series and monolithically integrated with a p-$GaInP_2$/electrolyte junction (Figure 2.5b), as well as an a-Si:H PV cell electrically in series with a $BiVO_4$/electrolyte junction (Figure 2.5c) and the PEC cells often referred to as ‘septum-based PEC cells’. [50-54]

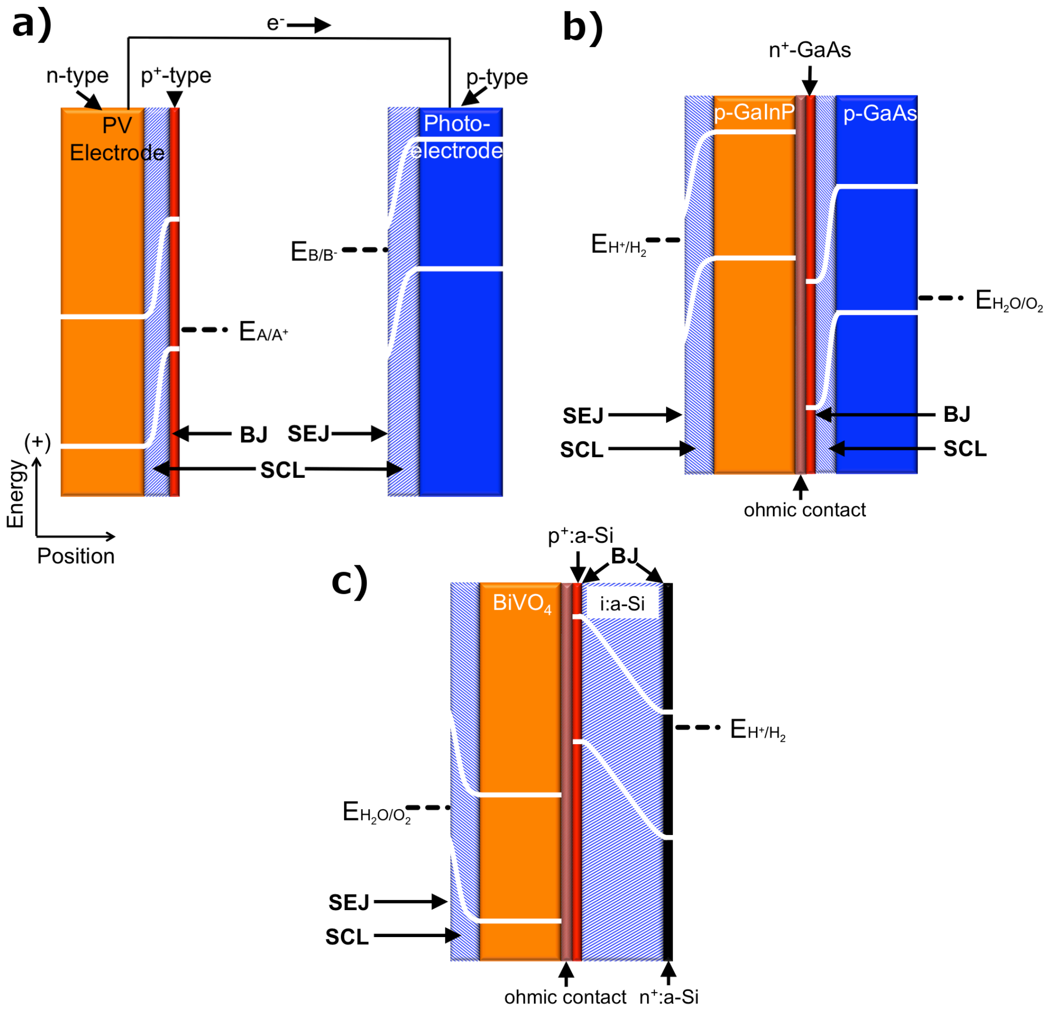

Figure 2.5: Illustrations of photovoltaic-biased photoelectrochemical cells in the dark after equilibration, with the physical position of the semiconductor/electrolyte junction (SEJ), the buried junction (BJ), and the electric potentials of the conduction and valence bands shown in each diagram. The expected direction of electron flow under illumination is indicated. The axes in each panel are the same as those in panel a. a) A general photovoltaic-biased photoelectrochemical cell comprising one photovoltaic electrode and one photoelectrochemical electrode that effects two general half-reactions. b) An example of a photovoltaic-biased photoelectrochemical cell that uses tandem photoelectrodes, one utilizing a GaInP/electrolyte junction and the other utilizing a GaAs buried junction, to drive water splitting. c) A recent example of a photovoltaic-biased photoelectrochemical cell that uses tandem photoelectrodes, one utilizing a $BiVO_4$/electrolyte junction and the other utilizing an amorphous hydrogenated Si buried junction, to drive water splitting.

2.4 Photoelectrosynthetic Particulate/Molecular Photocatalysts

Both the buried junction and the semiconductor/electrolyte junction motifs can be employed when the semiconducting material is employed in a dispersed particulate form as opposed to a solid electrode (Figure 2.6). In these particulate systems, the photovoltage and photocurrent that drive the interfacial electrochemical reactions in the presence of illumination are developed as a result of semiconductor/electrolyte and/or buried junctions in a single discrete particle unit that generally contains separate co-catalysts for each half-reaction. [55]

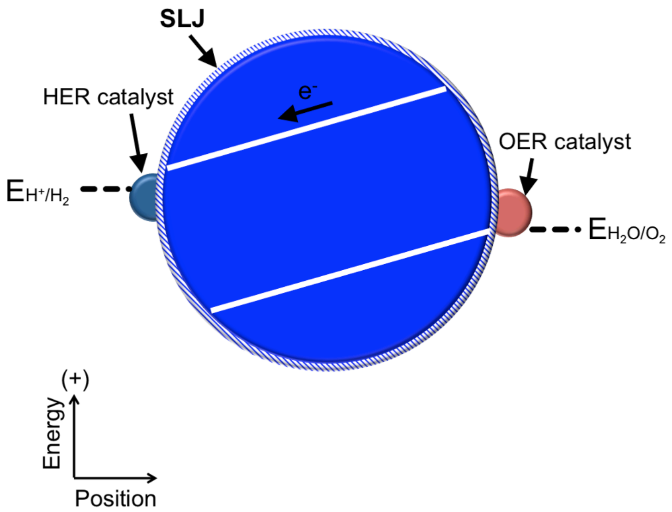

Figure 2.6: Illustration of a photocatalytic particle in the dark after equilibration, with the physical position of the semiconductor/electrolyte junction (SEJ) and the electric potentials of the conduction and valence bands shown in the diagram. This photocatalytic particle is shown performing water splitting with two separate co-catalysts attached to its surface. Instead of a semiconductor/electrolyte junction the particle could utilize a buried junction. In practice, multiple particles are suspended in an electrolyte.

Although in theory one could distinguish between particles utilizing buried and semiconductor/electrolyte junctions in the same way as for the PEC and PV cells, in practice, these two types of systems are difficult to distinguish experimentally. A comparison of the photovoltage produced by a particle in solution with that measured across a particle removed from solution may be difficult or impossible to perform, due to the small size of the particles and the resulting effective absence of addressable electrodes. Indirect measurements of the photocurrent and/or photovoltage under varying conditions may be obtained by correlating changes in the amount of products formed by the light-driven reaction with various solution compositions, but accurate measurements of the products will be hindered by product crossover and incompatible catalysts. The particulate versions of PV and PEC cells, as well as the related photo-driven molecular photocatalysts wherein inorganic molecular compounds are dispersed in solution, share many of the same research challenges as their parent categories, with the added challenge of developing methods to physically separate the products of the fuel-forming reactions. The term cell does not apply to particulate schemes that employ neither addressable electrodes nor a built-in means to enforce the separation of products. For these reasons, we consider all three of these strategies to comprise members of the general category of *photoelectrosynthetic particulate/molecular photocatalysts*.[7, 56, 57]

An example of photoelectrosynthetic particulate photocatalysts are CdS particles in contact with TiO_2 particles, with an electrical asymmetry at the CdS/TiO_2 interface.[57-59] Other examples include a NiO-$SrTiO_3$ photocatalyst capable of concomitantly evolving H_2 and O_2, as well as a number of metal nitrides, oxides, and oxynitrides (e.g. ZrO_2, TaON, Ta_3N_5, WO_3).[57] Similarly, the performance of a photoelectrosynthetic molecular photocatalyst is based either on monomolecular photochemical processes or on coupled photoelectrochemical-photochemical or photochemical-dark reactions in an individual molecular unit. Examples of photoelectrosynthetic molecular cells include light-driven water splitting by UV irradiation of aqueous Ce(III)/Ce(IV) solutions; [60] the use of molecular triads or tetrads coupled to nanoparticulate or molecular electrocatalysts for fuel production;[61] the coupling of molecular catalysts to photoactive proteins;[62, 63] and related systems.[64, 65]

The principal advantages of particulate/molecular photocatalysts are the simplicity of the photocatalysts relative to other approaches and the associated low predicted system cost, with a recent technoeconomic analysis suggesting that systems based on particulate/molecular photocatalysts could be significantly less expensive than electrode-based systems when deployed at scale.[15] The challenges facing development of systems from photoelectrosynthetic particulate/molecular photocatalysts involve stabilizing all of the components, addressing safety concerns arising from the production of explosive mixtures of stoichiometric fuel products, and controlling undesired recombination processes to realize high steady-state quantum yields for net fuel production. Specific undesired processes include photogenerated electrons reducing key surface-bound intermediates, intermediates in solution, or products of the oxidation of water to O_2, as well as photogenerated holes participating in analogous oxidation reactions, and the spontaneous recombination of the fuels facilitated by contact with the co-catalysts at any location in the system.

2.5 Discussion

Both PV and PEC cells can be structured with multiple junctions to optimize the theoretical maximum efficiency for a given fuel-forming reaction.[66] Single-junction cells are best suited for fuel-forming reactions that require operating voltages near or below the ~1 V maximum power point of the single-junction devices that have the highest reported energy-conversion efficiency.[67] Fuel-forming reactions that require larger voltages also require more junctions to better utilize the solar spectrum, with the optimal number of junctions being dependent on the voltage required for the operating current density. Therefore, the maximum realizable efficiencies for water splitting are generally obtained with a tandem-absorber cell, where two light absorbers with appropriately tuned band gaps are arranged in series with respect to the incident light.[9, 53] Additional junctions can increase the efficiency of solar devices when the semiconductors have carefully selected band gaps. [68] Triple-junction cells utilizing a single semiconductor or two semiconductors have also been used to effect solar-driven water splitting when related double junction devices were unable to generate sufficient voltage.[11, 12, 51] When the same semiconductor is used to form multiple junctions, the cells suffer from a loss of current to achieve the necessary voltage for water splitting.

Advanced structuring of PV- and PEC-based solar fuels generators can offer additional efficiency gains for systems, including those for which all of the components are in contact with the electrolyte. One example of advanced structuring is an array of p-Si microwires that have radial n^+-doped emitter regions, with an electrocatalyst placed in specific physical locations between or along the surfaces of the microwires (Figure 2.7).[69] Some ambiguity exists regarding the classification of such a system. The mechanism of charge separation is a buried junction, and thus the device falls into the category of photovoltaic cells.

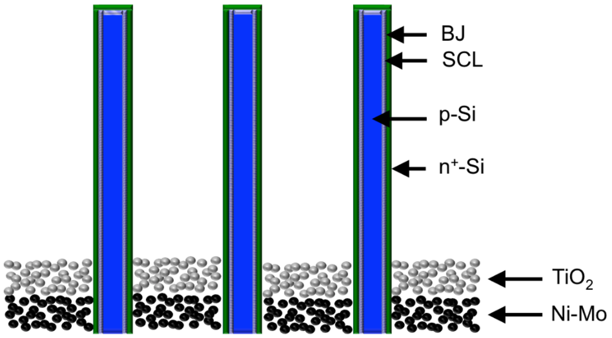

Figure 2.7: A next-generation photocathode that employs advanced structuring to improve performance. This photocathode consists of an array of Si microwires, each microwire with a buried junction and connected to hydrogen-evolution catalysts (Ni-Mo). TiO_2 scattering particles are located at the base of the microwire array to maintain high catalytic activity while also maintaining high light absorption in the semiconductor. This photocathode could be combined with a (photo)anode to form a complete cell.

However, although in concept a conformal electrical contact could be made to the microwires, with the resulting electrical current then passed to another identically microstructured conductive electrode that possessed the spatial distribution, loading, and resulting activity of the electrocatalyst in the integrated structure, separation of the integrated system into essentially identically functioning discrete components would be difficult to accomplish in practice. Because the performance of the device critically depends on the details of, and the presence of, the absorber/electrolyte junction, which acts in this case in a synergetic fashion with respect to one or more other components of the integrated system, designation of the device as a photoelectrochemical cell might seem reasonable. Furthermore, if the microwires are removed from the substrate and embedded in an immobilizing membrane, they may be deemed similar to a photoelectrosynthetic particulate photocatalyst. In this case, however, the uniform particle orientation and built-in barrier for product separation would produce a photoelectrosynthetic particulate cell rather than a photoelectrosynthetic particulate photocatalyst. This discussion serves to emphasize that while some devices easily fall into a single taxonomic classification and therefore are subject to the research challenges associated with that classification, other devices may have characteristics of multiple classifications with some or all of the related challenges, advantages, or disadvantages.

2.6 Conclusion

Although researchers have developed diverse designs for solar fuels generators based on a diverse set of underlying principles, solar fuels generators are often grouped together and denoted as "photoelectrochemical cells". The purpose of this chapter is not to favor, or establish a bias or preference towards, any specific design or approach. The different performance/cost/function trade-offs associated with each approach ultimately will determine which of these distinct technological approaches to the development of solar fuels generators will prove viable in the marketplace. Instead, we have described a taxonomy for solar fuels generators that is based on the operating principles underlying the designs, to bring clarity and precision to discussions of research in the field of artificial photosynthesis while facilitating concise and consistent identification of the research challenges and state-of-the-art for each type of system.

2.7 Acknowledgements

The bulk of the above work appeared in *Energy and Environmental Science* in 2015 (DOI: 10.1039/c4ee02251c). Matthew R. Shaner, Kimberly M. Papadantonakis, and Sonja A. Francis are thanked for their extensive and invaluable contributions.

2.8 References

1. A. J. Bard and M. A. Fox, *Acc. Chem. Res.*, 1995, 28, 141-145.
2. S. J. Fonash, *Solar Cell Device Physics*, Elsevier Inc., Amsterdam, 2nd edn., 2010.
3. N. Serpone and E. Pelizzetti, *Photocatalysis: Fundamentals and Applications*, John Wiley & Sons, Inc., Hoboken, NJ, 1989.
4. M. X. Tan, P. E. Laibinis, S. T. Nguyen, J. M. Kesselman, C. E. Stanton and N. S. Lewis, in *Prog. Inorg. Chem.*, ed. K. D. Karlin, John Wiley & Sons, Inc., 1994.
5. Within this *Opinion*, we specifically denote as ‘junctions’ those interfaces whose electrical asymmetry leads to the development of a photovoltage or photocurrent upon illumination. In other contexts, the interface between two materials that do not generate a photocurrent or photovoltage under illumination, such as ohmic contacts, may also be referred to as a ‘junction’.
6. The term ‘photovoltaic’ has been used in a number of contexts, including to denote any device that generates a measurable photocurrent or photovoltage upon illumination, including specifically photoelectrochemical cells (references 7,8). This usage is defendable because both PV and PEC cells exhibit a photovolatic effect as understood by the strict definition of the term ‘photovoltaic’. However, as alluded to in reference 8, photoelectrochemical cells are commonly differentiated from cells that utilize a junction between two electronic conductors, to emphasis the different underlying princples in the two different types of systems. The term ‘photovoltaic’ is therefore used herein to refer to only those devices that include a junction between electronic conductors.

7. A. J. Bard, R. Memming and B. Miller, *Pure Appl. Chem.*, 1991, 63, 569-596.
8. S. Licht, ed., *Semiconductor Electrochemistry and Photoelectrochemistry*, Wiley-VCH, Weinheim, Germany, 2002.
9. S. Licht, B. Wang, S. Mukerji, T. Soga, M. Umeno and H. Tributsch, *J. Phys. Chem. B*, 2000, 104, 8920-8924.
10. *USA Pat.,* 4,466,869, 1984.
11. S. Y. Reece, J. A. Hamel, K. Sung, T. D. Jarvi, A. J. Esswein, J. J. H. Pijpers and D. G. Nocera, *Science*, 2011, 334, 645-648.
12. R. E. Rocheleau, E. L. Miller and A. Misra, *Energy Fuels*, 1998, 12, 3-10.
13. T. J. Jacobsson, V. Fjallstrom, M. Sahlberg, M. Edoff and T. Edvinsson, *Energy & Environmental Science*, 2013, 6, 3676-3683.
14. G. Hodes, L. Thompson, J. DuBow and K. Rajeshwar, *J. Am. Chem. Soc.*, 1983, 105, 324-330.
15. B. D. James, G. N. Baum, J. Perez and K. N. Baum, *Technoeconomic Analysis of Photoelectrochemical (PEC) Hydrogen Production*, 2009.
16. A. J. Bard and M. S. Wrighton, *Journal of The Electrochemical Society*, 1977, 124, 1706-1710.
17. R. Noufi, A. J. Frank and A. J. Nozik, *J. Am. Chem. Soc.*, 1981, 103, 1849-1850.
18. M. G. Walter, E. L. Warren, J. R. McKone, S. W. Boettcher, Q. Mi, E. A. Santori and N. S. Lewis, *Chem. Rev.*, 2010, 110, 6446-6473.
19. M. Heyrovsky and R. G. W. Norrish, *Nature*, 1963, 200, 880-881.
20. W. J. Albery, *Acc. Chem. Res.*, 1982, 15, 142-148.
21. B. Parkinson, *Acc. Chem. Res.*, 1984, 17, 431-437.

22. In accordance with references 4 and 8, we have chosen to use the term 'regenerative photoelectrochemical cell' to denote a cell that utilizes a solid/electrolyte junction to generate electricity, with no net chemical conversion, under illumination. This usage in contrast to that of reference 7, which refers to these systems as 'photovoltaic' devices. As described above, we have reserved the term 'photovoltaic' to denote a system that utilizes a junction between two electronic conductors, in accord with broad usage and with the definition in many dictionaries of the term "photovoltaic".

23. In accordance with reference 24, we have used the term 'photoelectrosynthetic' to encompass all devices in which a net chemical conversion takes place. We recognize that the term 'photoelectrolytic' has been used (e.g., ref 7) in this context to refer to devices in which a net chemical conversion occurs with $\Delta G>0$, and the term 'photocatalytic' has been used to refer to devices with $\Delta G<0$. We chose our nomenclature to avoid confusion with the common usage of the term 'photocatalyst'.

24. J. Connolly, ed., *Photochemical conversion and storage of solar energy*, Academic Press, New York, 1981.

25. C. M. Gronet, N. S. Lewis, G. Cogan and J. Gibbons, *Proc. Nat. Acad. Sci. USA*, 1983, 80, 1152-1156.

26. M. Grätzel, *J. Photochem. Photobiol. C*, 2003, 4, 145-153.

27. M. S. Wrighton, A. B. Ellis, P. T. Wolczanski, D. L. Morse, H. B. Abrahamson and D. S. Ginley, *J. Am. Chem. Soc.*, 1976, 98, 2774-2779.

28. C. Levy-Clement, A. Heller, W. A. Bonner and B. A. Parkinson, *Journal of The Electrochemical Society*, 1982, 129, 1701-1705.

29. L. Alibabaei, M. K. Brennaman, M. R. Norris, B. Kalanyan, W. Song, M. D. Losego, J. J. Concepcion, R. A. Binstead, G. N. Parsons and T. J. Meyer, *Proc. Nat. Acad. Sci. USA*, 2013, DOI: 10.1073/pnas.1319628110.

30. J. R. Swierk and T. E. Mallouk, *Chem. Soc. Rev.*, 2013, 42, 2357-2387.

31. K. J. Young, L. A. Martini, R. L. Milot, R. C. Snoeberger Iii, V. S. Batista, C. A. Schmuttenmaer, R. H. Crabtree and G. W. Brudvig, *Coord. Chem. Rev.*, 2012, 256, 2503-2520.

32. J. Brillet, J.-H. Yum, M. Cornuz, T. Hisatomi, R. Solarska, J. Augustynski, M. Graetzel and K. Sivula, *Nat. Photonics*, 2012, 6, 824-828.

33. R. van de Krol, Y. Liang and J. Schoonman, *Journal of Materials Chemistry*, 2008, 18, 2311-2320.

34. H.-J. Lewerenz and L. Peter, *Photoelectrochemical Water Splitting*, The Royal Society of Chemistry.

35. F. Lin and S. W. Boettcher, *Nature Materials*, 2014, 13, 81-86.

36. E. Aharon-Shalom and A. Heller, *Journal of The Electrochemical Society*, 1982, 129, 2865-2866.

37. R. N. Dominey, N. S. Lewis, J. A. Bruce, D. C. Bookbinder and M. S. Wrighton, *J. Am. Chem. Soc.*, 1982, 104, 467-482.

38. N. C. Strandwitz, D. J. Comstock, R. L. Grimm, A. C. Nichols-Nielander, J. Elam and N. S. Lewis, *J. Phys. Chem. C*, 2013, 117, 4931-4936.

39. A. C. Nielander, M. J. Bierman, N. Petrone, N. C. Strandwitz, S. Ardo, F. Yang, J. Hone and N. S. Lewis, *J. Am. Chem. Soc.*, 2013, 135, 17246-17249.

40. M. Barroso, A. J. Cowan, S. R. Pendlebury, M. Grätzel, D. R. Klug and J. R. Durrant, *J. Am. Chem. Soc.*, 2011, 133, 14868-14871.

41. M. Barroso, C. A. Mesa, S. R. Pendlebury, A. J. Cowan, T. Hisatomi, K. Sivula, M. Grätzel, D. R. Klug and J. R. Durrant, *Proc. Nat. Acad. Sci. USA*, 2012, 109, 15640-15645.

42. M. Barroso, S. R. Pendlebury, A. J. Cowan and J. R. Durrant, *Chemical Science*, 2013, 4, 2724-2734.

43. A. Heller, in *Photoeffects at Semiconductor-Electrolyte Interfaces*, American Chemical Society, 1981, vol. 146, ch. 4, pp. 57-77.

44. A. Heller, *Acc. Chem. Res.*, 1981, 14, 154-162.

45. S. R. Lunt, L. G. Casagrande, B. J. Tufts and N. S. Lewis, *J. Phys. Chem.* 1988, 92, 5766-5770.

46. N. S. Lewis and G. Crabtree, ed. U. S. D. O. E. Office of Science, Washington, DC, 2005.

47. M. F. Weber and M. J. Dignam, *J. Electrochem. Soc.*, 1984, 131, 1258-1265.

48. S. Hu, C. Xiang, S. Haussener, A. D. Berger and N. S. Lewis, *Energy & Environmental Science*, 2013, 6, 2984-2993.

49. M. F. Weber and M. J. Dignam, *Int. J. Hydrogen Energy*, 1986, 11, 225-232.

50. Although the Turner Cell (reference 53) is classified as a PV-Biased PEC cell, the surface of the p-$GaInP_2$ at the p-$GaInP_2$/3M H_2SO_4(aq) interface is covered in a thin layer of Pt. This suggests the possibility that the *I-V* characteristics of this

device may be independent of the nature of the electrolyte at the p-$GaInP_2$/3M H_2SO_4(aq) interface, which would then result in the appropriate designation of this cell as a PV-Biased electrosynthetic cell. However, as noted in ref 35, the *I-V* behavior of electrodes consisting of thin layers of Pt on semiconductors is often dependent on the pH of the electrolyte. Thus, based on the available data, is not clear whether the Turner Cell is more appropriately designated as PV-Biased photoelectrosynthetic cell or as a PV-Biased electrosynthetic cell. A similar argument is relavent for the devices discussed in reference 51.

51. F. F. Abdi, L. Han, A. H. M. Smets, M. Zeman, B. Dam and R. van de Krol, *Nat. Commun.*, 2013, 4.

52. A. J. Bard and T. E. Mallouk, *J. Phys. Chem.*, 1993, 97, 7127-7128.

53. O. Khaselev and J. A. Turner, *Science*, 1998, 280, 425-427.

54. S. C. Kondapaneni, D. Singh and O. N. Srivastava, *J. Phys. Chem*, 1992, 96, 8094-8099.

55. K. Domen, S. Naito, M. Soma, T. Onishi and K. Tamaru, *J. Chem. Soc., Chem. Commun.* 1980, DOI: 10.1039/C39800000543, 543-544.

56. We have used the term ‘photocatalyst’ to describe these systems, in accordance with common parlance and in accord with the usage of reference 57. We recognize that ‘photocatalysis’ is often, however, used to refer specifically to the light-driven catalysis of a reaction for which $\Delta G<0$ (reference 7).

57. T. Hisatomi, J. Kubota and K. Domen, *Chem. Soc. Rev.*, 2014, DOI: 10.1039/C3CS60378D.

58. K. R. Gopidas, M. Bohorquez and P. V. Kamat, *J. Phys. Chem*, 1990, 94, 6435-6440.

59. N. Serpone, E. Borgarello and M. Gratzel, *J. Chem Soc., Chem. Commun.,* 1984, DOI: 10.1039/C39840000342, 342-344.

60. J. Weiss and D. Porret, *Nature*, 1937, 139, 1019-1020.

61. D. Gust, T. A. Moore and A. L. Moore, *Acc. Chem. Res.*, 2009, 42, 1890-1898.

62. S. C. Silver, J. Niklas, P. Du, O. G. Poluektov, D. M. Tiede and L. M. Utschig, *J. Am. Chem. Soc.*, 2013, 135, 13246-13249.

63. L. M. Utschig, S. C. Silver, K. L. Mulfort and D. M. Tiede, *J. Am. Chem. Soc.*, 2011, 133, 16334-16337.

64. P. Du, J. Schneider, G. Luo, W. W. Brennessel and R. Eisenberg, *Inorg. Chem.*, 2009, 48, 4952-4962.

65. B. D. Yuhas, A. L. Smeigh, A. P. Douvalis, M. R. Wasielewski and M. G. Kanatzidis, *J. Am. Chem. Soc.*, 2012, 134, 10353-10356.

66. J. R. Bolton, S. J. Strickler and J. S. Connolly, *Nature*, 1985, 316, 495-500.

67. B. M. Kayes, H. Nie, R. Twist, S. G. Spruytte, F. Reinhardt, I. C. Kizilyalli and G. S. Higashi, presented in part at the 37th IEEE Photovoltaic Specialists Conference, Seattle, WA, 2011.

68. C. H. Henry, *J. Appl. Phys.*, 1980, 51, 4494-4500.

69. E. L. Warren, J. R. McKone, H. A. Atwater, H. B. Gray and N. S. Lewis, *Energy & Environmental Science*, 2012, 5, 9653-9661.

Chapter 3

Methods for Solar Energy Conversion Efficiency Measurement

3.1 Introduction and Background

As the fields of photoelectrochemical (PEC) energy conversion and solar fuels have grown, a number of metrics have been adopted for evaluating the performance of electrodes and systems. These metrics are often contradictory, irreproducible, or not properly standardized, which prevents researchers from accurately comparing the performance of materials, even within the PEC community itself. We explore herein these different metrics to evaluate their strengths and applicability, as well as to demonstrate the knowledge derived from each approach. We also present a framework for reporting these metrics in an unambiguous and reproducible manner. Additionally, we outline a method to estimate two-electrode system efficiencies from three-electrode potentiostatic measurements, to accelerate the identification of promising system components without requiring the actual construction of a full system. Clarifying these issues will benefit the PEC community by facilitating the consistent reporting of electrode performance metrics, and will allow photoelectrodes and solar fuels systems to be appropriately compared in performance to other solar energy-conversion technologies.

The energy-conversion efficiency is a key metric that facilitates comparison of the performance of various approaches to solar-energy conversion. However, a suite of disparate methodologies has been proposed and used historically to evaluate the efficiency of systems that produce fuels, either directly or indirectly, with sunlight and/or electrical power as the system inputs. A general expression for the system efficiency is given as the ratio of the total output power (electrical plus chemical) divided by the total input power (electrical plus solar). The solar-to-hydrogen (STH) efficiency follows from this globally applicable system efficiency but is applicable only in the special case for systems in which the only input power is sunlight and the only output power is in the form of hydrogen fuel derived from solar-driven water splitting. Herein, system-level efficiencies, beyond the STH efficiency, as well as component-level figures-of-merit, are defined and discussed to describe the relative energy-conversion performance of key photoactive components of complete systems. These figures-of-merit facilitate the comparison of electrode materials and interfaces without conflating their fundamental properties with the engineering of the cell setup. The resulting information about the components can then be used in conjunction with a graphical circuit analysis formalism to obtain "optimal" system efficiencies that can be compared between various approaches, when the component of concern is used in a reference fuel-producing energy-conversion system. The approach provides a consistent method for comparison of the performance at the system and component levels of various technologies that produce fuels and/or electricity from sunlight.

Many disparate technological approaches are being pursued to convert solar energy into electricity and fuels. For example, photovoltaic (PV) cells, photoelectrochemical (PEC) cells, and solar-thermal systems can directly produce electricity from sunlight. Similarly, fuels can be produced from sunlight either directly by PEC cells or by solar-driven electricity connected to electrolyzers, either as discrete, stand-alone units or as an integrated system [1, 2]. Fuels can also be generated by thermochemical systems [3-5] or by engineering chemical reactions in biological systems [6]. It is imperative to adopt a consistent approach to report the energy-conversion efficiencies for these various technologies. In all cases, the input power (sunlight, electricity) and output power (electricity, fuels) can be measured by a variety of analytical methods, and the absolute efficiency of any technology can be reported or compared directly to any other.

For solar-fuels generating systems, the solar-to-fuels (STF) efficiency can be directly determined by analysis of the chemical products formed under solar illumination in the absence of an applied bias [7, 8]. The STF efficiency is an important metric for comparing solar-fuels systems to other technologies. However, this metric is reductive by definition, as it does not delineate the sources of loss or sub-optimal performance in a system. A STF metric provides little guidance regarding the potential for improvement because nearly all of the details of performance of the electrodes and of the system design are entangled in this single result. In addition, the STF efficiency is not applicable to systems that require electrical power as a partial input or that produce electrical power as a partial output. Conversely, the electrode *components* of a solar-fuels generating system can be isolated and characterized via electronic and electrochemical methods, and such results can be used to elucidate the catalytic and photovoltaic properties of a component as well as sources of energy-conversion inefficiencies for that component. The translation of these component measurements to STF device performance, however, must be done with care. Furthermore, many electrode component metrics that have traditionally been denoted and reported as efficiencies for single electrodes are not true efficiencies, because they are not a measurement of the ratio of the total power output to the total power input. Thus, there is a need to improve the evaluation of single prototypical electrodes and to relate their individual performance to their potential in solar-fuels systems.

Herein we first define the system efficiency generally and then more specifically for various technologies that convert sunlight into a combination of electricity and/or chemical fuels. Next we describe related figures-of-merit and discuss their value for the evaluation of single photoactive electrodes within photoelectrochemical STF devices, as well as important considerations towards using such metrics appropriately. To link the properties of photoactive electrodes to the performance of full systems, we present a method of graphical circuit analysis that permits evaluation of the optimal operating point of a hypothetical system composed of electrodes with well-characterized PEC properties. We also discuss how graphical circuit analyses can guide the engineering of an optimally efficient system architecture based on the characteristics of the chosen components. The methods for calculating the optimal system efficiency discussed herein are intended to provide a complementary and general system analysis method relative to evaluating theoretical system efficiencies based on materials properties such as band gaps [9, 10] or relative to measurements of efficiencies in fully realized STF systems [7].

3.2 System Efficiencies

3.2.1 General Treatment

Consider a system that generates output products in the form of chemical fuels and/or electrical power. The total system output power, P_o, is the sum of the output power contained in the chemical fuel, $P_{f,o}$, and any output power in the form of electricity, $P_{e,o}$. When the incipient output currents, I, due to fuel and electricity production are equal (i.e. the circuit elements are electrically connected in series), this relationship can be expressed as:

$$P_o = P_{f,o} + P_{e,o} = I * \left(E_{f,o} + V_{e,o}\right) \tag{1}$$

where $E_{f,o}$ is the potential difference corresponding to the Gibbs free-energy difference between the two half-reactions of the fuels being produced and $V_{e,o}$ is the output voltage of the electrical power portion of the total system output.

The system inputs may, in general, consist of electrical power, $P_{e,i}$, and/or power from solar illumination, P_s. The total input power, P_i, is therefore:

$$P_i = P_s + P_{e,i} \tag{2}$$

By definition, the efficiency for any process that converts energy from one form to another is the ratio of output power to the input power. The general expression for the *system efficiency* (η) is then simply given by:

$$\eta = \frac{P_{f,o} + P_{e,o}}{P_S + P_{e,i}} \tag{3}$$

The efficiencies of specific technological approaches will be elaborated by examples that are provided in the following sections. For brevity, we do not explicitly treat herein systems in which the input or output power is composed in part from heat transfer to or from the solar energy-conversion system.

3.2.2 Solar-to-Electricity Systems

For systems that solely produce electricity, such as photovoltaic or regenerative photoelectrochemical cells [11], the maximum-power operating current I_{mp} and voltage V_{mp} are the current and voltage that generate the maximum output power, $P_{max} = I_{mp}V_{mp}$. The efficiency of the photovoltaic or regenerative PEC cell is simply the ratio of the electrical power output to the input power provided by solar illumination. This ratio can be calculated from the general efficiency expression (Equation 3) by setting to zero the terms related to chemical fuel output and electrical power input ($P_{\mathrm{f,o}} = 0$ and $P_{\mathrm{e,i}} = 0$). Thus, the efficiency of a *photovoltaic or regenerative PEC system* at maximum power, η_{PV}, is given by:

$$\eta_{PV} = \frac{P_{e,o}}{P_S} = \frac{I_{mp} * V_{mp}}{P_S} \tag{4}$$

3.2.3 Solar-to-Fuels Systems

For comparing the performance of a solar-fuels generator to a solar-electricity generating system, we adopt herein the Gibbs free energy of the fuel as the standardized measure of the energy content of the fuel [7, 8], where the fuel-forming reactions can be, for example, water splitting, hydrogen halide splitting, CO_2 reduction, etc. For a system that produces only fuel as the output and that uses only solar power as the input, the efficiency can be calculated from Equation 3 by setting to zero the terms related to the electrical power input and output ($P_{\mathrm{e,i}} = 0$ and $P_{\mathrm{e,o}} = 0$), such that:

$$\eta_{STF} = \frac{P_{f,o}}{P_s} = \frac{A\,[cm^2] * J_{op}\,[A\,cm^{-2}] * E_{f,o}[V] * \varepsilon_{elec}}{P_s\,[W]} \tag{5}$$

where J_{op} is the operating current density, A is the geometric area of the device, and ε_{elec} is the Faradaic efficiency of the fuel production. The solar-to-hydrogen conversion efficiency of a photo-driven water-splitting system is obtained using the difference in formal potentials of the hydrogen-evolution and oxygen-evolution half-reactions ($E_{\mathrm{f,o}}$ = 1.23 V) to describe the Gibbs free-energy content of the H_2(g) and O_2(g) formed under standard temperature and pressure conditions. For a photo-driven water-splitting system that produces only H_2(g) and O_2(g) as the outputs, the system efficiency is commonly designated as the *solar-to-hydrogen efficiency*, η_{STH}[7, 12, 13]:

$$\eta_{STH} = \frac{A\,[cm^2] * J_{op}\,[A\,cm^{-2}] * 1.23[V] * \varepsilon_{elec}}{P_s\,[W]} \tag{5'}$$

3.2.4 Electricity-to-Fuels Systems

Electrolysis involves the input of electrical power to produce output power as chemical fuel, such as in the form of separated, pure streams of H_2(g) and O_2(g). Electrolyzers operate with no output electrical power ($P_{\mathrm{e,o}}$ = 0) and no power generated by illumination (P_{s} = 0). Assuming that all of the current is derived from Faradaic processes (ε_{elec} = 1), the *efficiency of electrolysis* is:

$$\eta_{\mathrm{electrolyzer}} = \frac{P_{f,o}}{P_{e,i}} = \frac{E_{f,o}}{V_{e,i}} \tag{6}$$

where $V_{e,i}$ is the input voltage required to drive the electrolysis at the operating current density of interest. State-of-the-art electrolyzers require 1.7-1.9 V to effect H_2 production at a current density of 1 A cm^{-2} of projected electrode area, and hence have system efficiencies under such conditions of $\eta_{electrolyzer} = 65\text{-}75\%$ [14].

3.2.5 Mixed Fuel/Electricity/Solar Input and Output Systems

Efficiencies can also be evaluated from Equation 3 for systems that require electrical and optical energy inputs and/or produce both electrical and chemical energy as outputs. As an example of such a system, an n-Fe_2O_3|1.0 M KOH(aq)|Pt cell can be used as the photoanode in photo-driven water-splitting reactions, and could thus generate a portion of the photovoltage required for electrolysis. However, this system requires an external bias to split water, and therefore η_{STH} is zero by definition as Equation 5 makes no allowance for electrical input power. Nevertheless, the system still provides a net conversion of sunlight in the form of a reduced bias needed to drive the electrolysis reaction relative to the situation with two dark electrodes in the system. Throughout the manuscript, 'dark electrode' refers to an electrode which either has negligible incident illumination incident or is not photoactive. Regardless of the details, the system efficiency can be determined from Equation 3. Because no excess electricity is drawn as output from this cell ($P_{e,o} = 0$), the expression for the resulting photo-assisted electrolysis system efficiency (η_{PAE}) is:

$$\eta_{PAE} = \frac{P_{f,o}}{P_S + P_{e,i}}. \tag{7}$$

As another example, an n-$SrTiO_3$ photoelectrode operated in aqueous alkaline environment in conjunction with a Pt counter electrode (i.e., an n-$SrTiO_3$|1.0 M KOH(aq)|Pt cell) can perform the full water-splitting reaction without external bias [15]. The photovoltage produced by this system is in excess of that needed for water electrolysis. The η_{STH} value therefore only accounts for the chemical portion of the realizable output power of the system. The excess photovoltage produced by the system could be harnessed as additional power, either as electrical power or as additional chemical output power through the use of engineering methods such as pressurization of the $H_2(g)$ stream (see below). The system efficiency is regardless given by Equation 3 with $P_{\mathrm{e,i}} = 0$:

$$\eta = \frac{P_{f,o} + P_{e,o}}{P_S} \tag{8}$$

3.3 System Figures of Merit

Although the system efficiency is the key engineering-based figure-of-merit for fully operational electrochemical solar energy-conversion systems, understanding the electrochemical characteristics of the components of a system is crucial for understanding the results of a system efficiency measurement. Different metrics can be employed to characterize the performance of the photoactive components in systems by varying the components or other inputs of the system. In these cases, a 'system' refers to all of the components of a system that necessarily act in concert to produce harvestable power. This definition of a system can, but does not necessarily, include losses related to electrical generation, transmission, or control as would be considered for large-scale technical analyses for cross-technology comparisons. These measurements are often taken on systems employing two electrodes in an electrochemical cell.

One quantity that has been used to describe the performance of photoactive electrodes is the *applied-bias photon-to-current* metric (often called an efficiency, and thus often abbreviated ABPE or ABCE, abbreviated here as ABPC) [16, 17]. As given in Equation 9, this quantity is the difference of the power output in chemical fuel and any added electrical input power, divided by the solar power input [15, 18]:

$$\Phi_{ABPC} = I_{mp} * \frac{(E_{f,o} - V_{ext,mp})}{P_s} \tag{9}$$

Here I_{mp} is the current at the maximum power point, $E_{\mathrm{f,o}}$ is the potential difference corresponding to the Gibbs free energy of the fuel being produced, and $V_{\mathrm{ext,mp}}$ is the applied voltage at the maximum power point between the working photoactive electrode and a standard dark counter electrode.

Φ_{ABPC} is the IUPAC-suggested definition of the solar-conversion efficiency of a cell that has a dark electrode and a semiconductor-based photoactive electrode [18]. In general, however, Φ_{ABPC} is not a measurement of a system efficiency, because Φ_{ABPC} is not a ratio of the total power output divided by the total power input to the system. Rather, Φ_{ABPC} measures the net chemical output power (rate of production of free energy of products less the input electrical power) of a system in units of incident solar power. The Φ_{ABPC} figure-of-merit represents the fraction of the energy stored in the chemical products that can be assigned to the photovoltage provided by the input solar illumination. The value of Φ_{ABPC} can be negative, meaning that the electrical energy input even under illumination is in excess of the free energy stored in the products. For systems that perform fuel-forming reactions without an applied bias (V_{ext}), the expression for Φ_{ABPC} reduces to the analytical form of η_{STH} (Equation 5) if no electrical power is output by the system.

Another metric commonly used to evaluate the effects of input solar illumination is the system-level *power-saved* metric. This metric is quantified by determining the external voltage needed to achieve a current, I, for a system with a photoactive working electrode and a given counter electrode, compared to the voltage needed to achieve that same current in a related system but comprising instead a dark working electrode and the same counter electrode:

$$P_{saved}(I) = I * \left(V_{dark,ext}(I) - V_{light,ext}\,(I)\right) = I * V_{saved}(I) \qquad (10)$$

where $V_{dark,ext}(I)$and $V_{light,ext}(I)$ are the measured external bias values needed to drive the reaction at current I in the dark and light, respectively, and $V_{saved}(I)$ is the difference between $V_{dark,ext}(I)$ and $V_{light,ext}(I)$. Throughout this manuscript, '*' is used to imply multiplication, and conversely a variable followed immediately by another variable in parentheses indicates that the former variable is a function of the latter. The ratio of the saved power to the input solar power is a commonly reported metric based on the power-saved measurement [19], and thus the *ratiometric power saved* is given as:

$$\Phi_{saved} = \frac{I * V_{saved}}{P_S}. \qquad (11)$$

The power-saved metric is further discussed in three-electrode measurements (see section IV.A), because for a given current, the measured quantity is identical for two- and three-electrode configurations.

3.4 Three-Electrode Measurements

Three-electrode electrochemical current density vs. potential (*J-E)* measurements provide a direct evaluation of the properties of an electrode under the relevant solution and illumination conditions, and can be replicated readily by other researchers. This provides a distinct advantage over the less easily replicated two-electrode system measurements discussed above. This fundamental evaluation of electrode performance provides a basis to compare the relative metrics for different electrodes. Furthermore, three-electrode measurements allow identification of the optimal performance achievable in a system that would use the given components, without having to explicitly consider or develop the design, engineering, or operational details of the full system.

In three-electrode voltammetric measurements, a potentiostat is used to control the potential difference between a working electrode and a reference electrode, while the current is measured between the working electrode and a counter electrode, with negligible current passed between the working and reference electrodes. The *J-E* behavior can therefore be determined independently of any overpotentials, mass-transport restrictions of redox species, and potential drops associated with the counter electrode and the counter electrode-electrolyte interface, or of the solution ohmic losses between the working and counter electrodes. Kinetic overpotential and mass transport losses may be considered inherent to an electrode under the relevant conditions, but potentiostatic measurements should always be appropriately corrected for any uncompensated solution resistance, as this quantity is not a fundamental characteristic of an electrode/electrolyte interface.

For photoactive electrode components, the *J-E* behavior can yield the *open-circuit potential*, E_{oc}, the current at the Nernstian potential (E(A/A$^-$)) for the half-reaction of interest, I(E(A/A$^-$)) (or *J(E(A/A*$^-$*))*, the current density), and the photogenerated current, I_{ph} [20], determined by finding the difference between the current under illumination and the dark current, prior to the observation of breakdown phenomena and under conditions that are not mass-transport limited. When I_{ph} is potential-dependent (e.g. due to photogenerated carrier collection being dependent on drift in the depletion region) I_{ph} should be measured separately at each potential of interest.

3.4.1 Power-Saved Metric

In a three-electrode system, the power saved [16, 21, 22] at any current, I, is given by the product of the current I and the difference between the potential required to drive a half-reaction at a selected working electrode at this current in the dark, $E_{dark}(I)$ and the potential required to drive the same half-reaction at a photoactive electrode in the light, $E_{light}(I)$:

$$P_{saved}(I) = I * \left(E_{dark}(I) - E_{light}(I)\right) = I * V_{saved}(I) \qquad (12)$$

The *ratiometric power saved* is still given by P_{saved} divided by the input solar power, P_s:

$$\phi_{saved} = \frac{I * V_{saved}(I)}{P_S}. \tag{13}$$

Because the power-saved measurements are, by definition, differences in performance between the photoactive electrode and a selected dark electrode, all of the cell and system-based losses in a two-electrode system and in a three-electrode cell should cancel out in the calculated power saved difference measurements. Therefore, a power-saved measurement extracted from two three-electrode measurements (Equation 10) is identical to a power-saved measurement obtained from two two-electrode measurements (Equation 12), at a given value of *I.*

Figure 3.1 illustrates the different methods by which three-electrode power-saved measurements can be used to characterize the photoactive electrode performance.

3.4.4.1 Power-Saved Measurements Relative to an Ideally Nonpolarizable Dark Electrode

If the photoactive electrode is compared to an ideally non-polarizable dark electrode for that same half-reaction (Figure 3.1a)*,* the potential difference at a given current is then:

$$E_{dark}(I) - E_{light}(I) = E(A/A^-) - V_{PV}(I) + V_{cat}(I) + V_{mt}(I) + V_{sol}(I)\,) \tag{14}$$

where $V_{PV}(I)$ is the ideal *I-V* characteristic of the photoactive electrode, $V_{cat}(I)$ is the potential loss due to the catalytic overpotential, $V_{mt}(I)$ is the potential loss due to mass transport, and $V_{sol}(I)$ is the potential loss due to ohmic solution resistance. $E_{light}(I)$ and $E_{dark}(I)$ are the voltammetric *I-E* measurements of the working photoactive electrode of interest and the dark electrode of comparison, respectively. Equation 14 contains no potential drops for the dark electrode because an ideally non-polarizable electrode remains at a fixed electrochemical potential regardless of the current flowing through the interface. The potential of the electrodes is controlled by an external control source, such as a potentiostat.

Multiplying by the current and dividing by the input solar power yields:

$$\phi_{saved,ideal} = \frac{I*[V_{PV}(I)-(V_{cat}(I)+V_{mt}(I)+V_{sol}(I))]}{P_s} \tag{15}$$

In the example from Figure 3.1a, the ratiometric power-saved at the maximum power point is $\phi_{\mathrm{saved,ideal}} = 0.008$ A x (1.23V-0.71 V) / $P_{\mathrm{s}} = 4.2\%$ for $P_{\mathrm{s}} = 0.1$ W cm^{-2}. The value of $\phi_{\mathrm{saved,ideal}}$ has often been designated as an efficiency, sometimes called the thermodynamic energy conversion efficiency and other times, if corrected for concentration overpotentials and uncompensated resistance losses, called the intrinsic photoactive electrode efficiency. However, neither quantity as calculated is an actual system efficiency, because the calculated quantities do not represent a ratio between the total power output by, and total power input into, a full system. The value of $\phi_{\mathrm{saved,ideal}}$ can, however, be used to obtain a specific type of system efficiency, provided that the working photoactive electrode is used in conjunction with an ideally nonpolarizable counterelectrode in an ideal electrochemical cell, as described in section VI.A below.

3.4.4.2 Power-Saved Measurements Relative to a State-of-the-Art Dark Electrode

The photoactive electrode power saved can also be calculated with respect to a state-of-the-art dark electrode for the half-reaction of interest (Figure 3.1b, $\phi_{\mathrm{saved,SOA}}$). The potential difference at a given current is then:

$$E_{dark,SOA}(I) - E_{light}(I) = \left(V_{cat,dark}(I) - V_{cat,light}(I)\right) + \left(V_{mt,dark}(I) - V_{mt,light}(I)\right) + V_{PV}(I) \tag{16}$$

where $V_{\mathrm{cat,dark}}(I)$ and $V_{\mathrm{mt,dark}}(I)$ are the potential losses due to catalysis and mass transport, respectively, at the state-of-the-art dark electrode, $V_{\mathrm{cat,light}}(I)$ and $V_{\mathrm{mt,light}}(I)$ are the potential losses due to catalysis and mass transport, respectively, at the photoactive electrode, and $E_{\mathrm{dark,SOA}}(I)$ is the voltammetric *I-E* measurement of the state-of-the-art dark electrode of comparison.

As seen in Equation (16), comparison of a photoactive electrode to a state-of-the-art dark electrode takes into account any differences in the catalytic activities of the electrodes, any differences in mass transport to the electrode surfaces, and accounts for the photovoltage generated by the photoactive electrode. In the example from Figure 3.1b, the measured ratiometric power-saved at the maximum power point is $\phi_{\mathrm{saved,SOA}} = 0.008\text{ A} \times (1.23\text{ V}+0.10\text{ V}-0.71\text{ V}) / P_{\mathrm{s}} = 5.0\%$.

3.4.4.3 Power-Saved Measurements Relative to a Dark Degenerately Doped Catalytic Anode to Isolate the Photovoltage-Current Performance of a Photoactive Electrode

The photoeffects produced by an illuminated photoactive electrode can be isolated from catalytic losses or from cell resistance or concentration overpotential losses by use of a non-photoactive version of the illuminated electrode of interest (*e.g.* a p$^+$-Si dark anode compared to an n-Si illuminated photoanode) as the dark electrode for a three-electrode power-saved measurement. In this case (Figure 3.1c), in an otherwise identical 3-electrode electrochemical cell, the power saved ($\phi_{saved,NPA,C}$) (NPA,C = non-photoactive, identical catalyst) calculated by subtraction of E_{light}, the potential applied to the photoactive electrode, from the value of E_{dark} exhibited by a non-photoactive dark electrode, both at a given current I, is given by:

$$E_{dark}(I) - E_{light}(I) =$$

$$(E(A/A^-) - V_{PV}(I) + V_{cat}(I) + V_{mt}(I) + V_{sol}(I)) - (E(A/A^-) + V_{cat}(I) + V_{mt}(I) + V_{sol}(I))$$

$$= V_{\mathrm{PV}}(I) \tag{17}$$

where the photopotentials in Equation 17 have been broken down into the various components that represent the photovoltaic component, V_{PV}, the overpotential due to electrocatalytic losses, V_{cat}, the overpotential due to mass transport losses/concentration overpotentials, V_{mt}, and the voltage losses due to uncompensated solution resistance, V_{sol}. $E(A/A^-)$ is the Nernstian potential of the half-reaction being performed at the working electrode. The value of V_{saved} produced by such a calculation isolates the photovoltage

$V_{PV}(I)$ generated by the photoactive electrode in the limit where the catalytic/mass transport behavior of the photoactive working electrode and of the dark working electrode are the same and therefore cancel in the subtraction of E_{dark} from E_{light}. In the example from Figure 3.1c, the measured ratiometric power-saved at the maximum power point is $\phi_{saved,NPA,C} = 0.008$ A x (1.23V+0.2V-0.71V) / $P_s = \phi_{saved,NPA,C} = 5.8\%$.

The *photovoltaic characteristics*, $V_{PV}(I)$, of a photoactive electrode can be described by the diode equation:

$$V_{PV}\ (I) = \frac{nkT}{q} * \ln\left(\frac{|I_{ph}|-I}{|I_0|} + 1\right) \tag{18}$$

where n is the ideality factor of the photodiode, k is Boltzmann's constant, T is the absolute temperature, q is the unsigned elementary charge on an electron, I_{ph} is the light-induced current of the photodiode, and I_0 is the reverse-saturation current of the photodiode. Extraction of the $V_{PV}(I)$ behavior allows analysis that the observed *J-E* performance of the photoactive electrode could equivalently instead be obtained through the use of an external PV cell connected electrically in series with an electrocatalytic dark electrode, with the PV cell required to exhibit specific values of its V_{oc}, short-circuit current, fill factor, and thus an energy-conversion efficiency (as defined by Equation 4).

3.4.4.4 Power-Saved Measurements Relative to Other Types of Working Electrodes

In general, other choices of working electrodes for use in power-saved measurements will yield a convolution of effects due to the photovoltaic properties and catalytic properties, and the photoactive electrode and dark electrodes used in the comparison. For instance, if a degenerately doped photoanode is used as the dark electrode for the power saved measurement[19] [19], the resulting value will also include any overpotentials associated with rectifying behavior of the semiconductor/liquid junction at reverse bias, and possibly ohmic resistance losses between the back contact and the reverse biased semiconductor electrode. The "ideal" degenerately doped dark anode would show none of these losses and thus would ultimately produce an ideally nonpolarizable working electrode. Other degrees of rectification would produce a convolution of the polarization behavior of the dark anode with the photoanode characteristics, making it difficult to extract either pure values for $V_{PV}(I)$, $V_{cat}(I)$, $V_{mt}(I)$, or $V_{sol}(I)$ from the difference between the *J*-*E* behavior of the photoactive electrode and the *J*-*E* behavior of the dark anode. Ideally behaving, non-degenerately doped semiconductor electrodes will exhibit negligible dark current well into reverse bias [20, 23]. In such systems, Equation 18 applies over a wide range of voltages, and hence $J = J_o$ even for very large reverse biases. Therefore, for such systems, the use of the dark *J*-*E* characteristic as a reference for power-saved measurements, relative to the *J*-*E* characteristics for that same photoactive electrode under illumination, will produce misleadingly large power-saved values. For example, an n-Si-based photoanode exhibits negligible dark current even at very large reverse bias potentials [24, 25]. The comparison between the dark anodic current and illuminated anodic photocurrent on the same electrode would in this case result in 'photovoltages' derived from the power-saved calculation that were misleadingly large, and would yield values in excess of the band-gap energy of Si.. Similarly, the use of a dark anode with a very high overpotential for the reaction would inherently include a very large value for $V_{cat,dark}$, which would not provide a consistent basis for calculation of solely either $V_{PV}(I)$, $V_{cat}(I)$, $V_{mt}(I)$, or $V_{sol}(I)$ from a power-saved measurement.

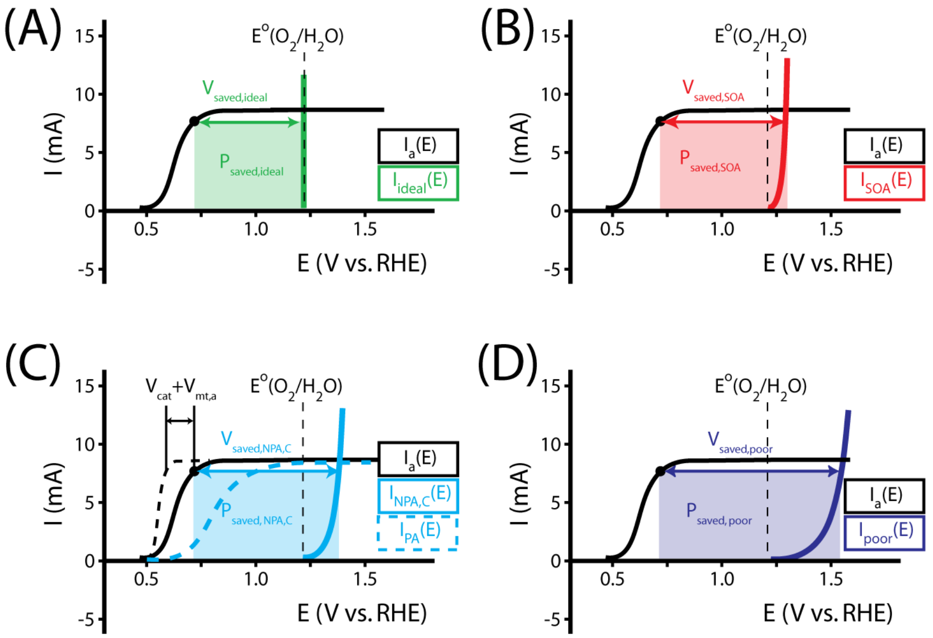

Figure 3.1. Examples demonstrating the effect of the chosen comparison dark electrode on the power-saved figure-of-merit in three-electrode *J-E* measurements. In each example, the same schematic voltammetric *I-E* characteristic (maximum power point designated by a black dot; V_{mp} = 0.71 V vs. RHE, I_{mp} = 8 mA, electrode area = 1cm^2) for the photoanode of interest is compared to a chosen dark electrode performing the same anodic reaction. (A) The power-saved compared to an ideally non-polarizable dark electrode. The measured ratiometric power-saved is $\phi_{saved,ideal}$ = 4.2% (for P_s = 0.1 W cm^{-2}). (B) The power-saved compared to the state-of-the-art dark anode for the water oxidation reaction (see Table 3.1). In this example, the dark electrode exhibits an overpotential of 100 mV at I = 8 mA, increasing the measured ratiometric power-saved value to $\phi_{saved,SOA}$ = 5.0%. (C) The power-saved by the photoanode compared to an identically engineered (semiconductor substrate, structure and mass loading of electrocatalyst, surface, etc.), non-photoactive, degenerately doped electrode (solid blue line). For the example that the catalyst and mass-transport overpotentials are 200 mV for this electrode configuration, and the ratiometric power-saved value is $\phi_{saved,NPA,C}$ = 5.8%. The intrinsic photovoltaic properties of the semiconductor $V_{PV}(I) = E_{dark,NPA,C}(I)\text{-}E_{light}(I)$ (dashed black line). The catalyst/mass transport effects can be observed using a photoactive electrode prepared from the photoactive substrate without added electrocatalyst ($E_{light,PA}(I)$) (dashed blue line, PA = Photoactive). (D) The power-saved for the photoanode compared to a dark electrode with a non-optimal catalytic overpotential for water oxidation. An arbitrarily poor dark electrode can be chosen for comparison, which increases the ratiometric power-saved metric ($\phi_{saved,poor}$ = 6.6% for the example dark electrode with overpotential of 300 mV at 8 mA) without any actual improvement in the photoactive electrode characteristics.

3.5 Predicting System Efficiencies from Three-Electrode Component Measurements

To determine how a particular component will affect the overall efficiency of a system, the most rigorous approach is to physically construct a full system that includes the component in question. However, this method introduces unreasonable barriers to component-level research because only those research groups capable of building and accurately testing full photoelectrochemical systems would then be able to participate in component-level development. Additionally, a lack of standardization in device and system designs can lead to different conclusions between different laboratories regarding the contribution of the same component to the performance of the same device.

An alternative approach is to hypothetically integrate the components into a theoretical, optimized system in which the resistive losses associated with the solution, membrane, and series resistances are negligible. This process allows estimation of an optimal system efficiency for a given photoactive electrode, and the resulting optimal system efficiency value can be compared directly to efficiencies of other full systems. While this optimal system efficiency will always be greater than the measured efficiency for an actual, constructed device, calculation of the optimal system efficiency is nevertheless a valuable evaluation of how individual components will contribute to the system efficiency in an optimized device configuration. Below, we describe a method to determine the optimal system efficiency from half-cell measurements for three different photoelectrochemical systems: 1) an ideal regenerative photoelectrochemical cell, 2) a photoassisted electrolysis device, and 3) a dual-photoactive electrode photosynthetic cell.

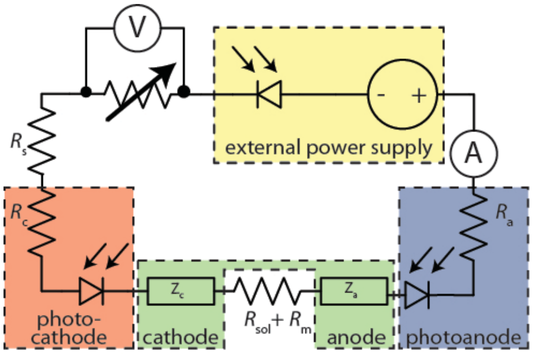

Figure 3.2. An equivalent circuit for a full two-terminal electrochemical system that allows for the inputs of electrical power as well as solar power at various stages. The resistance and impedance characteristics of each electrode can be determined by electrochemical measurements. For a graphical circuit analysis, the relevant electrochemical behavior can be determined from IR-corrected, three electrode *J-E* measurements.

3.5.1 Graphical Circuit Analysis For Identifying System Efficiencies From Three-Electrode Measurements

Figure 3.2 shows an equivalent circuit diagram for a two-electrode system. The photoelectrochemical characteristics of a photoanode/anode and of a photocathode/cathode components are determined by their representative individual *IR*-corrected *J-E* measurements. To perform the graphical circuit analysis, the cathodic *J-E* characteristic (referenced to the Nernstian potential of the reaction at the cathode) is reflected across the x-axis and translated by V_{app}, thus crossing the anodic *J-E* characteristic (referenced to the Nernstian potential of the reaction at the anode). The *operating current* I_{op} can be identified by the intersection point at which the current has the same absolute value through the anode and through the cathode. This constraint can be understood as a requirement of Kirchoff's current law that the current through each electrode must be the same. The value of the efficiency at zero applied bias and the applied bias that results in the maximum efficiency can then both be readily computed. This method is analogous to typical load-line analyses of photovoltaic cells and resistive loads. The *J-E* behavior of an electrode is obviously dependent on the composition of the solution including the concentration of both electrolyte and gaseous species, the incident illumination on the electrode, and the temperature of the cell, among other factors. Whenever possible, the three-electrode measurements used in the graphical circuit analysis to produce predicted optimal system efficiencies should therefore be obtained under the same conditions that the electrode will experience during steady-state operation in the relevant two-electrode device. If both of the three-electrode measurements are not obtained under the same solution conditions (e.g. different counter ions, different pH, etc.) except for any separated products that may appear at one electrode but not the other (e.g. O_2 gas at an anode and H_2 gas at a cathode), correction for any junction potential that would form or equilibration of electrolyte that would take place in the two-electrode device is necessary.

3.5.1.1 Ideal Regenerative Cell Efficiency

Figure 3.3 shows the graphical circuit analysis for an ideally nonpolarizable counter electrode performing the same chemical half-reaction (but in the opposite direction chemically) as is being performed by the working electrode. This system constitutes a regenerative photoelectrochemical cell, in which input solar power produces only electrical power as the output, with no net chemical change in the components of the cell itself.

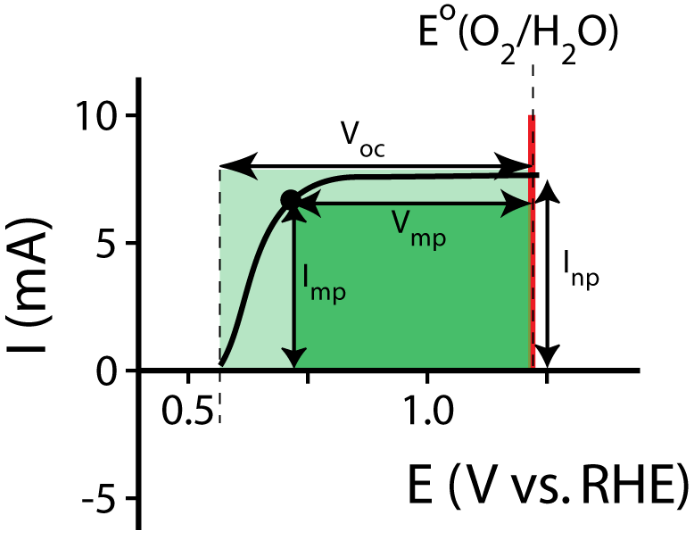

Figure 3.3. The calculation of the intrinsic regenerative cell efficiency, η_{IRC}, of an example photoanode in a configuration where water is being oxidized at the photoanode (black), and oxygen is being reduced at an ideally polarizable counter electrode (red). The system efficiency η_{IRC} can be calculated from the output power at the maximum power point, indicated by the black dot on the voltammagram of the photoanode.

These conditions are fully analogous to those of a solid-state photovoltaic cell, and therefore the same equation is used as the relationship that describes the efficiency of a PV device:

$$\eta_{IRC} = \frac{V_{mp} * I_{mp}}{P_s} = \frac{I(E(A/A^-)) * V_{oc} * ff}{P_s} \qquad (19)$$

where $\eta_{IRC}$is the *ideal regenerative cell efficiency*. The values of V_{oc} and $I(E(A/A^-))$ in Equation 19 are both referenced to the equilibrium potential of the half-reaction being performed at the photoactive electrode. The fill factor (*ff*) is the ratio of the power out at the maximum power point (V_{mp} x I_{mp}) to the product V_{oc} x $I(E(A/A^-))$. The fill factor is a common metric used to quantify the fraction of the theoretical maximum power that is achieved from a photovoltaic, and is determined from a *I-E* measurement corrected for the solution potential drop (V_{sol}) and also possibly for any correctable (see below) mass-transport-derived voltage losses (V_{mt}). The value of η_{IRC} is a true system efficiency that, by construction, is numerically equal to $\phi_{saved,ideal}$ (Equation (19)) calculated from 3-electrode measurements as described in section IV.4.

The η_{IRC} efficiency shares similarities with the two-electrode Φ_{ABPC} metric. As noted earlier, the voltage used to obtain a value for η_{IRC} is exactly the load voltage. Because η_{IRC} is designed to describe the behavior of a regenerative cell, the load is adjustable. However, the load is not adjustable for the fuel-forming systems that Φ_{ABPC} is used to describe. For fuel-forming reactions, in general, the free energy of formation of the chemical fuel is the load in an electrochemical solar-driven water-splitting cell. Thus, for water splitting, a value of 1.23 V is used for the load. This value appears in Equation 9, and the $\mathbf{\Phi_{ABPC}}$ metric and η_{IRC} would thus have mutually identical numerical values for a fuel-forming system in which $V_{ext} = 0$ and for which the counter electrode was ideally non-polarizable.

3.5.1.2 Optimal System Efficiencies

An *optimal system efficiency*, η_{opt}, can be defined for a system that consists of the specified working photoactive electrode and an optimized, state-of-the-art counter electrode that has explicitly stated component-level performance characteristics, while assuming that all other voltage losses are negligible. The merit of this approach is that it produces a standardized, self-consistent set of calculated solar-conversion efficiencies for a theoretical, optimized full system based on the measured properties of a half-cell photoactive electrode.

Here, we propose the use of Pt and RuO_2 as state-of-the-art cathodic and anodic counter electrodes, respectively, for the purpose of calculating optimized system efficiencies based on measurements of half-cell *I-E* characteristics. The performance characteristics of these suggested counter electrode materials are shown in Table 3.1. The parameters j_0 and b are the exchange current density and Tafel slope, respectively, that fit the overpotential-current density relationship of the exemplary planar dark electrocatalysts [1]. The data in Table 3.1 were taken from previously reported electrochemical data on prepared Pt and RuO_2 electrodes. The electrodes should be prepared using the same methods (see references in Table 3.1) to avoid any convolution of electrochemical activity with differences in catalyst structuring. Additionally, any future improvements on the preparation of these or other electrodes for HER and OER should supersede the data in this table. Other reference systems can be used instead, but their equivalent electrochemical parameters should be clearly specified when calculating such optimal solar-conversion efficiencies.

Table 3.1 Performance characteristics of state-of-the-art cathodic (Pt) and anodic (RuO_2) counter electrodes.

Electrode	Electrolyte	$J_0 = \frac{I_0}{A}$ / mA cm$^{-2}_{geo}$	$b = \frac{2.3RT}{\alpha\, n_e F}$ /V decade^{-1}	Ref
Pt	Acid	1^a	0.035^a	[26-28]
Pt	Base	0.7	0.120	[29]
RuO_2	Acid	10^{-5}	0.035	[30, 31]
RuO_2	Base	10^{-5}	0.042	[32]

[a] Note that the kinetic parameters used here to describe the performance of Pt in acid are summarized from studies conducted with planar Pt electrodes, which are appropriate as engineering parameters that approximate the measured Tafel behavior for a planar electrode. It has been suggested that planar Pt electrodes are sufficiently active in acidic conditions such that their kinetic parameters are analogous to the calculated Nernstian diffusion overpotential assuming infinitely fast reaction kinetics, and are therefore may not be related to the true kinetics of the underlying reaction.[29, 33]. Note that for this table, the expected overpotential can be calculated using the equation $\eta = b * log\left(\frac{I}{I_o}\right)$.

The solar-conversion efficiency of the optimized half-cell is then readily calculated (Equation 5), by assuming that the series resistances are zero and using the measured photoactive electrode characteristics in conjunction with the assumed counter electrode behavior, in conjunction with the definition of a system efficiency presented in Equation (3).

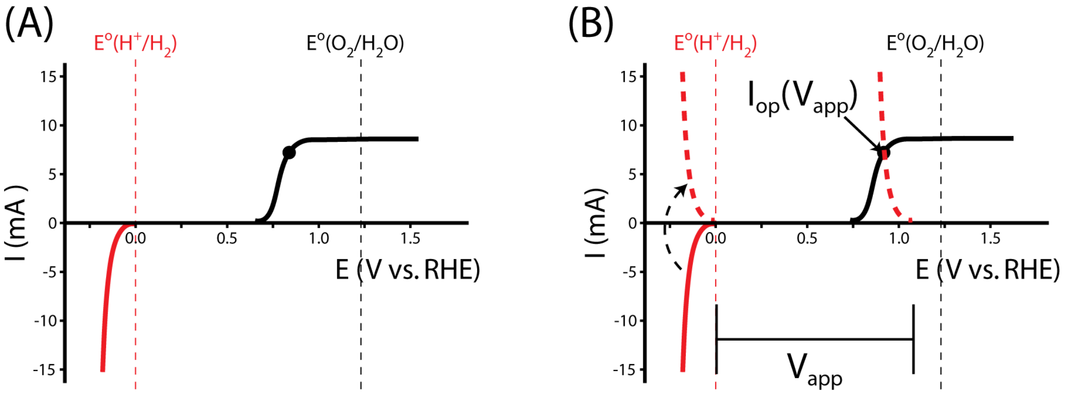

Figure 3.4. Graphical circuit analysis for a photoanode performing photo-assisted water electrolysis. (A) The characteristic three-electrode *I-E* voltammograms for a photoanode (black, positive current densities) and dark cathode (red, negative current densities). (B) A graphical circuit analysis example to determine the value for the bias-assisted (V_{app}) operating current at the maximum power point (black dot) of a photoelectrochemical system constructed from the photoactive electrodes in (A). This relationship is found by inverting the *I-E* voltammogram for the dark cathode, and shifting the resulting voltammogram by an applied potential (dashed red line) to find the operating current $I_{op}(V_{app})$ at that applied potential.

3.5.1.3 Photoelectrosynthetic Cell Efficiencies

In general, semiconductors that utilize a significant portion of the solar spectrum do not provide sufficient photovoltage, or have the correct valence/conduction band-edge alignment, to simultaneously perform the hydrogen-evolution and water-oxidation reactions when in contact with an aqueous electrolyte. For instance, to split water, semiconductors such as Si, WO_3, and Fe_2O_3 require an external bias to a counter electrode. Figure 3.4a shows a typical *I-E* characteristic of a photoanode in alkaline electrolytes, along with a Pt cathode that acts as the counter electrode and is the state-of-the-art hydrogen-evolving cathode in this hypothetical system.

The graphical circuit analysis can be used to determine the efficiency of a system that used this photoactive electrode. Figure 3.4b shows the shifted cathodic voltammogram required to determine the operating current as a function of the applied bias: $I_{op}(V_{app})$. The system has negligible operating current until sufficient bias is supplied. In this example, the $I_{op}(V_{app})$ relationship can be used to find the efficiency of this system for a given bias V_{app} from Equation (3) :

$$\eta_{opt}(V_{app}) = \frac{\boldsymbol{I_{op}}(V_{app})[C\ s^{-1}] * \Delta G[J\ C^{-1}] * \varepsilon_{elec}}{I_{op}(V_{app}) * V_{app} + P_s[W\ cm^{-2}] * A[cm^2]} \tag{20}$$

where ΔG is the Gibbs free energy supplied to water splitting, ε_{elec} is the Faradaic efficiency of the heterogeneous reaction and P_s is the power supplied by the illumination.

The properties of the counter electrode used in this analysis can be measured directly in another three-electrode measurement. Typically, η_{opt} at zero applied bias can be calculated as $\eta_{\text{opt}}(V_{app}=0)$. However, the current is negligible for this example when $V_{app}=0$, and thus there is no reason to calculate the value of η_{opt} at zero bias in this system.

3.5.1.4 Dual Photoactive Electrode System Efficiencies

The value of η_{opt} for a Z-scheme system composed of a photoanode and photocathode independently performing water oxidation and hydrogen evolution reactions, respectively, is possible with the graphical circuit analysis as well, though some additional considerations must be made for the conditions under which the "representative" *J-E* measurements are performed.[34, 35] One example of a Z-scheme is a system in which the photoanode and photocathode are arranged in a side-by-side configuration under illumination [36]. As each photoactive electrode has an independent surface area, the P_s must be appropriately adjusted to calculate the proper efficiency. Another device architecture consists of two semiconductors in series with respect to the incident illumination, rather than in parallel such as in the side-by-side cell arrangement. Voltammograms should be measured for the second material that account for the reduced illumination intensity due to absorption in the first material. For planar materials, this attenuation can be accounted for by using an optical high-pass filter to emulate the first absorber (with a cut-off energy corresponding to the band-gap energy of the top absorber) in the measured voltammogram of the second absorber. For structured electrodes, this characteristic becomes difficult to account for, but this issue should be addressed in any report of η_{opt}.

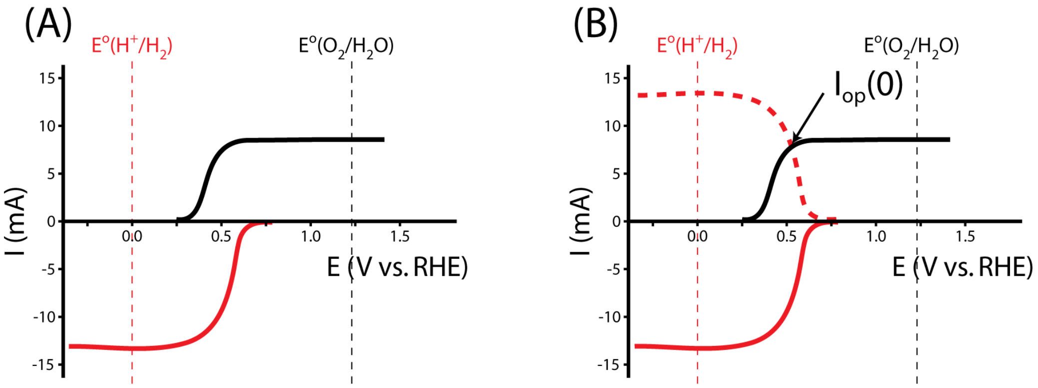

Figure 3.5. Graphical circuit analysis for a Z-scheme architecture comprised of a hypothetical photoanode and photocathode pair. (A) Characteristic three-electrode *I-E* voltammograms for the photoanode (black, positive current densities) and photocathode (red, negative current densities). (B) A graphical circuit analysis example to determine the value for the bias-free operating current $I_{op}(0)$ of a Z-scheme system constructed from the photoactive electrodes in (A).

Figure 3.5a shows the relevant *I-E* measurements for the example photocathode and photoanode materials under the same operating conditions. The intersection of the transformed photocathode voltammogram and the photoanode voltammogram in Figure 3.5b indicates the J_{op} for which η_{opt} can be calculated.

The power output at the current density $I_{op}(0)$ is given by:

$$P_{f,o} = I_{op}(0) * \Delta G \qquad (21)$$

where ΔG is the difference of the thermodynamic half-cell potentials of the electrochemical reactions at the cathode and anode. The overall full photosynthetic system efficiency is then given by:

$$\eta_{FP,opt} = \frac{I_{op}(0) * \Delta G}{P_S} \qquad (22)$$

For a solar-driven water-splitting system, the overall system efficiency is then given by:

$$\eta_{STH,opt} = \frac{I_{op}(0) * 1.23\ V}{P_S} \qquad (23)$$

Equation 23 is analogous to Equation 5 if the sole output is chemical fuel with assumed 100% faradaic efficiency for hydrogen and oxygen production. The dual-electrode scheme can, and has been, used to effect other reactions as well, including HBr and HI splitting [37, 38].

3.6 System Design Considerations

3.6.1 Relating Changes In Component Performance To Changes In Projected System Efficiency

The graphical circuit analysis is required because neither Φ_{ABPC} nor power-saved measurements are robust predictors of system efficiencies. Consider, for example, the five hypothetical photoanodes shown in Figure 3.5 as photoactive electrodes for oxygen evolution in 1 M H_2SO_4(aq). Table 3.2 presents the ratiometric power-saved figure-of-merit, as well as the value of Φ_{ABPC}, and the optimal system solar-conversion efficiency, $\eta_{opt,}$ based on the half-cell performance of each electrode.

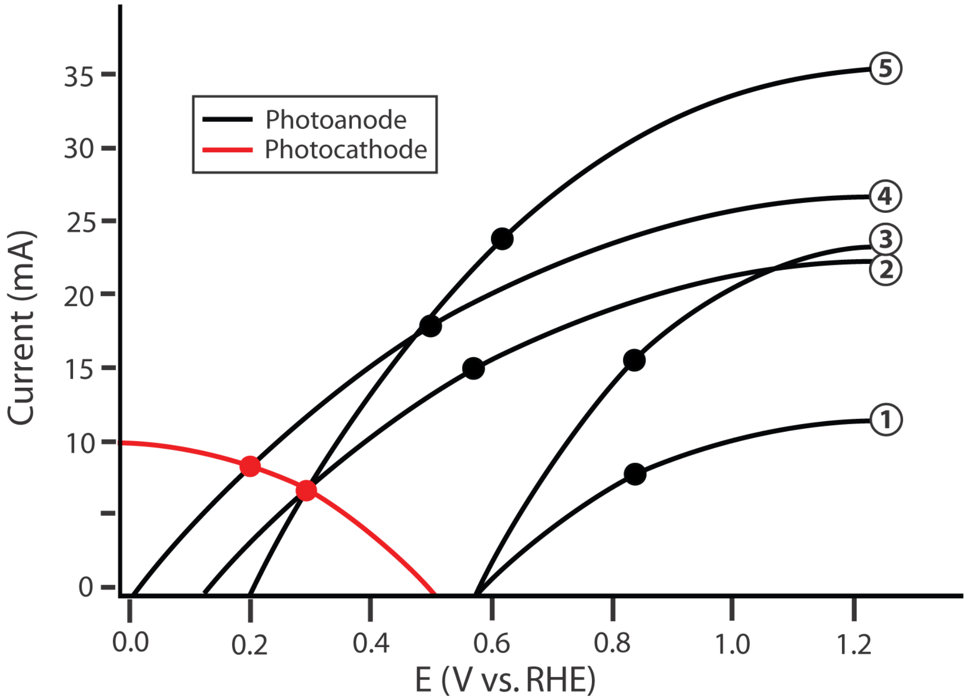

Figure 3.6. Schematic graphical circuit analysis showing five separate photoanodes (numbered on the right) and a single photocathode. The values in Table 3.2 are calculated based on this plot. The black points represent the maximum power point of each individual curve.

Electrode	V_{mp} / V	I_{mp} / mA	$\phi_{\mathrm{ABPC,opt}}{}^{a}$ / %	$\phi_{\mathrm{saved}}{}^{b}$ / %	$\eta_{\mathrm{PAE,opt}}{}^{a}$ / %	I_{op} / mA	$\eta_{\mathrm{STH,opt}}$/ %
1	0.84	7.67	2.75	4.57	8.84	-	0.00
2	0.57	14.96	9.26	13.1	16.9	6.62	8.14
3	0.84	15.58	5.43	9.46	16.9	-	0.00
4	0.50	17.94	12.3	17.0	20.1	8.39	10.3
5	0.62	23.79	13.4	19.8	25.2	6.62	8.14

[a]Assumes an optimized Pt counter electrode with the performance metrics of Table 3.1.
[b]Compared to an optimized, state-of-the-art dark RuO_2 electrode.

Table 3.2. Half-cell performance metrics of the five photoanodes shown in figure 3.5, as well as full-cell optimal system efficiencies when each photoanode is paired either with a state-of-the-art dark counter electrode or instead with the example photocathode whose *I-E* characteristic is shown in figure 3.6.

Clearly, the model *I-E* characteristics show disparities in the efficiency and performance figures-of-merit for the various model photoanodes. However, no individual component efficiency or figure-of-merit is an adequate descriptor of the overall performance of the optimized full system. As shown in figure 3.6, photoanode 5 has the highest Φ_{ABPC} and power-saved (with respect to a state-of-the-art dark electrode) metric values of all of the photoanodes considered. A theoretical water-splitting system consisting of photoanode 3 operating at the maximum power point of the photoactive electrode, in series with an optimal Pt counter electrode and an external bias, has a maximum system efficiency of 16.7%. However, a similar system using photoanode 2 also operates with a system conversion efficiency of 16.7%. Hence, the power-saved figures-of-merit for these two photoanodes do not indicate that the device incorporating photoanode 2 can operate with the same maximum solar-conversion efficiency as a system that instead uses photoanode 3.

A similar issue arises for the relationship between the actual system efficiencies of dual photoactive electrode systems and trends in Φ_{ABPC}, power saved measurements, or even η_{IRC} values. For example, when used in conjunction with the example photocathode to produce a whole system, the system composed of photoanode 5 operates with $\eta_{STH,opt}$ equal to that of the system comprised of photoanode 2. Moreover, using the example photocathode, neither photoanode 1 nor photoanode 3 are capable of providing the photovoltage necessary to operate in a dual-electrode full photosynthetic system with only solar power as the only source of input power. The graphical circuit analysis illustrates that although photoanode 5 yields a higher value of I_{mp} than photoanode 4, the photoanode current is not the limiting factor in this example, because due to its higher photovoltage, photoanode 4 yields a higher η_{STH} than photoanode 5 when paired with the specific photocathode used in the example of Figure 3.6. This issue demonstrates the importance of current matching when combining photoanodes and photocathodes in systems designed for photoelectrolysis.

3.6.2 Limitations of Using STH Efficiencies Relative to Using System Efficiencies

As demonstrated in Table 3.2, there are clear limitations to using η_{STH} as the sole metric for the efficiency of a photovoltaic electrosynthetic or photoelectrochemical device. A motivating example is the case of two high-fill-factor solar cells (eg. GaAs) electrically connected in series driving electrolysis on a dark anode and a dark cathode (Figure 3.7a). In this case, the component characteristics (i.e., the *J-V* characteristics of each photovoltaic) do not change, but the values of the computed figures-of-merit may change significantly when the system is organized in different ways. For example, consider two identical photovoltaic cells that each provide 1.0 V of open-circuit voltage, 28 mA cm^{-2} of short-circuit current density, *ff* = 0.86, have optically active areas of 1 cm^2, and thus each have efficiencies of 24%. The series connection of the two photovoltaics (laid out to cover twice the area of the incident optical plane and thus receive twice the illumination as an individual cell) still has an efficiency of 24%, but produces twice the voltage and the same, matched current through the whole circuit. If an electrolysis unit that is 75% efficient at the 28 mA cm^{-2} current density is then connected with these two series-connected PV cells, the whole system has an efficiency of 18% (0.75 x 0.24), as given by Equation 3.

However, if the identical PV devices were wired individually to electrolysis units and η_{STH} was calculated by treating the whole set of components as a full system, various values would be obtained for different configurations of the identical components. Specifically, if only one PV unit was wired to an electrolysis unit and the other was unused, η_{STH} would be undefined, because η_{STH} is limited to systems in which the production of H_2 occurs spontaneously with only sunlight as the input power source, and the single PV unit does not provide sufficient voltage to perform water splitting. If the second PV was wired in series with the first and connected to the remainder of the system components, η_{STH} would then be calculated to be (28 / 2) x 1.23 = 17.4%, provided that the electrolyzer was 75% efficient at the operating current density. If instead the electrolyzer were 60% efficient, which would require operation at a total of 1.23 V / 60% = 2.05 V, η_{STH} would again be undefined, since the total open-circuit photovoltage of 2.0 V produced by both of the PV cells connected electrically in series would be insufficient to spontaneously drive the water-splitting process and thus no electrolysis current would result.

Note that in each case, however, if additional electrical power inputs and electrical power outputs were considered, the general expression of Equation 3 for the system efficiency and Equation 4 for the solar energy-conversion efficiency would be applicable in each instance, and hence would provide for a consistent basis for comparison of the performance of these different systems.

Specifically, the system can be analyzed with the graphical circuit method by dividing the system into a tandem configuration consisting of a single PV-oxygen-evolving-photoanode and a PV-hydrogen-evolving-photocathode. Separate voltammetric measurements in a three-electrode configuration can be used for each of these two components, as shown in figure 3.7a. Figure 3.7b shows the *J-E* characteristics of each electrode in this schematic example. The potential of each electrode is defined relative to the fuel-forming reaction it performs, so the operating current for a water splitting system built from these electrodes can be evaluated from the graphical circuit analysis. Neither electrode is capable of performing the full water-splitting reaction with only a dark counter electrode, but together both electrodes are able to drive water splitting when configured in tandem. The graphical circuit analysis shown in figure 3.7c demonstrates that an operating current can be found and the STH efficiency can be calculated from that quantity.

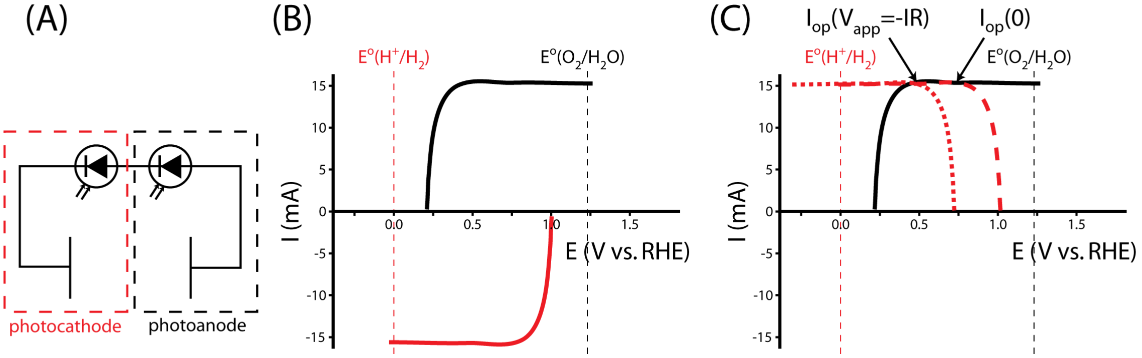

Figure 3.7. (A) The circuit diagram for a tandem photovoltaic system powering the dark electrolysis of water. (B) Schematic voltammograms for the photoanode (blue) and photocathode (red) electrodes. These voltammograms are representative of GaAs photovoltaic cells coupled in series to a hydrogen-evolving electrocatalyst (cathode) or to an oxygen-evolving electrocatalyst (anode). (C) The graphical circuit analysis of the voltammograms in (B). As each voltammogram is relatively flat near the operating current I_{op}, the addition of a resistive load to the series circuit ($I_{\mathrm{op}}(V_{\mathrm{app}} = -IR)$, dotted red line) results in a very similar operating current and STH efficiency as the system at short circuit with no load ($I_{\mathrm{op}}(0)$, dashed red line), with additional electrical power being generated.

The tandem system provides a relatively large overvoltage for water splitting, which reduces the STH efficiency of the system compared to the solar-to-electricity efficiency that would be measured if the two PV units were connected in series across an optimized electrical load. Figure 3.7c shows that the voltammograms are relatively flat in the region of the operating point, due to attaining their light-limited operating current. An electrical load can be added to the series circuit, which draws excess power without significantly affecting the operating current driving water splitting. In the graphical circuit analysis, the effect of the load drawing excess power is represented by shifting the transformed voltammogram of the photocathode to more negative potentials, effectively acting as a negative applied bias that can be utilized as electrical power. But more practically, this behavior demonstrates the necessity of load matching in solar fuels applications. A system designed from PV elements as described here would have a much higher efficiency if the architecture of the system matched the power supplied by the photocurrent-generating electrodes. A network of identical photoactive electrodes, current/voltage transformers, and electrolysis units can be assembled to minimize these overvoltages, maximizing η_{STH} without any alteration to the PEC characteristics of the photoactive electrodes [39]. It is difficult to determine the optimal system architecture from a direct STH measurement, because the PEC performance of the electrode is convoluted with the design of the experimental system. The system architecture effects are eliminated in the calculation of η_{opt} from three-electrode cyclic voltammetry measurements, thereby allowing for the absolute ceiling of efficiency to be calculated for that specific photoactive electrode or combination of electrodes. The value of η_{opt} calculated in this way is a significant metric by which to judge the technological potential of any photoactive electrode for performing solar-driven, fuel-forming reactions.

3.6.3 Systems-Level Considerations for Comparison Between Efficiencies of Different Types of Photoelectrosynthetic Cells

The systems described herein are generally part of larger processes, which may include energy needed to provide suitably pure input water streams, conditioning and pressurization of the output gas stream, and other processes involved with the storage, transportation, and utilization of the fuel[40, 41]. The overall process efficiency will be affected by many variables; for instance a 12% efficient solar-driven water-splitting system that produces H_2(g) at 1 atm pressure and thus requires a relatively inefficient 3-stage compressor to produce pressurized H_2(g) at the factory gate may be less preferred than a 10% efficient solar-driven water-splitting system that utilizes electrochemical compression and thus allows the use of a much more efficient two-stage compressor as part of the process. The key attributes of the system of interest must thus be clearly specified so that their utility in larger processes can be evaluated on a consistent basis.

A second level of complexity is introduced in assessing the efficiency of a system that produces separated fuels from a system that co-evolves the gases in a mixture in the effluent stream. To be useful in a fuel cell, for example, or in a controllable combustion-based device, the gases must be separated and thus entropy is involved as well as energy inputs. Additionally, in the specific case of solar-driven water splitting (and likely in general for any fuel production), the H_2 concentration in the O_2 (and vice versa) must never exceed the lower explosive limits at any point in the system, to be qualified as intrinsically safe and therefore to be practical and deployable (or even demonstrated at significant scale). The energy required to separate the products must therefore be included in any overall system efficiency measurement to provide a valid comparison between the system-level efficiency of a system that produces separate, pure gas streams relative to a system that co-evolves the gases. Additionally, due to impediments to practical implementation, systems that are not intrinsically safe should be so designated, and cannot directly be compared in efficiency to systems that are intrinsically safe.

A related, third level of complexity is that in the case of solar-driven water splitting, a pressure differential along a pipeline infrastructure is required to beneficially collect the H_2 for use, and a further pressurization is required to supply, utilize, and distribute the H_2 for conversion or other end-use. The efficiency of a mechanical compressor is a strong function of the ratio of the input and output pressures of the compressed gas, whereas electrochemical compression is inherently more efficient than mechanical compression. Therefore, energy-conversion efficiencies at the systems level need to specify the output pressure of the (acceptably pure) H_2 gas stream and will need to remain functional as a system under pressure differentials that vary in both space and time.

3.7 Conclusion

The key system-level figure-of-merit for power-conversion systems is the *system efficiency,* η, obtained from the ratio of the total output power in all forms to the total input power in all forms. Use of the system efficiency provides a consistent approach for comparing the performance of various methods for producing fuels and/or electrical power. The system efficiency reduces to the *solar-to-hydrogen efficiency* (η_{STH}) for the special case of a system in which sunlight is the only input power and for which the only useful output power is the hydrogen obtained from solar-driven water splitting; thus, η_{STH} is defined for characterizing this specific type of system.

While efficiencies are the most important measure of the performance of a full system, other single electrode and system metrics provide important characterization of electrode performance. For example, a measured efficiency value does not provide insight into the detailed behavior of individual components within the system, and therefore pathways to improvement can be obscured. This issue is particularly relevant to photoelectrochemical systems for fuel or electricity production, where dual electrodes must be independently optimized to operate in tandem within the electrochemical device. Three-electrode electrochemical measurements should be used to probe the *J-E* behavior of a specific working electrode. To compare performance among individual electrodes, a variety of figures-of-merit have been discussed, each of which has a useful role, provided that they are clearly specified and quoted in the appropriate context.

The *ideal regenerative cell efficiency* (η_{IRC}) is defined as the efficiency of a photoactive electrode component after correcting for the mass transport and uncompensated resistance overpotentials that arise because of the geometry of the electrochemical cell and used in conjunction with an ideally polarizable counterelectrode that is performing the reverse half-reaction of that performed at the photoactive electrode. This figure-of-merit can be readily reproduced between laboratories, does not require constraints regarding cell design, and is not a function of the properties of the counter electrode used in the measurement. As the name suggests, η_{IRC} is designed to yield a standardized measure of the combined photo- and catalytic performance of a photoactive electrode, and is thus suitable for comparing performance between electrodes for fuel- and electricity-forming systems.

The *ratiometric power-saved* (ϕ_{saved}) figure-of-merit can also be used to decouple the fundamental properties of electrodes from systems engineering considerations. This figure-of-merit provides a comparison between behavior of a photoactive electrode under illumination and that of an appropriately chosen dark electrode. ϕ_{saved} yields different information depending on the dark electrode chosen for comparison, as demonstrated in Figure 3.1. If a state-of-the-art catalytic electrode for the reaction of interest is used for comparison (Table 3.1), $\phi_{saved,SOA}$ is a measure of the combined photo- and catalytic performance of a photoactive electrode. Alternatively, if a non-photoactive and oppositely and degenerately doped version of a photoactive electrode is used for comparison, $\phi_{saved,NPAC}$ is a measure of the fundamental photovoltaic performance of the photoactive electrode, because other losses in the cell (uncompensated solution resistance, mass transfer overpotential, catalytic overpotential, etc.) make identical contributions to each measurement and therefore cancel in the comparison. A judicious choice of the dark electrode must be made and specified for this calculation, as improper choices can result in arbitrarily high values of ϕ_{saved}.

A third component metric, the *applied bias photon-to-current* figure-of-merit (Φ_{ABPC}), is useful for isolating the contribution of the photovoltage of an electrode to the energy stored in the chemical products produced by the system. For systems that produce fuel from sunlight and that do not require an applied bias, Φ_{ABPC} reduces to the solar-to-fuel efficiency (such as η_{STH}).

Graphical circuit analysis methods, where three-electrode voltammograms from two different (photo)electrodes are combined on one plot, and where the crossing point of the curves is the optimal operating current of the system (which is dependent on the applied bias) are required to predict system efficiencies from individual three-electrode *I*-*E* measurements. This information can be used to calculate an *optimal system efficiency*, η_{opt}, which represents the maximum possible efficiency attainable when these two electrodes are combined into a system. Such a method is useful because it is often difficult to build and test a full system, but a graphical circuit analysis allows for optimal efficiencies to be estimated based on separate three-electrode measurements of individual photoactive electrodes. This method also offers the benefit of highlighting how changes within a single component electrode would affect the estimated efficiency of a full STH system, thus indicating effective utilization strategies for optimizing these components towards improving full system performance.

The various metrics described and discussed herein yield different information and all have some utility, in the proper context, for characterizing electrodes or systems for photoelectrochemical energy conversion. It is imperative that researchers choose appropriate metrics to describe the performance of electrodes and materials for such systems, and that the measurements and methods used to calculate efficiencies and figures-of-merit are properly described and denoted in full. Such an approach is critical to facilitate accurate comparisons between laboratories, and to therefore accelerate progress in the field.

TABLE 3.3:
Names and Definitions for System, Subsystem, and Component Efficiencies

System Efficiencies		
η	General expression	$\frac{P_{f,o} + P_{e,o}}{P_s + P_{e,i}}$
η_{PV}	Photovoltaic system efficiency (Solar to Electricity)	$\frac{P_{e,o}}{P_s} = \frac{I \cdot V}{P_s}$
η_{STF}	Solar-to-fuels efficiency	$\frac{P_{f,o}}{P_s} = \frac{A\,[cm^2]\,J_{sc}\,[A\,cm^{-2}] \cdot E_{f,o}[V] \cdot \varepsilon_{elec}}{P_s\,[W]}$
η_{STH}	Solar-to-hydrogen efficiency	$\frac{A\,[cm^2]\,J_{sc}\,[A\,cm^{-2}] \cdot 1.23[V] \cdot \varepsilon_{elec}}{P_s\,[W]}$
$\eta_{\mathrm{electrolyzer}}$	Electrolyzer (Electricity-to-fuels) efficiency	$\frac{P_{f,o}}{P_{e,i}} = \frac{E_f}{V_i}$
η_{PAE}	Photoassisted electrolyzer efficiency	$\frac{P_{f,o}}{P_s + P_{e,i}}$
$\eta_{FP,opt}$	Optimal system efficiency for solar-to-fuel for a full photosynthetic cell	$\frac{I_{op}(0) \cdot \Delta G}{P_s}$
$\eta_{STH,opt}$	Optimal system efficiency for solar-to-hydrogen for a full photosynthetic cell	$\frac{I_{op}(0) \cdot 1.23\,V}{P_s}$
$\eta_{opt}(V_{app})$	System efficiency from a graphical circuit analysis	$\frac{I_{op}(V_{app})[C\,s^{-1}] \cdot \Delta G[J\,C^{-1}] \cdot \varepsilon_{elec}}{I_{op}(V_{app}) \cdot V_{app} + P_s[W\,cm^{-2}] \cdot A[cm^2]}$

Component or Half-Cell Performance Metrics

η_{IRC}	Ideal regenerative cell efficiency	$\frac{V_{mp} \cdot I_{mp}}{P_s} = \frac{I(E(A\,/A^{-}\,)) \cdot V_{oc} \cdot ff}{P_s}$
ϕ_{saved}	Ratiometric power-saved metric	$\frac{I \cdot V_{saved}\ (I)}{P_s}$
ϕ_{ABPC}	Applied-bias photon-to-current component metric	$I_{mp} \cdot \frac{(E_{f,o}\ -\ V_{ext,mp})}{P_s}$

3.8 Glossary

A	geometric surface area
$E(A/A-)$	half-cell Nernst potential for the electrochemical reaction at the electrode referenced to the reference electrode
$E_{dark}(I)$	potential needed to drive a reaction at current I in the dark during three-electrode measurements
$E_{dark,SOA}(I)$	potential needed to drive a reaction at current I on a state-of-the-art dark electrode during three-electrode measurements
$E_{ext}\ (I)$	potential at the working electrode when passing current I referenced to the reference electrode
$E_{f,o}$	potential difference corresponding to the Gibbs free energy difference between the two half-reactions of the fuels being produced
$E_{light}(I)$	potential needed to drive a reaction at current I in the light during three-electrode measurements
E_{oc}	open circuit potential
ff	photovoltaic fill factor
I	current
I_{mp}	current at maximum power point
$I(E(A/A^-))$	current at the Nerstian potential for a half-reaction (corrected for solution composition)
I_0	reverse saturation current of an electrode
I_{op}	system operating current (note that I_{op} can be a function of V_{app}, $I_{op}(V_{app})$
I_{ph}	photogenerated current
I_sc	photovoltaic short circuit current
J	current density
$J(E(A/A^-))$	current density at the Nernstian potential for a half-reaction (corrected for solution composition)
J_{sc}	short-circuit current density
J_{fp}	current density at the formal potential of the half-reaction of interest
J_{op}	system operating current density(note that J_{op} can be a function of V_{app}, $J_{op}(V_{app})$
k	Boltzmann's constant
n	diode ideality factor
P_i	total input power
$P_\mathrm{e,i}$	input electrical power
$P_\mathrm{e,o}$	output power in the form of electricity
$P_\mathrm{f,o}$	output power contained in the chemical fuel
P_{max}	maximium power output of a system or component
P_o	total output power
P_s	input power from solar illumination
$P_{saved}(I)$	power saved at current I
q	elementary charge on an electron

R_a	resistance associated with the anode of a system
R_c	resistance associated with the cathode of a system
R_m	membrane ohmic resistance
R_{sol}	solution ohmic resistance
T	temperature in Kelvin
V_{app}	electrical bias applied to a circuit
$V_{cat}(I)$	catalyst kinetic overpotential at current I
$V_{cat,dark}(I)$	catalyst kinetic overpotential at a dark electrode at current I
$V_{cat,light}(I)$	catalyst kinetic overpotential at a photoactive electrode
$V_{counter}(I)$	overpotential at the counter electrode at current I
$V_{dark}(I)$	external bias values needed to drive a reaction in the dark in a two-electrode system at current I
$V_{e,i}$	external electrical voltage input
V_{ext}	voltage supplied by an external source
$V_{e,o}$	output voltage of the electrical power portion of the total system output
$V_{light}(I)$	external bias values needed to drive the reaction at current *I* in the light in a two-electrode system
V_{mp}	voltage at maximum power point
$V_{mt}(I)$	mass-transport overpotential at current *I*
$V_{mt,dark}$	mass-transport overpotential at a dark electrode at current *I*
$V_{mt,light}$	mass-transport overpotential at a photoactive electrode at current *I*
V_{oc}	photovoltaic open-circuit voltage
$V_{\mathrm{PV}}(I)$	voltage across a photoactive electrode at current *I*
$V_{\mathrm{saved}}(\mathrm{I})$	difference between the external biases needed to drive a reaction at current *I* in the light and the dark on a photoactive working electrode and a related dark working electrode in a three-electrode measurement
$V_{\mathrm{sol}}(I)$	total voltage drop across the solution resistance at current *I*
ΔG	Gibbs free energy per electron of the heterogeneous reaction
ε_{elec}	Faradaic efficiency
η	efficiency
$\eta_{\mathrm{electrolyzer}}$	electrolyzer (electricity-to-fuels) system efficiency
$\eta_{\mathrm{FP,opt}}$	full photosynthetic system efficiency calculated from graphical circuit analysis of half cell performances
η_{IRC}	ideal regenerative cell efficiency
η_{opt}	System efficiency calculated from load-line analysis of half-cell performances
η_{PAE}	photo-assisted electrolyzer system efficiency
η_{PV}	photovoltaic (solar-to-electricity) component performance metric
η_{STF}	solar-to-fuels conversion efficiency
η_{STH}	solar-to-hydrogen conversion efficiency
$\eta_{\mathrm{STH,opt}}$	maximum solar-to-hydrogen conversion efficiency calculated from load-line analysis of half-cell performances
ϕ_{ABPC}	applied bias photon-conversion component metric

ϕ_{saved}	three-electrode power-saved performance metric
$\phi_{saved,ideal}$	three-electrode power-saved performance metric for a photoactive electrode compared to an ideally non-polarizable working electrode
$\phi_{saved,SOA}$	three-electrode power-saved performance metric for a photoactive electrode compared to the state-of-the-art (SOA) dark working electrode for the half-reaction of interest
$\phi_{saved,NPA,C}$	three-electrode power-saved performance metric for a photoactive electrode compared to an identically engineered (catalyst, substrate), but non-photoactive, working electrode (NPA,C = non-photoactive, identical catalyst)
$\phi_{saved,PA}$	three-electrode power-saved performance metric for a photoactive electrode compared to an identically engineered, but non-photoactive, working electrode without a catalyst
$\phi_{saved,poor}$	three-electrode power-saved performance metric for a photoactive electrode compared to a non-state of the art, high-overpotential working electrode

3.9 Acknowledgments

The bulk of this work appeared in *Energy and Environmental Science* in 2015 (DOI: 10.1039/c5ee00777a). I would like to thank Sonja Francis, Matt McDowell, Victoria Dix, and Shawn M. Chatman for their invaluable assistance. I would also like to particularly acknowledge Rob Coridan for his tireless efforts in improving this work.

3.10 References

1. M. G. Walter, E. L. Warren, J. R. McKone, S. W. Boettcher, Q. Mi, E. A. Santori and N. S. Lewis, *Chem. Rev.*, 2010, **110**, 6446-6473.
2. T. J. Jacobsson, V. Fjällström, M. Edoff and T. Edvinsson, *Energy Environ. Sci.*, 2014, **7**, 2056-2070.
3. A. Steinfeld, *Solar Energy*, 2005, **78**, 603-615.
4. M. A. Rosen, *Energy*, 2010, **35**, 1068-1076.
5. Z. Wang, R. R. Roberts, G. F. Naterer and K. S. Gabriel, *Int. J. Hydrogen Energy*, 2012, **37**, 16287-16301.
6. R. E. Blankenship, D. M. Tiede, J. Barber, G. W. Brudvig, G. Fleming, M. Ghirardi, M. R. Gunner, W. Junge, D. M. Kramer, A. Melis, T. A. Moore, C. C. Moser, D. G. Nocera, A. J. Nozik, D. R. Ort, W. W. Parson, R. C. Prince and R. T. Sayre, *Science*, 2011, **332**, 805-809.
7. Z. Chen, T. F. Jaramillo, T. G. Deutsch, A. Kleiman-Shwarsctein, A. J. Forman, N. Gaillard, R. Garland, K. Takanabe, C. Heske, M. Sunkara, E. W. McFarland, K. Domen, E. L. Miller, J. A. Turner and H. N. Dinh, *J. Mater. Res.*, 2010, **25**, 3-16.
8. B. A. Pinaud, J. D. Benck, L. C. Seitz, A. J. Forman, Z. Chen, T. G. Deutsch, B. D. James, K. N. Baum, G. N. Baum, S. Ardo, H. Wang, E. Miller and T. F. Jaramillo, *Energy Environ. Sci.*, 2013, **6**, 1983-2002.
9. J. R. Bolton, S. J. Strickler and J. S. Connolly, *Nature*, 1985, **316**, 495-500.
10. S. Hu, C. Xiang, S. Haussener, A. D. Berger and N. S. Lewis, *Energy Environ. Sci.*, 2013, **6**, 2984-2993.

11. A. C. Nielander, M. R. Shaner, K. M. Papadantonakis, S. A. Francis and N. S. Lewis, *Energy Environ. Sci.*, 2015, **8**, 16-25.

12. O. Khaselev, A. Bansal and J. A. Turner, *Int. J. Hydrogen Energy*, 2001, **26**, 127-132.

13. Z. Chen, H. N. Dinh and E. Miller, *Photoelectrochemical Water Splitting - Standards, Experimental Methods, and Protocols*, Springer, 2013.

14. G. J. Conibeer and B. S. Richards, *Int. J. Hydrogen Energy*, 2007, **32**, 2703-2711.

15. M. S. Wrighton, A. B. Ellis, P. T. Wolczanski, D. L. Morse, H. B. Abrahamson and D. S. Ginley, *J. Am. Chem. Soc.*, 1976, **98**, 2774-2779.

16. B. Parkinson, *Acc. Chem. Res.*, 1984, **17**, 431-437.

17. J. K. Dohrmann and N.-S. Schaaf, *J. Phys. Chem.*, 1992, **96**, 4558-4563.

18. A. J. Bard, R. Memming and B. Miller, *Pure Appl. Chem.*, 1991, **63**, 569-596.

19. H. Dotan, N. Mathews, T. Hisatomi, M. Grätzel and A. Rothschild, *J. Phys. Chem. Lett.*, 2014, **5**, 3330-3334.

20. M. X. Tan, P. E. Laibinis, S. T. Nguyen, J. M. Kesselman, C. E. Stanton and N. S. Lewis, in *Progress in Inorganic Chemistry*, ed. K. D. Karlin, John Wiley & Sons, Inc., 1994, pp. 21-144.

21. A. Heller, *Acc. Chem. Res.*, 1981, **14**, 154-162.

22. A. Heller and R. G. Vadimsky, *Phys. Rev. Lett.*, 1981, **46**, 1153-1156.

23. H. Gerischer, *Electrochimica Acta*, 1990, **35**, 1677-1699.

24. S. Hu, M. R. Shaner, J. A. Beardslee, M. Lichterman, B. S. Brunschwig and N. S. Lewis, *Science*, 2014, **344**, 1005-1009.

25. K. Sun, F. H. Saadi, M. F. Lichterman, W. G. Hale, H.-P. Wang, X. Zhou, N. T. Plymale, S. T. Omelchenko, J.-H. He, K. M. Papadantonakis, B. S. Brunschwig and N. S. Lewis, *Proc. Natl. Acad. Sci. U. S. A.*, 2015, **112**, 3612-3617.
26. J. O. M. Bockris, B. Dandapani, D. Cocke and J. Ghoroghchian, *Int. J. Hydrogen Energy*, 1985, **10**, 179-201.
27. N. M. Marković, B. N. Grgur and P. N. Ross, *J. Phys. Chem. B*, 1997, **101**, 5405-5413.
28. H. Kita, S. Ye and Y. Gao, *J. Electroanal. Chem.*, 1992, **334**, 351-357.
29. W. Sheng, H. A. Gasteiger and Y. Shao-Horn, *J. Electrochem. Soc.*, 2010, **157**, B1529-B1536.
30. G. Lodi, E. Sivieri, A. D. Battisti and S. Trasatti, *J. Appl. Electrochem.*, 1978, **8**, 135-143.
31. S. Haussener, C. Xiang, J. M. Spurgeon, S. Ardo, N. S. Lewis and A. Z. Weber, *Energy Environ. Sci.*, 2012, **5**, 9922-9935.
32. M. E. G. Lyons and S. Floquet, *Phys. Chem. Chem. Phys.*, 2011, **13**, 5314-5335.
33. K. C. Neyerlin, W. Gu, J. Jorne and H. A. Gasteiger, *J. Electrochem. Soc.*, 2007, **154**, B631-B635.
34. M. Grätzel, *Nature*, 2001, **414**, 338-344.
35. Y. Tachibana, L. Vayssieres and J. R. Durrant, *Nat. Photonics*, 2012, **6**, 511-518.
36. S. Licht, in *Semiconductor Electrodes and Photoelectrochemistry*, Wiley, 2002.
37. C. Levy-Clement, A. Heller, W. A. Bonner and B. A. Parkinson, *J. Electrochem. Soc.*, 1982, **129**, 1701-1705.

38. L. Fornarini, A. J. Nozik and B. A. Parkinson, *J. Phys. Chem.*, 1984, **88**, 3238-3243.

39. T. L. Gibson and N. A. Kelly, *Int. J. Hydrogen Energy*, 2008, **33**, 5931-5940.

40. P. Zhai, S. Haussener, J. Ager, R. Sathre, K. Walczak, J. Greenblatt and T. McKone, *Energy Environ. Sci.*, 2013, **6**, 2380-2389.

41. J. A. Herron, J. Kim, A. A. Upadhye, G. W. Huber and C. T. Maravelias, *Energy Environ. Sci.*, 2014, **8**, 126-157.

Chapter 4

Photoelectrochemical Behavior of n-type Si(111) Electrodes Coated With a Single Layer of Graphene

4.1 Introduction and Background

In this chapter, I discuss the behavior of monolayer graphene-coated n-Si photoanodes. The behavior of graphene-coated n-type Si(111 photoanodes was compared to the behavior of H-terminated n-type Si(111) photoanodes in contact with aqueous $K_3[Fe(CN)_6]/K_4[Fe(CN)_6]$ as well as in contact with a series of outer-sphere, one-electron redox couples in non-aqueous electrolytes. The n-Si/Graphene electrodes exhibited stable short-circuit photocurrent densities of over 10 mA cm^{-2} for >1000 s of continuous operation in aqueous electrolytes, whereas n-Si-H electrodes yielded a nearly complete decay of the current density within ~30 s. the values of the open-circuit photovoltages and the flat-band potentials of the Si were a function of both the Fermi level of the graphene and the electrochemical potential of the electrolyte solution, indicating that the n-Si/Graphene interface did not form a buried junction with the solution.

Various strategies have been developed to stabilize photoanodes such as n-Si against photocorrosion or photopassivation in aqueous electrolytes. Thin overlayers of metal have yielded improved anodic stability for silicon and other semiconductors, but generally form semiconductor/metal Schottky barriers that pin the Fermi level of the semiconductor, producing non-optimal photovoltages.[1-7] Furthermore, nearly complete protection from degradation generally requires the deposition of relatively thick metal layers, preventing a significant fraction of incident light from reaching the underlying semiconductor. Insulating barrier layers, such as oxides deposited by atomic layer deposition, or oxides formed via electrochemical anodization processes, can also provide some degree of protection against corrosion.[8-10] However, these oxides generally require deposition of pinhole-free films that form a tunneling barrier to photogenerated holes, in many cases producing a significant series resistance that negatively affects the performance of the resulting photoelectrochemical device. Surface functionalization has led to improvements in the stability of n-Si photoanodes in H_2O-containing non-aqueous solvents, but surface-modification approaches have not yet yielded materials that remain stable under extended anodic operation in aqueous electrolytes.[11-13]

Graphene has the potential to be an almost ideal protection layer for semiconductor photoelectrodes. Graphene can be prepared in nearly pinhole-free large-area layers and has been shown to attenuate the oxidation of metals in air as well as in aqueous electrochemical environments.[14-19] Unlike surface functionalization techniques that are typically specific to a semiconductor and surface plane, graphene layers can be readily applied to a variety of planar electrode surfaces. Graphene also has excellent optical properties, exhibiting ~97% transmission in the visible region of the solar spectrum.[20] Furthermore, graphene has been used in solid-state Schottky junctions capable of generating photocurrent.[21,22,24] The high carrier mobility in the plane of the graphene C-C bonds should allow for lateral transport of carriers to catalytically active sites on the surface of the photoelectrode.[23] The low density of states near the Fermi level of graphene, the chemical inertness of graphene, and the ability to deposit graphene at room temperature and thereby avoid high-temperature interfacial reactions, potentially provide an opportunity to deposit conductive graphene monolayers onto a variety of semiconductor photoanodes, while obtaining desirable photoelectrochemical performance from the resulting solid/liquid junctions.[14,24,25]

4.2 Behavior of graphene-covered n-Si photoelectrodes

Graphene-covered n-Si (n-Si/Gr) electrodes were fabricated by floating graphene that had been grown using chemical vapor deposition (CVD) on to H-terminated n-Si(111) surfaces. X-ray photoelectron spectroscopic (XPS) analysis indicated that this fabrication technique resulted in an intervening 1-2 monolayer thick oxide layer between the silicon and graphene (see Chapter 4 appendix for details).

4.2.1 Stability of graphene-covered n-Si photoanode in aqueous solution

Figure 4.1a depicts the current–density vs. potential (*J*–*E*) behavior in the presence and absence of illumination of n-Si/Gr and n-Si–H electrodes in contact with CH_3CN-5 mM Fc^+-50 mM Fc^0-1.0 M $LiClO_4$. The open-circuit photovoltage, V_{oc}, was 310 mV for Si-H surfaces, and was 260 mV for the n-Si/Gr electrodes. The n-Si/Gr electrodes showed somewhat smaller fill factors (*ff*) than the n-Si–H electrodes, (0.40 vs. 0.64) indicating the presence of a resistance at the n-Si/Gr/CH_3CN contact.

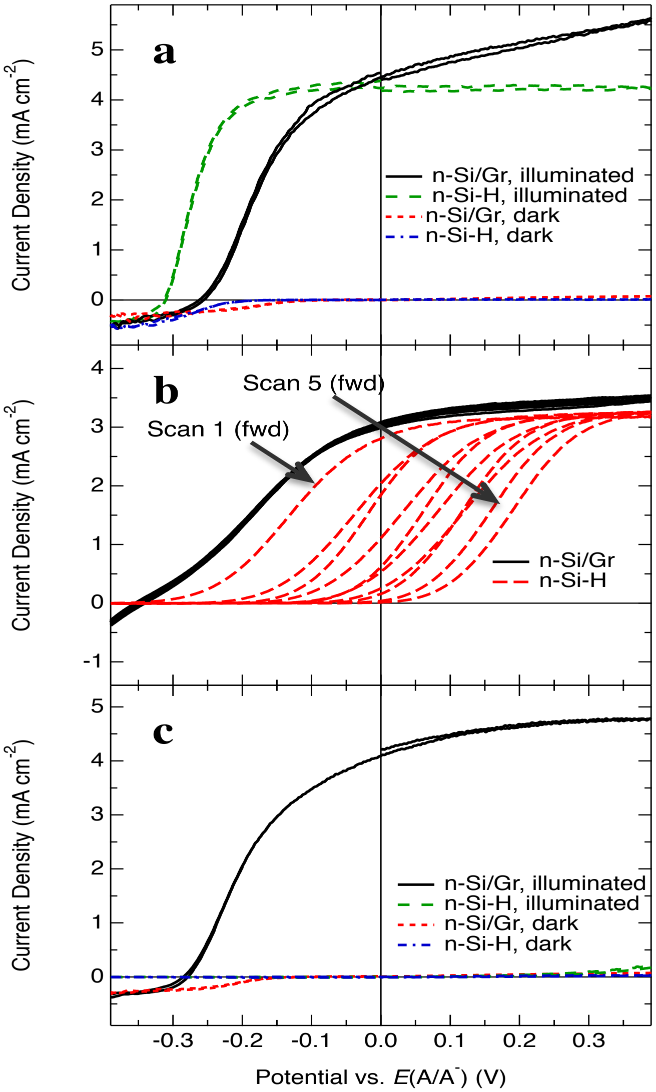

Figure 4.1. (a) *J–E* behavior of freshly fabricated n-Si/Gr and n-Si-H electrodes in contact with CH_3CN-$Fc^{+/0}$ under illumination and in the dark. (b) *J-E* behavior (5 cycles at 30 mV s^{-1}) of the n-Si/Gr and n-Si-H electrodes from (a) in $Fe(CN)_6{}^{3-/4-}{}_{(aq)}$ under illumination. (c) *J-E* behavior (1 cycle) of the n-Si/Gr and n-Si–H electrodes in CH_3CN-$Fc^{+/0}$ in the presence and absence of illumination, after the data collection depicted in (b).

After five potential sweeps in contact with 50 mM $Fe(CN)_6^{3-}$-350 mM $Fe(CN)_6^{4-}$ (aq), the n-Si–H electrode exhibited negliglble photocurrent over the power-producing potential range, consistent with expectations for the formation of an insulating oxide layer under photoanodic conditions.[11] In contrast, the n-Si/Gr photoelectrode exhibited essentially no change in J–E behavior under the same conditions, with V_{oc} = 340 mV and ff = 0.30 (figure 4.1b). As shown in figure 4.1c, after photoelectrochemical operation in contact with $Fe(CN)_6^{3-/4-}{}_{(aq)}$, the J–E behavior of the n-Si/Gr photoanode in contact with the CH_3CN-$Fc^{+/0}$ redox system was almost unchanged from its initial properties in this electrolyte. In fact, a minor improvement in V_{oc} was observed, as well as an apparent decrease in the parallel shunt resistance as indicated by the decreased dependence of the current on applied potential under reverse bias. This is consistent with the passivation of shunts via oxidation in aqueous solution. The chemical nature of these shunts may be due to trace metal impurities from the fabrication procedure or ‘dangling’ Si bonds present due to the formation of a non-stoichiometric silicon oxide.

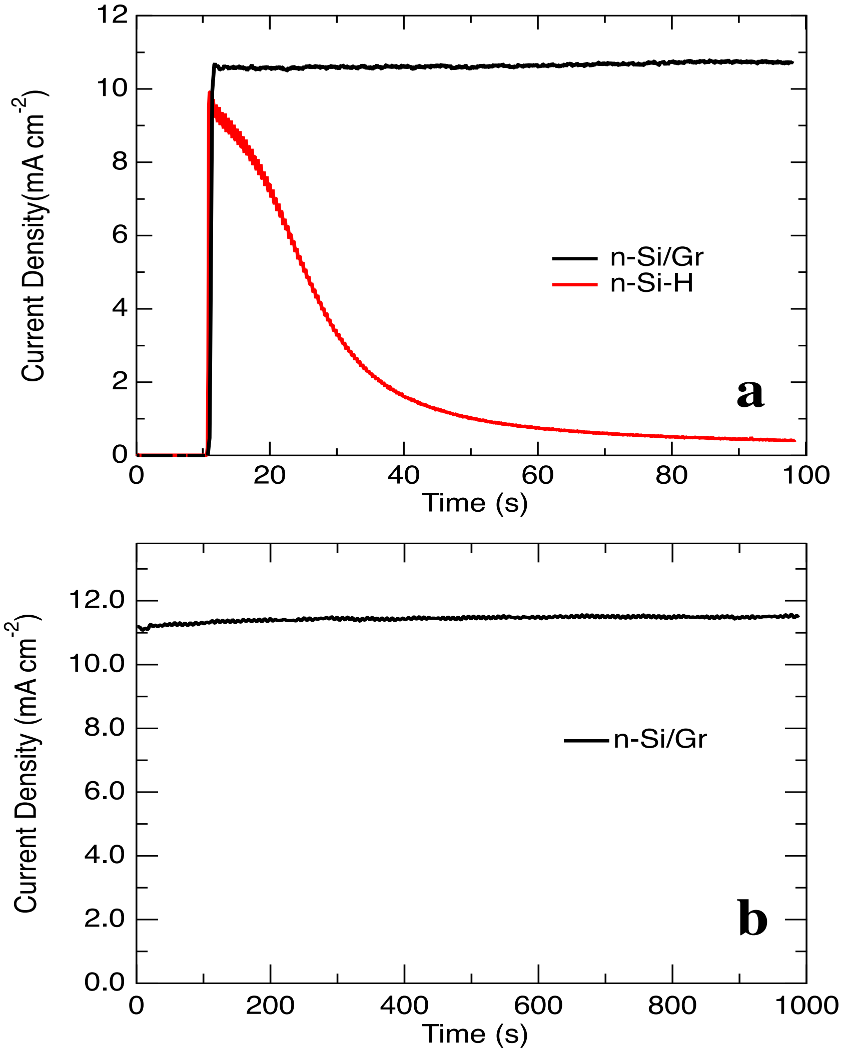

Figure 4.2 (a) Comparison of the *J–t* behavior of potentiostatically controlled n-Si/Gr and n-Si–H electrodes (*E* = 0 V vs. solution) in contact with $Fe(CN)_6{}^{3-/4-}{}_{(aq)}$ under illumination required to produce a short-circuit photocurrent density of ~11 mA cm^{-2} (~33 mW/cm^2). The illumination began at t = 10 s. (b) *J–t* behavior of an n-Si/Gr electrode in $Fe(CN)_6{}^{3-/4-}{}_{(aq)}$ under illumination required to produce a short-circuit photocurrent density of ~11 mA cm^{-2} over 1000 s (E = 0 V vs. solution). The slight increase in current over 1000 s was attributed to instability in the light source.

Figure 4.2 further displays the stability toward photopassivation of the n-Si/Gr surface relative to the n-Si–H surface. Both the n-Si/Gr and the n-Si–H electrodes were immersed in $Fe(CN)_6^{3-/4-}$(aq) and illuminated to produce ~11 mA cm^{-2} of photocurrent at a potential of E=0 V vs. the Nernstian potential of the solution. The n-Si/Gr electrode exhibited stable photocurrents, whereas the n-Si–H electrode decayed back to baseline within ~30 seconds (figure 4.2a). Figure 4.2b extends the experiment on the n-Si/Gr electrodes to 1000 seconds. Additionally, comparison of the stability in $Fe(CN)_6^{3-/4-}$(aq) of an n-Si/Gr electrode to that of methylated n-Si(111) electrodes showed that graphene was significantly more effective at preventing electrochemical performance degradation (See chapter 4 appendix), albeit without the interfacial dipole that increases the V_{oc} of n-type CH_3-Si(111) surfaces relative to H-Si(111) surfaces. Comparison of the n-Si/Gr electrode stability in $Fe(CN)_6^{3-/4-}$(aq) to that of n-Si–H electrode stability under ~100 mW/cm^2 illumination indicated degradation of both electrodes, albeit at much higher rates for the n-Si–H system (See chapter 4 appendix).

4.2.2 Behavior of graphene-covered n-Si photoanodes in non-aqueous electrolyte

Figure 4.3 compares the *J–E* behavior of freshly prepared n-Si/Gr electrodes in contact with CH_3CN-$CoCp_2^{+/0}$ to the *J–E* behavior of n-Si/Gr electrodes in contact with CH_3CN-$Fc^{+/0}$ and CH_3CN-$AcFc^{+/0}$.

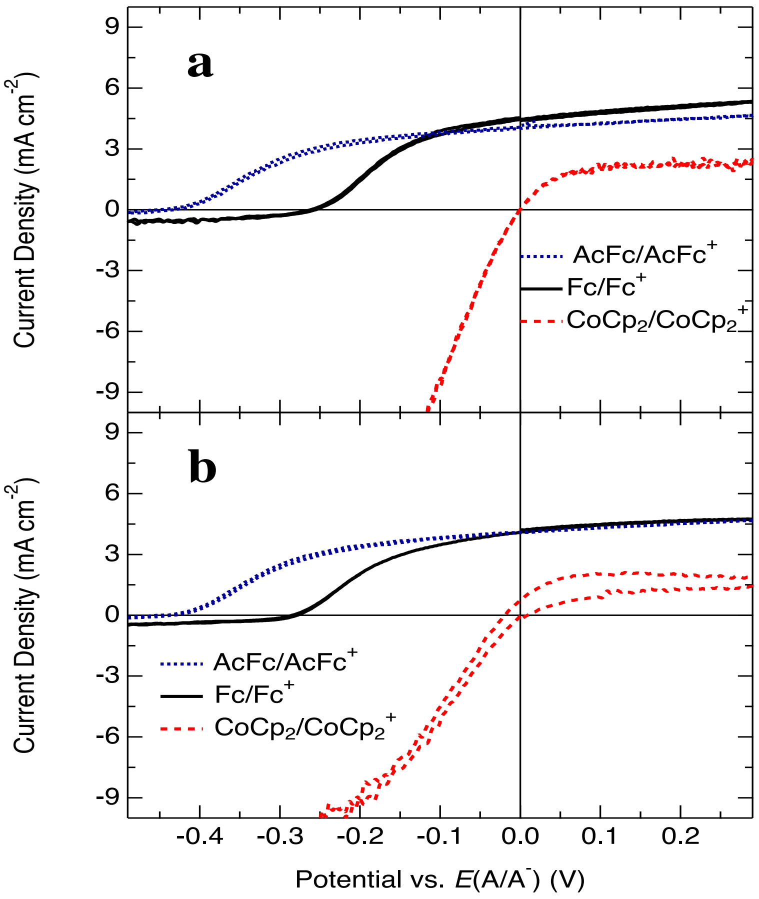

Figure 4.3 (a) *J–E* behavior (forward and reverse scan) of n-Si/Gr electrodes in CH_3CN-$AcFc^{+/0}$ (V_{oc} = 0.43 V), CH_3CN-$Fc^{+/0}$ (V_{oc} = 0.26 V), and CH_3CN-$CoCp_2^{+/0}$ (V_{oc} = 0 V) under illumination prior to exposure to $[Fe(CN)_6]^{3-/4-}{}_{(aq)}$ (b) *J–E* behavior of n-Si/Gr electrodes in CH_3CN-$AcFc^{+/0}$ (V_{oc} = 0.43 V), CH_3CN-$Fc^{+/0}$ (V_{oc} = 0.28 V), and CH_3CN-$CoCp_2^{+/0}$ under illumination after exposure to $[Fe(CN)_6]^{3-/4-}{}_{(aq)}$. The solution potentials were as follows: *E(*$AcFc^{+/0}$) = +0.4 V vs. $Fc^{+/0}$, *E(*$Fc^{+/0}$) = -0.1 V vs. $Fc^{+/0}$, and *E(*$CoCp_2^{+/0}$) = -1.26 V vs. $Fc^{+/0}$.

The moderate V_{oc} observed for n-Si/Gr/CH$_3$CN-Fc$^{+/0}$ contacts, larger V_{oc} observed for n-Si/Gr/CH$_3$CN-AcFc$^{+/0}$ contacts, and negligible V_{oc} in contact with CH$_3$CN-CoCp$_2$$^{+/0}$ is in accord with the expectation of increasing V_{oc} with increasingly oxidizing electrolyte potentials, and is also consistent with the junction energetics being controlled at least in part by the difference in electrochemical potential between the Si and liquid phase. After operation in both electrolytes, the n-Si/Gr electrodes were then operated under photoanodic conditions in contact with Fe(CN)$_6$$^{3-/4-}$$_{(aq)}$, in an analogous fashion to the electrodes shown in figure 4.1b.

The data in figure 4.3b indicate that the electrochemical properties of the electrodes were essentially unaffected by operation in the oxidizing Fe(CN)$_6$$^{3-/4-}$$_{(aq)}$ environment. If pinholes in the graphene had controlled the junction energetics, the Si exposed through these pinholes would presumably have passivated upon treatment in Fe(CN)$_6$$^{3-/4-}$ $_{(aq)}$, leaving only the graphene-covered regions to control the junction energetics. Thus, the measurement of V_{oc} > 200 mV for n-Si/Gr in contact with Fc$^{+/0}$, V_{oc} >400 mV for n-Si/Gr/AcFc$^{+/0}$ contacts, and negligible V_{oc} for n-Si/Gr/CoCp$_2$$^{+/0}$ contacts indicates that the Fermi level of the n-Si/Gr electrodes was not fully pinned by the presence of graphene at the silicon/graphene/electrolyte junction. The V_{oc} for n-Si/Gr electrodes in contact with CH$_3$CN-Fc$^{+/0}$ was consistently smaller than the V_{oc} of n-Si–H in contact with the same electrolyte (c.f. Figure 4.1a). The data in figures 4.1, 4.2, and 4.3 were highly reproducible between electrodes.

This behavior is consistent with expectations that a limited number of electronic states in graphene affect the junction energetics without fully pinning the Fermi level of the semiconductor. Specifically, Poisson's equation was solved while treating the n-

Si/Gr/electrolyte interface as consisting of a depleted semiconductor (Si) of known dielectric and capacitive properties in contact with an atomically thin material with the known density of electronic states as a function of energy of graphene, with this entire phase into contact with a phase consisting of the known dielectric and capacitive properties representative of a typical electrolyte solution. An initial difference in Fermi levels of ~0.8 eV between the semiconductor and the electrolyte should produce a potential drop of ~0.65 V in the Si space-charge region, with the remainder dropping across the solid/liquid interface. Mott-Schottky ($1/C^2$ vs. E) data yielded support for this model, in that a lower barrier height was observed for the n-Si/Gr/ CH_3CN-$Fc^{+/0}$ contacts than for n-Si-H/CH_3CN-$Fc^{+/0}$ contacts (see chapter 4 appendix). This behavior is consistent with a portion of the total potential drop occurring in the graphene and solution layer as opposed to the space-charge region of the semiconductor, and is also consistent with the smaller V_{oc} of n-Si/Gr/CH_3CN-$Fc^{+/0}$ contacts relative to n-Si–H/CH_3CN-$Fc^{+/0}$ contacts. Many factors, including the formation of a thin insulating oxide as well as changes in charge-transfer kinetics can affect the relationship between the barrier height and V_{oc} and could account for the somewhat smaller change in V_{oc} relative to the change in barrier height.

Fitting the forward-bias dark *J–E* behavior of the n-Si/Gr/CH_3CN-$Fc^{+/0}$ contact to the diode equation, $J = J_0*[\exp(-q\Delta V/\eta kT)-1]$ where J_0 is the exchange current density, q is unsigned charge on an electron, k is Boltzmann's constant, T is the absolute temperature, η is the diode quality factor, and ΔV is the difference between the applied potential and the Nernst potential of the solution, yielded $J_0 = 9.61 \times 10^{-7}$ A cm^{-2} ($\pm$ 6.10 $\times 10^{-8}$) and $\eta = 1.65$ ($\pm$ 0.02). Analysis of the dark *J-E* behavior of a freshly HF-etched n-Si–H electrode in contact with CH_3CN-$Fc^{+/0}$ yielded $J_0 = (6.80 \pm 0.51) \times 10^{-8}$ A cm^{-2} and $\eta = 1.25 \pm 0.012$. The $J_{0,\text{n-Si-H}}$ and $J_{0,\text{ n-Si/Gr}}$ values for these contacts were much smaller than the values obtained for Si/Gr/CH_3CN-$CoCp_2^{+/0}$ contacts ($J_0 \sim 10^{-3}$ A cm^{-2}) , and were comparable to J_0 values reported for highly rectifying n-Si/organic conducting polymer contact ($J_0 \sim 2 \times 10^{-8}$ A cm^{-2}). Similar to the reported results for n-Si/polymer contacts, the J_0 values for n-Si/Gr in contact with varying redox species spanned approximately five orders of magnitude, in comparison to n-Si/metal contacts, which are generally limited to a range of three orders of magnitude in J_0. This further supports the conclusion that the Si/Gr/electrolyte interface was only partially pinned by the presence of graphene. [26] The higher than unity ideality factor could result from a number of factors, including the voltage drop across the small amount of interfacial oxide as well as the expected voltage-dependent surface charge density that results from the observations and modeling of the interfacial energetics.

4.3 Conclusion

The ability of graphene to protect metallic electrodes against corrosion is controversial.[14-16,27] Herein we have clearly demonstrated that graphene markedly enhances the stability of silicon towards passivation by oxide formation under illumination, even in the stressing case of anodic operation in contact with aqueous solutions. In addition, we have elucidated the effects of graphene on the interfacial energetics of semiconductor/liquid contacts, which is not accessible on metallic electrodes and thus has not been defined or elucidated previously. The V_{oc} vs. solution potential relationships observed from the *J–E* data demonstrate that Fermi-level pinning by graphene did not fully limit the observed photovoltages. Further study is required to determine whether the photovoltage is maximized for the n-Si/Gr system in contact with CH_3CN-$AcFc^{+/0}$. Extended studies of the stability imparted by graphene to silicon surfaces and the electronic and chemical effects of graphene on the silicon surface are currently underway to elucidate the extent of the graphene-imparted stability especially for bilayer and multi-layer of grapshene coatings, as well as the effect of graphene on the surface chemistry and recombination characteristics of the underlying Si and the effect of graphene on n-Si/oxygen-evolution catalyst systems.

4.4 Acknowledgements

The bulk of the above work appeared in *The Journal of the American Chemical Society* in 2013 (DOI: 10.1021/ja407462g). I am thankful to Matt Bierman, Nick Petrone, Nick Strandwitz, Shane Ardo, Fan Yang, and James Hone for their invaluable contributions to this work.

4.5 References

1. Sze, S. M.; Ng, K., K. *Physics of Semiconductor Devices*; 3rd ed.; John Wiley & Sons, Inc.: Hoboken, NJ, 2007.
2. Menezes, S.; Heller, A.; Miller, B. *Journal of The Electrochemical Society* **1980**, *127*, 1268.
3. Bélanger, D.; Dodelet, J. P.; Lombos, B. A. *Journal of The Electrochemical Society* **1986**, *133*, 1113.
4. Contractor, A. Q.; Bockris, J. O. M. *Electrochimica Acta* **1984**, *29*, 1427.
5. Howe, A. T.; Hawkins, R. T.; Fleisch, T. H. *Journal of The Electrochemical Society* **1986**, *133*, 1369.
6. Fan, F. R. F.; Shea, T. V.; Bard, A. J. *Journal of The Electrochemical Society* **1984**, *131*, 828.
7. Nakato, Y.; Ueda, K.; Yano, H.; Tsubomura, H. *The Journal of Physical Chemistry* **1988**, *92*, 2316.
8. Strandwitz, N. C.; Comstock, D. J.; Grimm, R. L.; Nichols-Nielander, A. C.; Elam, J.; Lewis, N. S. *J Phys Chem C* **2013**, *117*, 4931.
9. Fonash, S. J. *Solar Cell Device Physics*; 2nd ed.; Elsevier Inc.: Amsterdamn, 2010.
10. Chen, Y. W.; Prange, J. D.; Dühnen, S.; Park, Y.; Gunji, M.; Chidsey, C. E. D.; McIntyre, P. C. *Nat Mater* **2011**, *10*, 539.
11. Bansal, A.; Lewis, N. S. *The Journal of Physical Chemistry B* **1998**, *102*, 4058.
12. Bansal, A.; Lewis, N. S. *The Journal of Physical Chemistry B* **1998**, *102*, 1067.

13. Bolts, J. M.; Bocarsly, A. B.; Palazzotto, M. C.; Walton, E. G.; Lewis, N. S.; Wrighton, M. S. *Journal of the American Chemical Society* **1979**, *101*, 1378.

14. Chen, S.; Brown, L.; Levendorf, M.; Cai, W.; Ju, S.-Y.; Edgeworth, J.; Li, X.; Magnuson, C. W.; Velamakanni, A.; Piner, R. D.; Kang, J.; Park, J.; Ruoff, R. S. *ACS Nano* **2011**, *5*, 1321.

15. Prasai, D.; Tuberquia, J. C.; Harl, R. R.; Jennings, G. K.; Bolotin, K. I. *ACS Nano* **2012**, *6*, 1102.

16. Sutter, E.; Albrecht, P.; Camino, F. E.; Sutter, P. *Carbon* **2010**, *48*, 4414.

17. Lee, Y.; Bae, S.; Jang, H.; Jang, S.; Zhu, S.-E.; Sim, S. H.; Song, Y. I.; Hong, B. H.; Ahn, J.-H. *Nano Letters* **2010**, *10*, 490.

18. Suk, J. W.; Kitt, A.; Magnuson, C. W.; Hao, Y.; Ahmed, S.; An, J.; Swan, A. K.; Goldberg, B. B.; Ruoff, R. S. *ACS Nano* **2011**, *5*, 6916.

19. Flynn, G. W. *The Journal of Chemical Physics* **2011**, *135*, 050901.

20. Mak, K. F.; Sfeir, M. Y.; Wu, Y.; Lui, C. H.; Misewich, J. A.; Heinz, T. F. *Physical Review Letters* **2008**, *101*, 196405.

21. Li, X.; Zhu, H.; Wang, K.; Cao, A.; Wei, J.; Li, C.; Jia, Y.; Li, Z.; Li, X.; Wu, D. *Advanced Materials* **2010**, *22*, 2743.

22. Chen, C.-C.; Aykol, M.; Chang, C.-C.; Levi, A. F. J.; Cronin, S. B. *Nano Letters* **2011**, *11*, 1863.

23. Morozov, S. V.; Novoselov, K. S.; Katsnelson, M. I.; Schedin, F.; Elias, D. C.; Jaszczak, J. A.; Geim, A. K. *Physical Review Letters* **2008**, *100*, 016602.

24. Droscher, S.; Roulleau, P.; Molitor, F.; Studerus, P.; Stampfer, C.; Ensslin, K.; Ihn, T. *Applied Physics Letters* **2010**, *96*, 152104.

25. Ponomarenko, L. A.; Yang, R.; Gorbachev, R. V.; Blake, P.; Mayorov, A. S.; Novoselov, K. S.; Katsnelson, M. I.; Geim, A. K. *Physical Review Letters* **2010**, *105*, 136801.

26. Sailor, M. J.; Klavetter, F. L.; Grubbs, R. H.; Lewis, N. S. *Nature* **1990**, *346*, 155.

27. Schriver, M.; Regan, W.; Gannett, W. J.; Zaniewski, A. M.; Crommie, M. F.; Zettl, A. *ACS Nano* **2013**.

4.6 Appendix

4.6.1 Methods

4.6.1.1 Chemicals/Materials

All experiments employed single-crystalline, Czochralski grown, (111)-oriented, planar, 380 μm thick, phosphorus doped, 1.1 Ω-cm resistivity (doping density, $N_D \approx 5x10^{15}$ cm^{-3}) n-type silicon (University Wafer).

Water was obtained from a Barnstead Nanopure system and had a resistivity ≥ 18.0 MΩ-cm. Copper Etch Type CE – 100 ($FeCl_3$-based, Transene Company, Inc., Danvers, MA), Copper Etch Type APS – 100 (Ammonium persulfate-based, Transene), buffered $HF_{(aq)}$ (semiconductor grade, Transene Company, Inc., Danvers, MA), and 11 M NH_4F (semiconductor grade, Transene) were used as received. Acetone (HPLC grade, Sigma-Aldrich) was used as received. Acetonitrile (99.8% anhydrous, Sigma-Aldrich) that was used in electrochemical measurements was dried over Al_2O_3 prior to use.

Ferrocene (Fc, bis(cyclopentadienyl)iron(II) ,99%,Strem), cobaltocene ($CoCp_2$, bis(cyclopentadienyl)cobalt(II), 98%, Strem), and acetylferrocene (AcFc, (acetylcyclopentadienyl)-cyclopentadienyl iron(II), 99.5%, Strem) were purified via sublimation. Ferrocenium tetraflouroborate ($Fc^+[BF_4]^-$, bis(cyclopentadienyl)iron(III) tetraflouroborate,technical grade,Sigma-Aldrich) was recrystallized from a mixture of diethyl ether (ACS grade, EMD) and acetonitrile (ACS grade, EMD) and dried under vacuum. Cobaltocenium hexafluorophosphate ($CoCp_2^+$, bis(cyclopentadienyl)cobalt(III) hexafluorophosphate, 98%, Sigma-Aldrich) was recrystallized from a mixture of ethanol

(ACS grade, EMD) and acetonitrile (ACS grade, EMD) and dried under vacuum. Acetylferrocenium ($AcFc^+$) was generated in situ via electrochemical oxidation of AcFc with the concomitant reduction reaction occurring in a compartment separated from the electrochemical cell using a Vycor frit.

Potassium ferricyanide ($K_3[Fe(CN)_6]$, 99.2%, Sigma-Aldrich) and potassium ferrocyanide ($K_4[Fe(CN)_6]\cdot 3H_2O$, ACS Certified, Fischer Scientific) were used as received. $LiClO_4$ (battery grade, Sigma-Aldrich) was used as received. Petri dishes used were Falcon Optilux™ branded and were cleaned with water prior to use. All chemicals were used as received unless otherwise noted.

4.6.1.2 Electrode Fabrication

A monolayer film of graphene was formed via chemical-vapor deposition (CVD) of carbon onto a Cu foil. A 25 µm-thick Cu foil (99.999%, Alfa Aesar) was heated in a tube furnace to 800 °C at a pressure of 50 mTorr and annealed for 10 h under a 2 sccm flow of $H_{2(g)}$. Graphene was subsequently synthesized on the surface of the copper foil by flowing $CH_{4(g)}$ (35 sccm) and $H_{2(g)}$ (2 sccm) at 1000 °C and 250 mTorr. This method of graphene growth has been shown to grow polycrystalline monolayer graphene and figure 4A.1 shows a representative Raman spectrum of the starting material graphene on 300 nm SiO_2.[1] After growth of the graphene, the gas flow rates and chamber pressure were maintained and the Cu foil was rapidly cooled to room temperature by removing the furnace from the growth section of the process tube. The graphene synthesis resulted in grains that were 0.2 to 5 µm on a side, and an analysis of the grain size and grain distribution of the resulting polycrystalline graphene film has been presented in Petrone, et al., 2008.[1] The surface was then covered with a coating of 495K A4 polymethyl methacrylate (PMMA, MicroChem) by spinning at 2000 RPM (500 RPM/s acceleration) for 60 s, followed by a 10-min bake at 185 ^{o}C. This procedure was repeated for a total of two PMMA applications. The Cu was etched away using either a 15% (v:v) $NH_4(S_2O_8)_2$ (aq) solution or a 40% $FeCl_3$/1% HCl (aq) solution (Transene).[2] Cu removal was determined visually and confirmed by XPS analysis (figure 4A.6). To remove etchant residue, the resultant PMMA/graphene stack was transferred consecutively to three fresh baths of 18 MΩ-cm resistivity H_2O in petri dishes. The transfer was executed using a freshly piranha-cleaned (7:3 H_2SO_4:H_2O_2, aqueous solution) SiO_2-coated Si wafer to collect the PMMA/Gr stack from one bath and release the stack in a fresh H_2O bath. N-type Si samples were washed consecutively with H_2O, methanol, acetone, methanol, and H_2O, and were then submerged in a piranha solution for 10 min and etched for 30 s in buffered $HF_{(aq)}$ (Buffer HF Improved, semiconductor grade, Transene). The cleaned PMMA/graphene stack was transferred from a water bath to the cleaned, freshly $HF_{(aq)}$ etched Si(111) surface, and a gentle stream of $N_{2(g)}$ was used to remove H_2O from the intervening space between the graphene and the Si. The PMMA/graphene/Si stack was then heated at 80 °C for 10 min in air, followed by submersion for 10 min in acetone to remove the PMMA layer. The resulting Si/graphene (Si/Gr) stack was annealed for ~8 h at 300 °C under forming gas (95:5 v:v N_2:H_2) to further remove PMMA residue from the surface of the graphene.[1] Si/Gr electrodes ~ 0.02 cm^2 in area were then fabricated with the use of GaIn (75:25 mass:mass) eutectic as a back ohmic contact. The electrodes were affixed to a Cu wire with Ag paint, and all surfaces, except the electrode, were insulated from the electrolyte by use of Loctite Hysol 9460 epoxy. On average, out of ten fabricated electrodes, two to three showed very low shunt resistances in non-aqueous electrolytes and/or displayed minimal protection of the Si surface from oxidation. The remaining 7-8 electrodes gave data consistent with that shown figures 4.1, 4.2, and 4.3. An analogous process was used to fabricate electrodes that were not coated with graphene (n-Si–H and n-Si–Me electrodes). Methylated silicon wafers were prepared using a previously reported procedure.[3] Before use, the graphene-free, non-methylated Si electrodes were terminated with Si-H bonds by exposure to buffered $HF_{(aq)}$ for 30 seconds. Electrodes were also fabricated by exposing silicon wafers to the same conditions as the graphene-transfer procedure, except that no graphene was present between the PMMA and Cu. Such electrodes were not HF-etched prior to use.

4.6.1.3 Instrumentation

X-ray photo- electron spectroscopy (XPS) data was collected at ~5 × 10^{-9} Torr using a Kratos AXIS Ultra DLD with a magnetic immersion lens that consisted of a spherical mirror and concentric hemispherical analyzers with a delay-line detector (DLD). An Al Kα (1.486 KeV) monochromatic source was used for X-ray excitation. Ejected electrons were collected at an angle of 90° from the horizontal. The CASA XPS software package v 2.3.16 was used to analyze the collected data.

Electrochemical data were obtained using a Princeton Applied Research Model 2273 or a Gamry Reference 600 potentiostat. A Pt wire reference electrode (0.5 mm dia., 99.99% trace metals basis, Sigma-Aldrich) and a Pt mesh counter electrode (100 mesh, 99.9% trace metals basis, Sigma-Aldrich) were used for the electrochemical measurements. The cell potentials for the non-aqueous redox species were determined using cyclic voltammetry to compare the solution potential to the formal potential of the redox species. The potential difference between cells was calculated using the difference between the formal potentials for each redox couple using standard potentials from the literature.[4] The CH_3CN-$CoCp_2^{+/0}$ solution ($CoCp_2$ [3 mM]/ $CoCp_2^+$ [50 mM]) was calculated to have a solution potential of -1.4 V vs Fc/Fc$^+$, the CH_3CN-$Fc^{+/0}$ solution (Fc [55 mM]/ Fc$^+$ [3 mM]) was calculated to have a solution potential of -0.10 V vs Fc/Fc$^+$, and the CH_3CN-$AcFc^{+/0}$ solution (pre-electrolysis AcFc concentration = [50 mM]) was calculated to have a solution potential of +0.40 V vs Fc/Fc$^+$. The non-aqueous electrochemical solutions each contained 1.0 M $LiClO_4$. The aqueous $K_3[Fe(CN)_6]/K_4[Fe(CN)_6]$ ($[Fe(CN)_6]^{-3}$, 50mM; $[Fe(CN)_6]^{-4}$, 350mM) solution contained no additional supporting electrolyte due to the high intrinsic salt concentration. The current under forward bias saturated at much larger values in the $Fe(CN)_6^{3-/4-}$ solution relative to in the Fc$^+$/Fc solution because of the increased concentration of electron-accepting species in the $Fe(CN)_6^{3-/4-}$ solution. CH_3CN-$Fc[BF_4]$ is a highly colored species that at high concentrations absorbs a significant fraction of the light prior to photons striking the photoelectrode. The electrolyte solution was rapidly stirred with a small, Teflon-covered stir bar. Illumination was provided with an ELH-type tungsten-halogen lamp. Illumination intensities were set to provide either 3-5 mA cm^{-2} or ~10-11 mA cm^{-2}. These values corresponded to ~1/10th and ~1/3rd of a Sun (~10 mW cm^{-2} and ~33 mW cm^{-2}), respectively, as determined through the concurrent use of a Si photodiode (Thor Laboratories) that was calibrated relative to a secondary standard photodetector that was NIST-traceable and calibrated at 100 mW cm^{-2} of AM1.5 illumination. Non-aqueous electrochemistry was performed anaerobically in an $Ar_{(g)}$-filled glovebox. Aqueous electrochemistry was performed in air. Electrodes were washed with H_2O and isopropanol and dried prior transfer between electrolyte solutions.

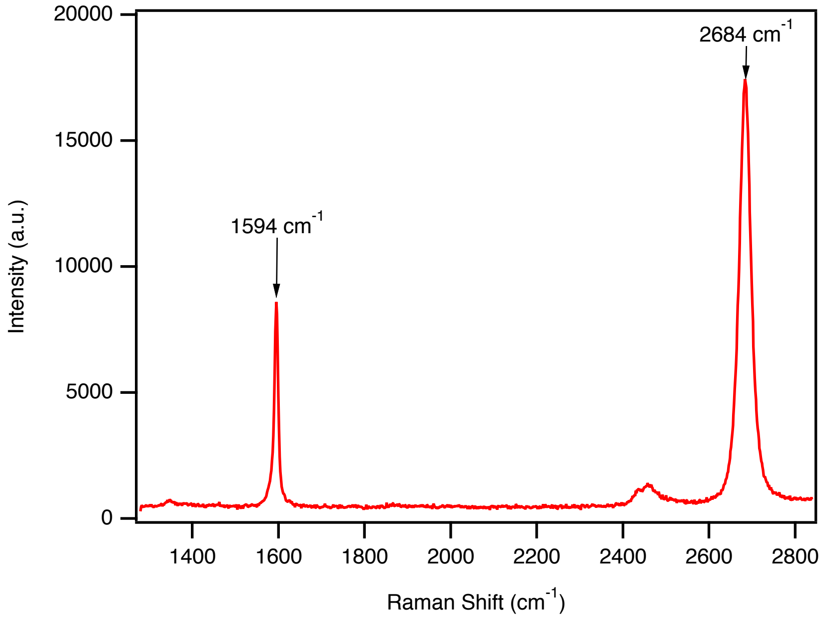

Figure 4A.1. Representative Raman spectrum of starting material graphene on 300 nm SiO_2 (λ=532 nm). Sharp G (1594 cm^{-1}, FWHM: 10 cm^{-1}) and 2D (2684 $cm^{-1,}$ FWHM: 32 cm^{-1}), as well as a small defect peak (~1350 cm^{-1}) confirm the monolayer, defect-free nature of the starting material.[5,6]

4.6.2 Mott-Schottky Fitting Procedure

To perform the Mott-Schottky analysis, a 10 mV sinusoidal AC signal was superimposed over DC biases of 0.25, 0.30, 0.35, 0.4, 0.45, 0.50, 0.55, and 0.60 V versus the Nernstian potential of the solution. The frequency of the AC signal was varied from 50 to 300 kHz at each DC bias. The impedance data were modeled by the equivalent Randle's circuit shown in figure 4A.2, and best fits were obtained using the fitting procedure executed by the ZView electrochemical software (Scribner Associates, Inc.). The data in table 4A.1 and table 4A.2 were used to approximate the area-normalized series resistance imparted to the n-Si/Gr electrodes by the fabrication procedure at approximately 9 Ω cm^2 by comparing the average area-normalized resistance of the n-Si/Gr and n-Si–H electrodes (24.4 Ω cm^2 and 15.1 Ω cm^2, respectively. The *J-E* data of n-Si/Gr under illumination in contact with CH_3CN-$Fc^{0/+}$ electrolyte indicated a series resistance of 23.1 ± 5.1 Ω cm^2 (6 electrodes), in excellent accord with data found via electrochemical impedance spectroscopy.

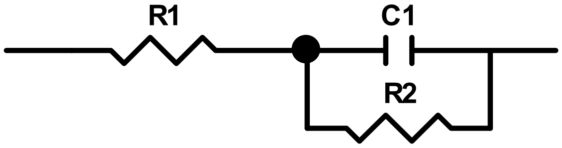

Figure 4A.2. Equivalent circuit used to analyze the impedance data. C1 was treated as the space-charge capacitance (C_{sc}).

Voltage (V)	R1(Ω cm^2)	R2(Ω cm^2)	C1 (μF cm^2)
0.25	25.6	7656.2	2.89E-02
0.3	24.7	7685.7	2.73E-02
0.35	23.9	7641.1	2.62E-02
0.4	24.3	7642.4	2.53E-02
0.45	24.4	7577.3	2.47E-02
0.5	24.2	7615.4	2.39E-02
0.55	24.2	7661.3	2.33E-02
0.6	24.1	7688.3	2.27E-02

Table 4A.1. Results obtained from the fitting of the impedance data at each applied voltage for the representative n-Si/Gr electrode.

Voltage (V)	R1(Ω cm^2)	R2(Ω cm^2)	C1 (μF cm^2)
0.25	12.9	154180.5	4.07E-03
0.3	13.7	95594.4	3.99E-03
0.35	14.2	84057.0	3.91E-03
0.4	15.0	60479.1	3.83E-03
0.45	15.5	49401.7	3.74E-03
0.5	16.1	47259.1	3.67E-03
0.55	16.7	49229.5	3.60E-03
0.6	17.4	41858.1	3.54E-03

Table 4A.2. Results obtained from the fitting of the impedance data at each applied voltage for the representative n-Si–H electrode.

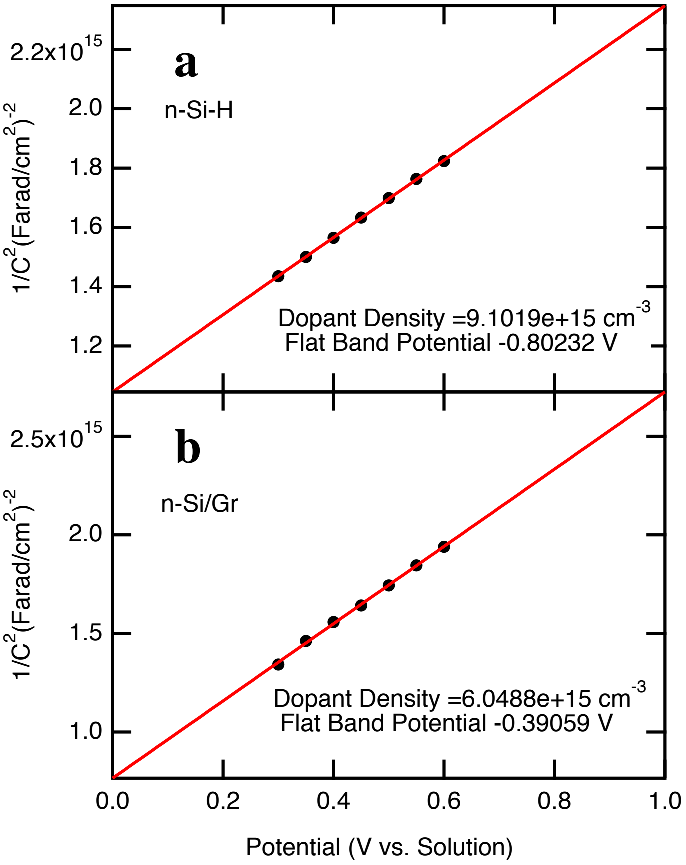

Figure 4A.3-I. Mott-Schottky (C_{diff}^{-2} vs E) behavior of (a) n-Si–H and (b) n-Si/Gr electrodes in contact with CH_3CN-$Fc^{+/0}$ in the dark. The differential capacitance (C_{diff}) at each voltage was determined by fitting the impedance vs. frequency data between 50 kHz and 300 kHz to an equivalent Randle's circuit at each voltage. The doping density measured by 4-point probe technique was calculated to be N_D~5x10^{15} cm^{-3}.

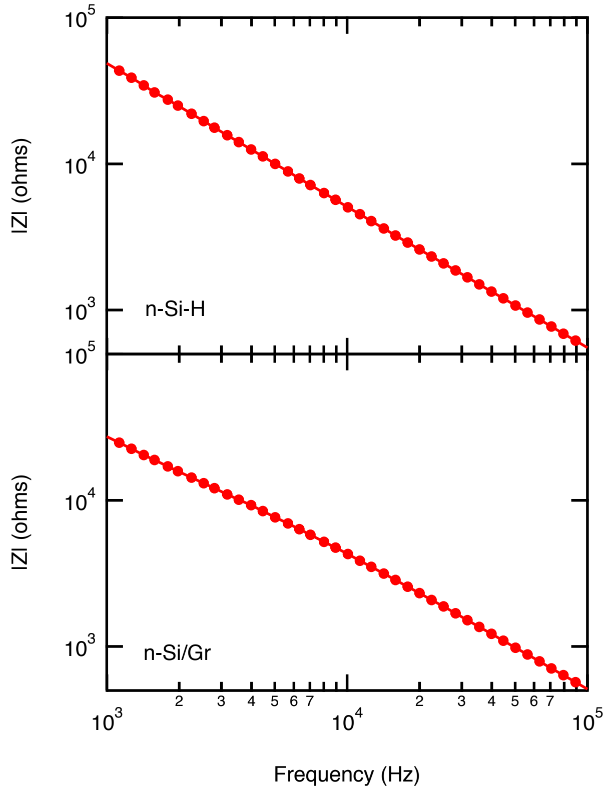

Figure 4A.3-II Bode plot of n-Si–H and n-Si/Gr electrodes in contact with CH_3CN-$Fc^{+/0}$ in the absence of illumination at *E* = 0.40 V vs. the Nernst potential of the solution. The deviation from linearity that can be seen in this figure suggests that the Randles circuit is an incomplete description of the graphene-covered Si photoelectrode interface.

4.6.3 Description of Semiconductor/Gr/Electrolyte Model

To gain a better understanding of the electrochemical and photoelectrochemical effects of graphene, the equilibration of the three-phase semiconductor/graphene/electrolyte system was analyzed. The following assumptions were made:

- The Fermi level of all three phases is the same at equilibrium.
- Equilibrium is obtained through charge transfer between the three phases.
- The initial Fermi level of the semiconductor ($E_{F,SC}$) is closer to the vacuum level than the initial Fermi level of graphene ($E_{F,Gr}$), which is in turn closer to the vacuum level than the initial Fermi level of the electrolyte ($E_{F,electrolyte}$) .
- The sum of the net charge in the three phases is zero, as required by electroneutrality: $Q_{sc} + Q_{Gr} + Q_{liquid} = 0$, where Q_{sc} is the net charge in the semiconductor, Q_{Gr} is the net charge in the graphene, and $Q_{electrolyte}$ is the net charge in the liquid electrolyte.
- The potential drop in the semiconductor (V_{bi}) is well-modeled by the potential drop of a semiconductor under depletion conditions.
- The potential drop in the electrolyte (V_H) is well-modeled using the known capacitive and dielectric properties of a typical electrolyte solution.
- The Fermi level of the graphene phase may be strongly shifted by the addition or loss of electrons, due to the low density of states and atomically thin structure of the grapheme. This shift (V_{Gr}) can be predicted

using the theoretically calculated DOS of graphene.[7] V_{Gr} is a shift in the graphene Fermi level and not an electrostatic potential drop.

- The potential drop in the interfacial layer between the semiconductor and graphene, as well as the potential drop the interfacial layer between graphene and the liquid electrolyte contact, is negligible.

Essentially, Poisson's equation was solved while treating the n-Si/Gr/electrolyte interface as consisting of a depleted semiconductor (Si) of known dielectric and capacitive properties in contact with an atomically thin material with the known density of electronic states as a function of energy of graphene, with this entire phase in contact with a phase consisting of the known dielectric and capacitive properties representative of a typical electrolyte solution. This treatment parallels, and is consistent with, the interfacial charge equilibration and surface state models that have been developed previously for semiconductor surfaces and are extensively described in the literature.[8,9] To calculate the equilibrium values of Q_{sc}, Q_{Gr}, and $Q_{\mathrm{electrolyte}}$, as well as V_{bi} and V_{H}, the analysis was broken down into two steps and iterated. First, the equilibrium values for the two-phase Gr/electrolyte system were determined using Poisson's equation. Then, using these values as the starting condition, the final self-consistent state for the two-phase Si/Gr system was solved using Poisson's equation. These values were then used as starting conditions for the first two-phase Gr/electrolyte system, and the process was iterated until the values converged to a global minimum. Poisson's equation was solved using a method previously described for equilibration of a two-phase system.[8]

The constants used in the modeling were as follows. The electron affinity of Si was taken to be -4.05 eV vs. vacuum.[10] The Fermi level of phosphorous-doped Si (N_D= 10^{15} cm^{-3}) was calculated to be ~ -4.3 eV. The intrinsic Fermi level of graphene was taken to be -4.6 eV vs. vacuum.[11] The empirical built-in potential difference in the absence of graphene (V_{bi} = 0.8 V) was used to calculate the Fermi level of the liquid electrolyte contacting phase, qE(A/A$^-$) = -5.1 eV versus vacuum (Figure 4A.3-I). The DOS of graphene is known,[7] and from this, [d(DOS)/dE$_{F, Gr}$] was taken to be 1.5x10^{-5} C/eV. The thickness of the Helmholtz layer was set to 5x10^{-8} cm and κ_l was set to 4.0.[12,13]

The potential distribution in the two-phase Gr/electrolyte system was modeled by the following equations:

$$\phi_{Gr} - \phi_{Electrolyte} = V_{Gr} + V_H \tag{1}$$

where ϕ_{Gr} is the Fermi level of the graphene with respect to vacuum, $\phi_{electrolyte}$ is the Fermi level of the liquid electrolyte with respect to vacuum,

$$V_{Gr} = \pm\sqrt{\frac{|Q_{Gr}+\Delta Q|}{0.5*\frac{dDOS}{dE_{F,Gr}}}} \tag{2}$$

and

$$V_H = \frac{D*|Q_{Electrolyte}+\Delta Q|}{\varepsilon_0*\kappa_l} \tag{3}$$

where $Q_{\mathrm{Gr}} = Q_{\mathrm{electrolyte}} = 0$, ΔQ is the change in charge required to reach equilibrium, $[d(\mathrm{DOS}_{\mathrm{Gr}})/dE_{\mathrm{F,\,Gr}}]$ is determined from the reported DOS of graphene with respect to $E_{\mathrm{F,\,Gr}}$, D is the thickness of the Helmholtz layer, ε_o is the permittivity of free space, and κ_l is the relative permittivity of the liquid phase.[7] The solution to this system of equations results in two values for ΔQ because of its quadratic dependence; however, only one of the results is physical. The equilibrium charge distributions for the two-phase Gr/liquid system are $Q_{\mathrm{Gr,\ eq\text{-}a}} = \Delta Q$ and $Q_{\mathrm{electrolyte,\ eq}} = -\Delta Q$. The energy of the Fermi levels at equilibrium implies that the graphene is positively charged and the liquid phase is negatively charged.

To determine the charge distribution for the three-phase Si/Gr/electrolyte system, the two-phase Si/Gr system was modeled by the following equation:

$$\phi_{sc} - \phi_{Gr} = V_{bi} - V_{Gr} \tag{4}$$

where

$$V_{bi} = \frac{(Q_{sc} + \Delta Q)^2}{2qN_D\varepsilon_0\kappa_{sc}} \tag{5}$$

and

$$V_{Gr} = \pm\sqrt{\frac{|Q_{Gr} - \Delta Q|}{0.5 * \frac{dDOS}{dE_{F,Gr}}}} \tag{6}$$

where $Q_{\mathrm{sc}} = 0$, $Q_{\mathrm{Gr}} = Q_{\mathrm{Gr,\ eq\text{-}a}}$ from above, ΔQ is the change in charge required to reach equilibrium, q is the elementary charge, N_{D} is the dopant density, ε_{o} is the permittivity of free space, and κ_{sc} is the relative permittivity of the semiconductor phase.[8] The sign convention on ΔQ was chosen to reflect the decrease in positive charge on the graphene phase and the increase in positive charge on the semiconductor. The graphene phase "loses" charge because it was previously positively charged from equilibration with the liquid phase, and the relative Fermi levels of the semiconductor and graphene phases dictate that the semiconductor transfers negative charge to the graphene. The solution to this system of equations results in four values for ΔQ because of its quartic dependence; however, only one of the results is physical. The equilibrium charge distributions for the two-phase Si/Gr system are $Q_{\mathrm{sc,\ eq}} = \Delta Q$ and $Q_{\mathrm{Gr,\ eq\text{-}b}} = (Q_{\mathrm{Gr,\ eq\text{-}a}} - \Delta Q)$. The energy of the Fermi levels at equilibrium implies that the semiconductor is positively charged and that the graphene remains positively charged.

Equilibration of the two-phase Si/Gr system resulted in non-equilibrium conditions for the two-phase Gr/liquid system as the graphene charge density, and thus potential drop, changed. Thus, the first set of equations was re-solved with the initial conditions, $Q_{\mathrm{Gr}} = Q_{\mathrm{Gr,\ eq\text{-}b}}$ and $Q_{\mathrm{electrolyte}} = Q_{\mathrm{electrolyte,\ eq}}$. The solutions were then used as initial conditions in the second set of equations as $Q_{\mathrm{sc}} = Q_{\mathrm{sc}}$, eq and $Q_{\mathrm{Gr}} = Q_{\mathrm{Gr,\ eq\text{-}a}}$, re-solved, and the process was iterated until $|Q_{\mathrm{Gr,\ eq\text{-}a}} - Q_{\mathrm{Gr,\ eq\text{-}b}}| < Q_{\mathrm{Gr,\ eq\text{-}a}} \times 10^{-5}$. The converged values of the charges were determined to be $Q_{\mathrm{sc,\ eq}} = (+)\ 2.30 \times 10^{-8}$ C, $Q_{\mathrm{Gr,\ eq\text{-}a}} = Q_{\mathrm{Gr,\ eq\text{-}b}} = (+)\ 9.67 \times 10^{-7}$ C, and $Q_{\mathrm{electrolyte,\ eq}} = (-)\ 9.97 \times 10^{-7}$ C. These were used to calculate the potential drops: $V_{\mathrm{bi}} \approx 0.65$ V, $V_{\mathrm{Gr}} \approx 0.35$ and $V_{\mathrm{H}} \approx 0.15$ V. For comparison, for the two-phase Si/liquid electrolyte system $Q_{\mathrm{sc,\ eq}} = (+)\ 1.64 \times 10^{-8}$ C, $Q_{\mathrm{electrolyte,\ eq}} = (-)$

1.64×10^{-8} C, $V_{\mathrm{bi}} = 0.797$ V, and $V_{\mathrm{H}} = 0.0030$ V. These trends are consistent with the experimentally observed V_{oc} values (Figure 4.1).

4.6.4 XPS Analysis

XPS analysis was performed in order to determine the effect of graphene-covering procedure on the n-Si surface. No silicon oxide was detected on freshly HF-etched silicon surfaces (Figure 4A.4). Silicon oxide was detected on the graphene-covered sample (Figure 4A.5) and quantified using a simple substrate—overlayer model described by equation 7[14]:

$$d = \lambda_{ov} \sin\theta \left\{ \ln\left[1 + \frac{I_{Si}^{o}}{I_{ov}^{o}} * \frac{I_{ov}}{I_{Si}}\right]\right\} \tag{7}$$

where d is the overlayer thickness, λ_{ov} is the attenuation factor through the oxide overlayer (assumed to be 2.6 nm)[15], θ the angle from the surface of the sample to the detector (90°), $\frac{I_{Si}^{o}}{I_{ov}^{o}}$ is an instrument normalization factor related to the expected signal for a pure Si and a pure SiO_2 sample (taken to be 1.3 for this instrument), I_{ov} is the measured intensity of the silicon, and I_{ov} is the measured intensity of the silicon oxide overlayer. The thickness of a monolayer of oxide was taken to be 0.35 nm.[16] Using the data in figure 4A.5, equation 7 indicates that the oxide thickness was approximately 0.41 nm, or 1-2 monolayers of oxide.

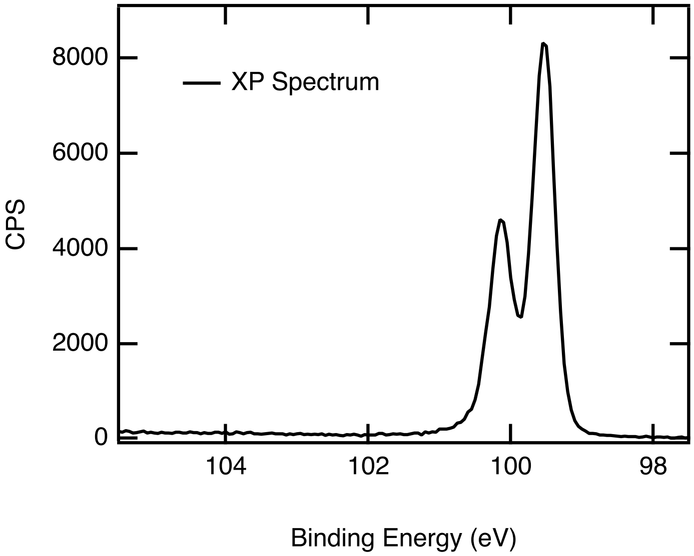

Figure 4A.4. Representative high resolution XP spectrum of the Si 2p region of a silicon wafer that had been etched in HF_{aq} just prior to XPS analysis. The lack of a peak in the 102-104 eV region indicates that there was not silicon oxide present at the Si surface prior to covering the wafer with graphene.

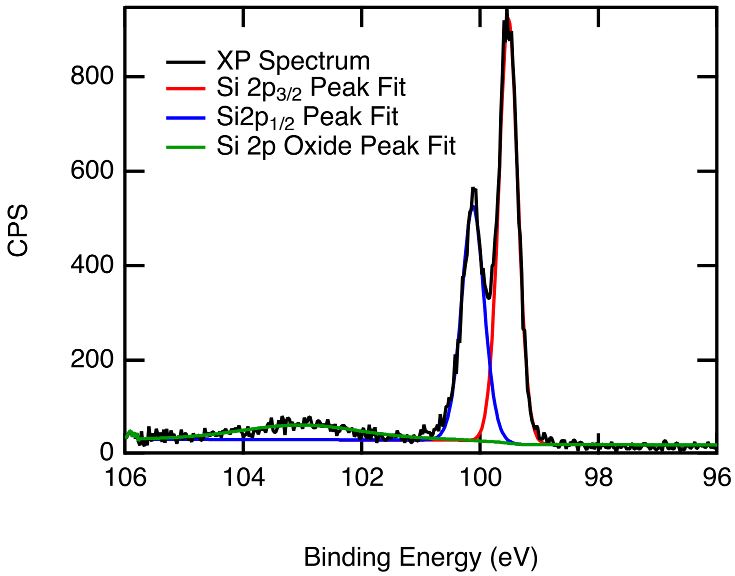

Figure 4A.5. Representative high resolution XP spectrum of the Si 2p region of a silicon wafer covered by graphene. Peak fitting gave peak areas of 80, 239, and 369 for the SiOx, Si 2p½ , and Si 2p3/2 peaks, respectively.

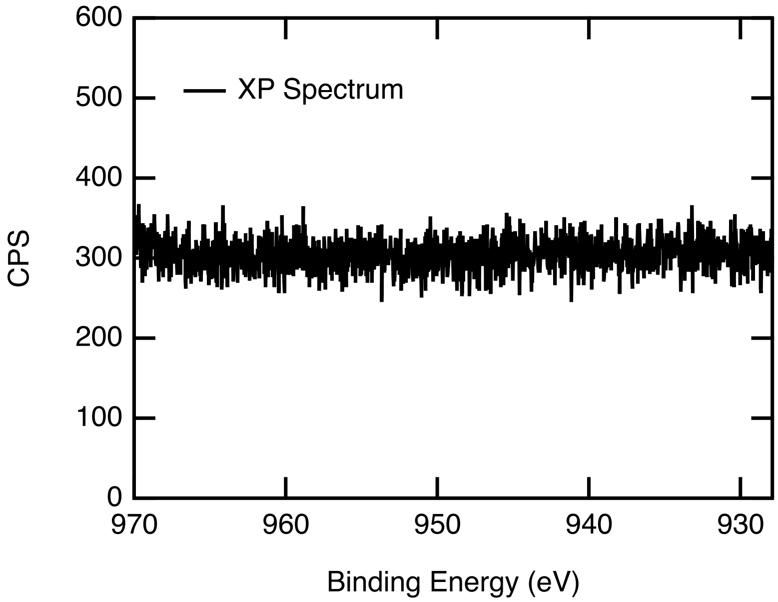

Figure 4A.6. Representative high resolution XP spectrum of the copper region of a silicon wafer covered by graphene. Spectrum indicated copper impurities below the detection limit of the XPS instrument used.

4.6.5 Methylated n-Si stability versus graphene-covered n-Si stability

It is interesting to compare the electrochemical stability imparted by the presence of a graphene layer to the stability imparted by methyl-termination of the silicon surface since both entail a single layer of carbon atoms covering a silicon lattice. As seen in figure 4A.7, at lower light intensities, the n-Si-Me electrode performance is comparable to that of the n-Si/Gr electrode performance. However, as seen in figure 4A.8, at higher light intensities, the n-Si/Gr electrode yielded more stable performance than the n-Si-Me electrode. Future studies will evaluate the stability when these protection techniques are used in tandem.

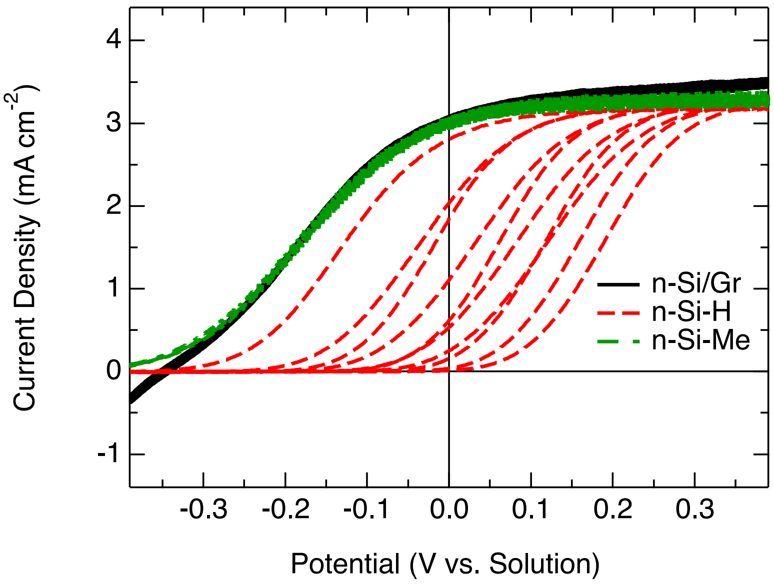

Figure 4A.7. *J-E* behavior (5 cycles at 30 mV s^{-1}) of the n-Si/Gr, n-Si-Me and n-Si-H electrodes $Fe(CN)_6^{3-/4-}{}_{(aq)}$ under ELH lamp illumination necessary to give ~3 mA cm^{-2} light-limited current density.

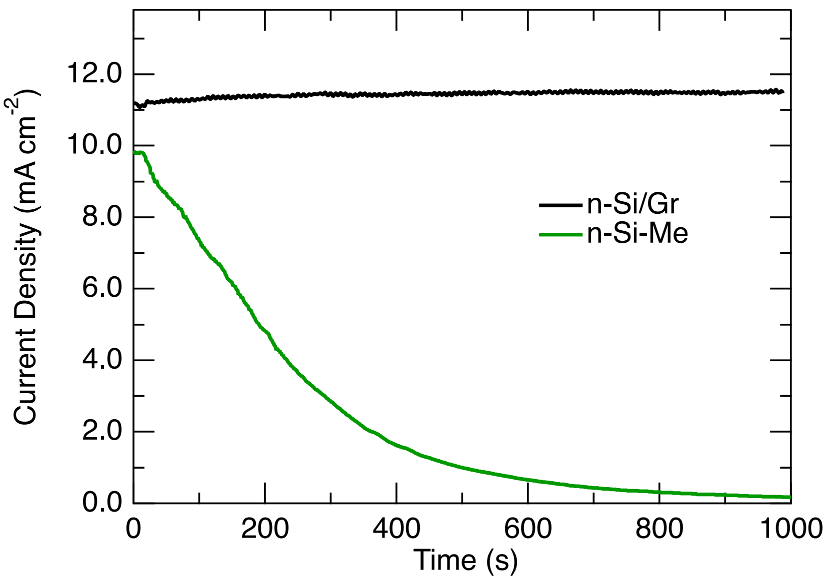

Figure 4A.8. *J–t* behavior of an n-Si/Gr and a n-Si-Me electrode in $Fe(CN)_6^{3-/4-}{}_{(aq)}$ under illumination required to produce a short-circuit photocurrent density of 10-11 mA cm^{-2} over 1000 s (E = 0 V vs. solution).

4.6.6 PMMA/Cu Control electrodes

Bare n-Si electrodes were fabricated analogously to graphene-covered electrodes except that PMMA/Cu stacks were used instead of PMMA/Gr/Cu stacks. As shown in figure 4A.9, such PMMA/Cu coated Si electrodes were unstable under our test conditions and exhibited rapid photopassivation due to oxide formation.

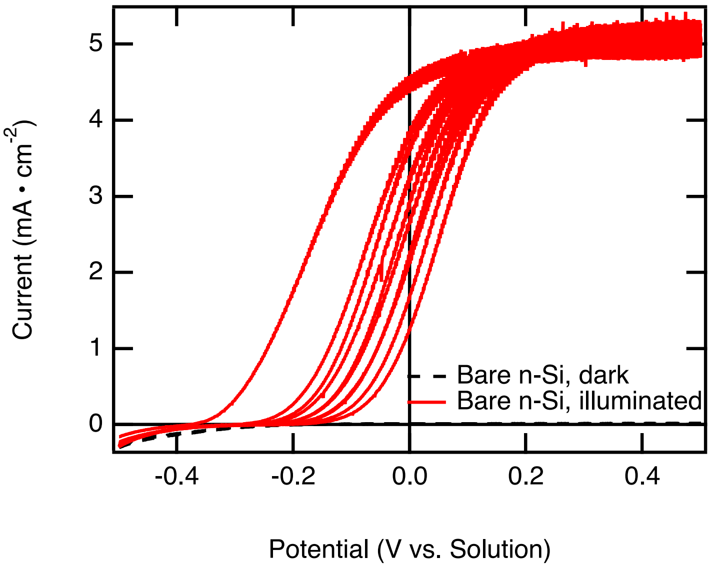

Figure 4A.9. *J-E* behavior (5 cycles at 50 mV s^{-1}) of a bare n-Si electrode exposed to the graphene transfer procedure in $Fe(CN)_6^{3-/4-}{}_{(aq)}$ under approximately 1/10th sun illumination provided by an ELH lamp.

4.6.7 n-Si/Gr and n-Si–H Electrode stability at ~100 mW/cm^2

As seen in figure 4A.10, both the n-Si/Gr and n-Si–H electrodes showed degradation of performance under approximately 1 sun illumination, albeit at reduced rates for the n-Si/Gr electrode. This underscores the need for further strategies, such as methyl termination combined with graphene multiple layers of graphene in order to address the challenging issue of obtaining long-term protection of Si in aqueous solution while evolving oxygen from water.

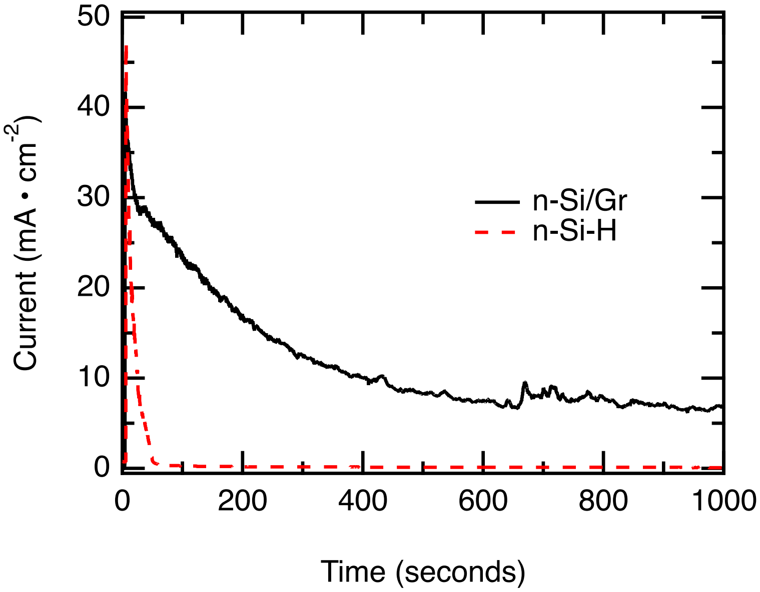

Figure 4A.10. *J–t* behavior of an n-Si/Gr and a n-Si–H electrode in $Fe(CN)_6^{3-/4-}{}_{(aq)}$ under approximately ~100 mW/cm^2 light intensity (ELH lamp) over 1000 s (E = 0 V vs. solution).

4.6.8 Appendix References

1. Petrone, N.; Dean, C. R.; Meric, I.; van der Zande, A. M.; Huang, P. Y.; Wang, L.; Muller, D.; Shepard, K. L.; Hone, J. *Nano Letters* **2012**, *12*, 2751.
2. The $NH_4(S_2O_8)_2$-etched n-Si/Gr electrodes demonstrated slightly larger fill factors than those derived from the $FeCl_3$ etch. However, the $NH_4(S_2O_8)_2$-etched n-Si/Gr electrodes also occasionally exhibited small parallel shunt resistances not indicative of typical photoelectrodes, such as those etched with $FeCl_3$ For these reasons, figure 4.1 and figure 4.3 report electrodes etched with $NH_4(S_2O_8)_2$ were used to obtain the data reported in figure 4.1 and figure 4.3 while electrodes etched with $FeCl_3$ were used to obtain the data reported in Figure 4.2.
3. O'Leary, L. E.; Johansson, E.; Brunschwig, B. S.; Lewis, N. S. *The Journal of Physical Chemistry B* **2010**, *114*, 14298.
4. Connelly, N. G.; Geiger, W. E. *Chemical Reviews* **1996**, *96*, 877.
5. Ferrari, A. C.; Basko, D. M. *Nat Nano* **2013**, *8*, 235.
6. Ni, Z.; Wang, Y. Y.; Yu, T.; Shen, Z. *Nano Res* **2008**, *1*, 273.
7. Ponomarenko, L. A.; Yang, R.; Gorbachev, R. V.; Blake, P.; Mayorov, A. S.; Novoselov, K. S.; Katsnelson, M. I.; Geim, A. K. *Physical Review Letters* **2010**, *105*, 136801.
8. Sze, S. M.; Ng, K., K. *Physics of Semiconductor Devices*; 3rd ed.; John Wiley & Sons, Inc.: Hoboken, NJ, 2007.
9. Gerischer, H. *Physical Chemistry: An Advanced Treatise*; Academic Press: New York, 1970; Vol. IXA, Electrochemistry.

10. Serpone, N.; Pelizzetti, E. *Photocatalysis: Fundamentals and Applications*; John Wiley & Sons, Inc.: Hoboken, NJ, 1989.
11. Yan, R.; Zhang, Q.; Li, W.; Calizo, I.; Shen, T.; Richter, C. A.; Hight-Walker, A. R.; Liang, X.; Seabaugh, A.; Jena, D.; Xing, H. G.; Gundlach, D. J.; Nguyen, N. V. *Applied Physics Letters* **2012**, *101*, 022105.
12. Bard, A. J.; Bocarsly, A. B.; Fan, F. R. F.; Walton, E. G.; Wrighton, M. S. *Journal of the American Chemical Society* **1980**, *102*, 3671.
13. Bard, A. J.; Faulkner, L. R. *Electrochemical Methods: Fundamentals and Applications*; 2nd ed.; John Wiley & Sons, Inc.: Hoboken, NJ, 2001.
14. Briggs, D.; Seah, M. P. *Practical Surface Analysis*; 2nd ed.; John Wiley & Sons Ltd, 1990.
15. Hochella Jr, M. F.; Carim, A. H. *Surface Science* **1988**, *197*, L260.
16. Haber, J. A.; Lewis, N. S. *The Journal of Physical Chemistry B* **2002**, *106*, 3639.

Chapter 5

Lightly Fluorinated Graphene as a Barrier Layer to n-type Si(111) Photoanodes

5.1 Background and Introduction

The behavior of n-Si(111) photoanodes covered by monolayer sheets of fluorinated graphene (F–Gr) was investigated under a range of chemical and electrochemical conditions. The electrochemical behavior of n-Si/F–Gr and np$^+$-Si/F–Gr photoanodes was compared to hydride-terminated n-Si (n-Si–H) electrodes in contact with aqueous $Fe(CN)_6^{3-/4-}$ and Br_2/HBr electrolytes as well as in contact with a series of outer-sphere, one-electron redox couples in nonaqueous electrolytes. Illuminated n-Si/F–Gr and np$^+$-Si/F–Gr electrodes in contact with an aqueous $[K_3(Fe(CN)_6]/[K_4(Fe(CN)_6]$ exhibited stable short-circuit photocurrent densities of ~10 mA cm^{-2} for > 100,000 s (>24 hours), in comparison to bare Si electrodes, which yielded nearly a complete photocurrent decay over ~100 s. X-ray photoelectron spectra collected before and after exposure to aqueous anodic conditions showed that oxide formation at the Si surface was significantly inhibited for Si electrodes coated with F–Gr relative to bare Si electrodes exposed to the same conditions. The variation of the open-circuit potential for n-Si/F–Gr in contact with a series of nonaqueous electrolytes of varying reduction potential indicated that the n-Si/F–Gr did not form a buried junction with respect to the solution contact. Further, illuminated n-Si/F-Gr electrodes in contact with Br_2/HBr(aq) were significantly more stable than n-Si–H electrodes over three cyclic voltammetry sweeps, and n-Si/F-Gr electrodes coupled to a Pt catalyst exhibited ideal regenerative cell efficiencies of up to 5% for the oxidation of Br^- to Br_2.

Several protective coating strategies have been developed to suppress deleterious surface reactions associated with corrosion or passivation of semiconductor photoanodes in aqueous electrolytes.[1,2] Nickel Oxide (NiO_x) films prepared by reactive sputtering or amorphous TiO_2 films in conjunction with a NiO_x based electrocatalyst have produced extended stability for Si photoanodes and allow the photochemical evolution of O_2(g) from water under alkaline conditions.[3,4] Thin metallic overlayers or transparent conductive metal oxide protective layers often result in relatively low photovoltages due to thermionic emission of majority carriers at Si/overlayer Schottky contacts.[3-10] Insulating metal oxide barriers must be thin enough (a few nm) to permit conduction by tunneling, and such thin layers are difficult to prepare in a pinhole-free manner over macroscopic areas.[5,11,12] Chemical functionalization has led to improved stability of n-Si surfaces, but such methods have not yet yielded stability over extended time periods in aqueous electrolytes.[13-15]

An ideal protective coating would be transparent, provide low resistance to charge transfer, allow for maximum energy-conversion efficiency for a range of semiconductor/electrolyte contacts, be applied easily to semiconductor surfaces, be capable of uniformly protecting macroscopic electrode areas, and be chemically and electrochemically stable under the relevant conditions. Monolayer graphene can be prepared in large (>100 cm^2), pinhole-free layers and transferred to any arbitrary planar surface, and has been shown to inhibit oxidation of metals both in air and in aqueous solution.[16-21] Graphene is chemically inert, optically transparent, can be deposited onto surfaces at room temperature. Illuminated graphene-coated Si photoanodes in contact with neutral pH aqueous electrolytes have demonstrated stability for over 1000 s while providing desirable photoelectrochemical performance.[22-25] However, the graphene does not completely protect the Si photoanodes from oxidation, and the devices exhibit partial Fermi-level pinning, which limits their energy-conversion efficiency. The incomplete protection and Fermi-level pinning are consistently ascribed to reactive sites near grain boundaries in the polycrystalline graphene produced by chemical-vapor deposition (CVD), and to the presence of mid-gap electronic states introduced at the n-Si/Gr interface as a result of the graphene electronic structure, respectively.

Relative to unfluorinated graphene, fluorination of graphene should reduce the density of states near the Fermi level, thus reducing Fermi level pinning effects, and should passivate reactive graphene defect sites via fluorine capping.[26-28] Accordingly, we report herein an investigation of the stability and photoelectrochemical behavior of fluorinated-graphene-coated Si photoanodes in contact with aqueous electrolytes.

5.2 Behavior of fluorinated-graphene-covered n-Si photoelectrodes

5.2.1. Stability of F-Gr covered n-Si surfaces in aqueous solution

Detailed experimental procedures are provided in the chapter 5 appendix. Briefly, monolayer sheets of lightly fluorinated graphene (<10 atom% F) were fabricated by treating CVD-grown graphene on a Cu foil with $XeF_2(g)$.[28] X-ray photoelectron spectroscopy (XPS) of the resulting F–Gr confirmed the fluorination.[27,28] The F–Gr was further characterized by UV/Vis and Raman spectroscopy (see SI). The fluorinated graphene sheets were transferred to n-Si and np^+-Si electrodes using standard CVD graphene growth and transfer methods.[29,30]

Figure 5.1 shows the current-density vs. time (*J-t*) and current density vs. potential (*J-E*) behavior for illuminated (~33 mW cm^{-2} ENH-type W-halogen lamp) n-Si/F–Gr photoanodes in contact with aqueous 50 mM $Fe(CN)_6^{3-}$ - 350 mM $Fe(CN)_6^{4-}$ (aq). The n-Si/F–Gr electrodes exhibited stable current over 100 s while the current density of n-Si–H electrodes decayed to nearly baseline values over the same time period (Figure 5.1a). Furthermore, the current density of the n-Si/F–Gr electrode decayed by less than 1 mA cm^{-2} over 100,000 s of continuous operation (Figure 5.1b). After correcting for fluctuations in the light intensity impinging on the electrode, greater than 97% of the expected current density of an ideally stable electrode was observed. Similar results were observed for np^+-Si/F–Gr electrodes (see appendix). Figure 5.1c depicts the *J-E* behavior before and after exposure to the conditions in Figure 5.1b. The stable open-circuit potential (-0.27 V vs. $E(A/A^-)$) and fill factor (*ff,* 0.33 before exposure, 0.32 after exposure) attest to the stability of the n-Si/F–Gr interface.

Prior to the stability test, the open-circuit potential (E_{oc}) of the n-Si/F–Gr electrode was -0.27 V vs. $E(A/A^-)$, approximately 70 mV lower than the reported E_{oc} of -0.34 V vs. $E(A/A^-)$ for n-Si coated with a single layer of graphene.[22] Further, exposure of n-Si/F-Gr to a series of non-aqueous electrolytes of varying electrochemical potential showed a dependence of E_{oc} on $E(A/A^-)$, indicating partial Fermi level pinning of the n-Si surface with respect to the solution potential. The mutually similar fill factors (*ff*) of the n-Si/F–Gr electrode and np^+-Si/F–Gr electrodes, 0.33 and 0.30, respectively (Figure 5.1c, Figure 5A.1), indicated similar limiting resistance to charge transfer in both systems.

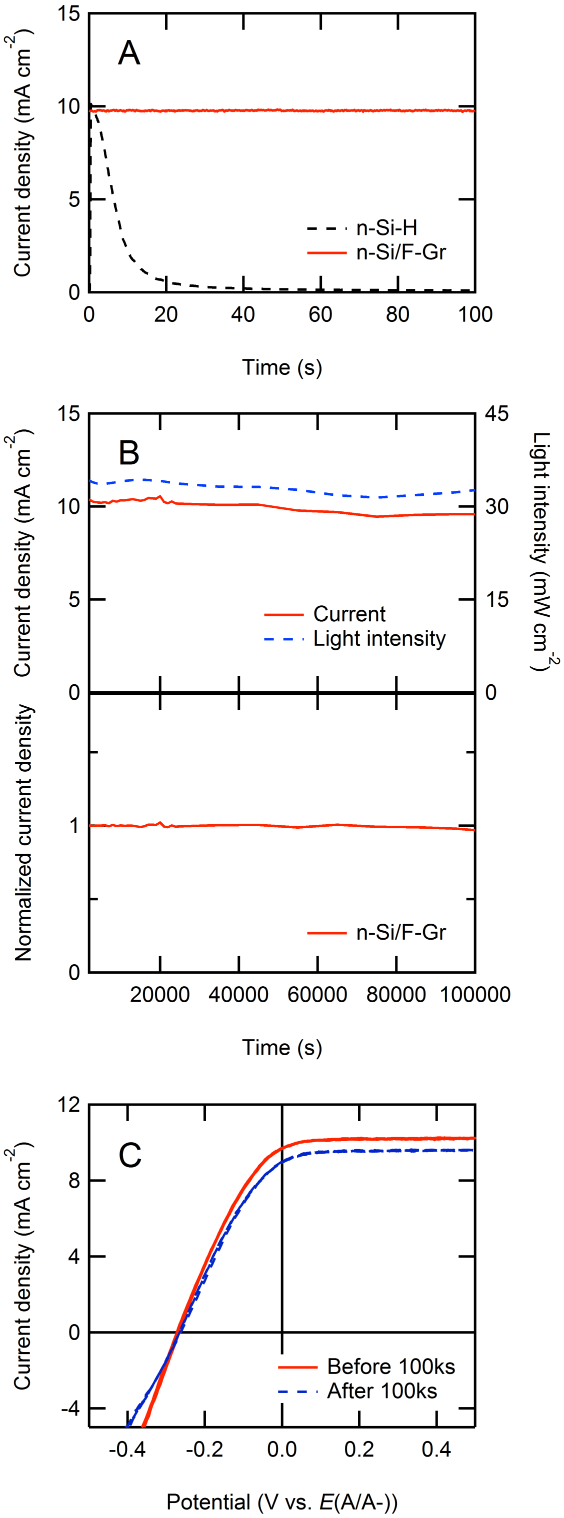

Figure 5.1. Current density-time (*J-t*) and current density-potential (*J-E*) behavior of n-Si/F–Gr electrodes in contact with aqueous 50 mM $Fe(CN)_6^{3-}$ - 350 mM $Fe(CN)_6^{4-}$ under ~ 33 mW cm^{-2} of ENH-type W-halogen lamp illumination. (A) Comparison of the *J-t* behavior of bare n-Si–H and n-Si/F-Gr electrodes over 100 s. (B) The *J-t* behavior of F–Gr covered n-Si at *E* = 0 V vs. the Nernstian potential of the solution (*E*(A/A$^-$)) over 100,000 s (>24 hours). The normalized current density is reported to correct for any variation in the intensity of the light source with time. (C) *J-E* behavior of n-Si/F–Gr (3 scans at 50 mV s^{-1}) before and after exposure to the conditions depicted in (B).

5.2.2. Inhibition of silicon oxide formation at F-Gr-covered n-Si surfaces

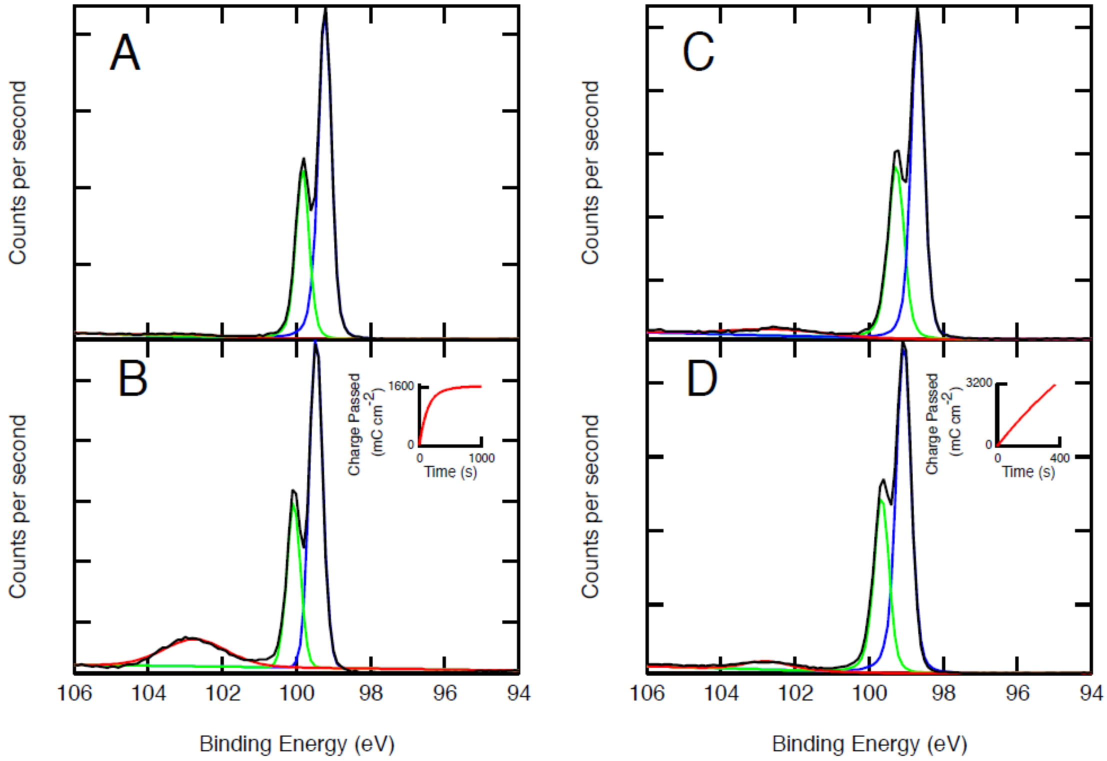

Figure 5.2. XP spectra of n-Si–Me and n-Si–Me/F–Gr electrodes. (A) and (B) show the XP spectra of an n-Si–Me electrode before and after passing 1600 mC cm^{-2} (inset) while passing anodic current in contact with an aqueous 50 mM $Fe(CN)_6^{3-}$ - 350 mM $Fe(CN)_6^{4-}$ electrolyte. (C) and (D) show an n-Si–Me/F–Gr electrode before and after passing 3200 mC cm^{-2} under similar electrochemical conditions to (A) and (B).

Figure 5.2 shows a comparison of the XP spectra of methyl-terminated n-Si electrodes (n-Si–Me) with and without a F–Gr protective layer before and after photoelectrochemical testing in an aqueous 50 mM $Fe(CN)_6^{3-}$ - 350 mM $Fe(CN)_6^{4-}$ electrolyte. After passing 1600 mC cm^{-2} of anodic charge on an n-Si-Me electrode, the growth of an oxide peak was observed in the Si 2p XPS region and was consistent with formation of multiple layers of oxide. In contrast, no additional growth of the oxide peak was observed after passing twice the number of Coulombs (3200 mC cm^{-2}) across an n-Si–Me/F–Gr electrode (See appendix). Hence, F–Gr acts as a physical barrier to oxide formation, preserving the photoelectrochemical behavior of the n-Si-Me/solution interface. Methylated surfaces were used because, in contrast with n-Si–H surfaces, the n-Si–Me surface does not easily oxidize in air nor forms significant oxide upon fabrication of n-Si/F–Gr interfaces, allowing more facile observation of oxide growth in the presence various protective layers, such as F–Gr. F-Gr covered Si surfaces did not form platinum silicide upon evaporation of Pt onto the F–Gr/Si surface, and F–Gr is stable in both aqueous and acidic (pH 0) solutions, suggesting F–Gr also provides as an effective physical barrier to inhibit Pt/Si reactivity and is stable under harsh fabrication and electrolyte conditions (see appendix).

5.2.3. Photoelectrochemical behavior of F-Gr/n-Si interfaces under bromide oxidation conditions

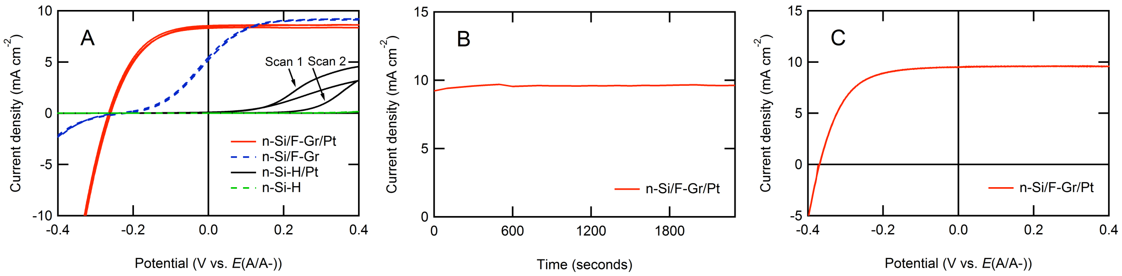

Figure 5.3. Electrochemical behavior of n-Si/F–Gr and n-Si–H electrodes with and without Pt deposition in aqueous 0.4 M Br_2 – 7.0 M HBr (pH = 0) electrolyte under 33 mW cm^{-2} from an ELH-type W-halogen lamp). (A) *J-E* behavior of n-Si/F–Gr and n-Si–H electrodes with and without Pt deposition. Each cyclic voltammogram was started at +0.4 V vs. *E*(A/A$^-$) and swept twice to more negative potentials at 50 mV s^{-1}. (B) *J-t* behavior of an n-Si/F–Gr/Pt electrode over 45 min at *E* = 0 V vs. *E*(A/A$^-$) (C) *J-E* behavior of an n-Si/F–Gr/Pt electrode after exposure to conditions described in (B).

Figure 5.3 displays the *J-E* behavior of n-Si–H and n-Si/F–Gr electrodes under ~33 mW cm^{-2} illumination intensity in contact with 0.4 M Br_2 – 7.0 M HBr (pH=0), with and without electrochemical deposition of 100 mC cm^{-2} of a Pt catalyst, respectively. With the Pt catalyst, the properties of the n-Si/F–Gr/Pt electrode improved to E_{oc} (n-Si/F–Gr/Pt) = 0.26 V, *ff* = 0.52, and J_{sc} = 8.3 mA/cm^2 from E_{oc} (n-Si/F–Gr) = 0.22 V, *ff* = 0.16, J_{sc} = 5.14 mA cm $^{-2}$. The improved *ff* can be ascribed to improved catalysis for the Br^- to Br_2 reaction effected by the Pt. The current density of the n-Si–H/Pt electrode under illumination decayed precipitously over two potential sweeps, while the n-Si/F–Gr/Pt electrode showed a stable *ff* and photocurrent density under the same conditions. The n-Si/F–Gr/Pt electrode had an ideal regenerative cell efficiency (η_{IRC}) of 3.5% in contact with the Br_2/HBr (aq) electrolyte.[31] The current density at n-Si/F-Gr/Pt electrodes was stable over 45 min at E = 0 V vs. the Nernstian potential of the solution, $E(A/A^-)$ and η_{IRC} increased to 5% over this time (See appendix). The improvement in η_{IRC} indicates a change in the energetics of the n-Si/F–Gr/Pt interface after electrochemical deposition of Pt.

5.3 Conclusion

Although only lightly fluorinated (C_xF, x > 10) graphene was used herein, these fluorinated graphene sheets provided superior protection against corrosion to the underlying Si relative to the protection imparted by monolayer graphene on n-Si(111) photoanodes (See appendix).[22] These results are consistent with the hypothesis that light fluorination of graphene induces reaction with high-energy defect sites, such as dangling bonds or missing atoms, effectively sealing defects that otherwise would allow oxide formation at the n-Si surface and further degradation of the Gr protective layer. The bonding of a very electronegative atom to the surface may also increase the hydrophobicity of the graphene sheet, which would further reduce deleterious corrosion reactions near pinholes.

In conclusion, fluorinated graphene forms an effective physical barrier between silicon surfaces and a number of contacting phases, including acidic and neutral pH aqueous electrolyte as well as metallic interfaces. Additionally, Si covered by fluorinated graphene exhibits partial Fermi level pinning in contact with non-aqueous electrolytes. Additional work at higher fluorination levels on both p-type and n-type silicon will elucidate whether a reduction in the density of states near the Fermi level can lead to a fully unpinned interface, and will allow elucidation of the effect of the graphene-based surface dipole on the electrochemical behavior of the resultant photoelectrode.

5.4 Acknowledgements

The bulk of this work will soon appear in publication. Annelise Thompson was an equal contributor to these efforts and I am also thankful to Chris Roske, Jackie Maslyn, Yufeng Hao and Noah Plymale for their invaluable contributions to this work.

5.5 References

1. S. Hu, N. S. Lewis, J. W. Ager, J. Yang, J. R. McKone and N. C. Strandwitz, *J. Phys. Chem. C*, 2015, **119**, 24201-24228.
2. K. Sun, S. Shen, Y. Liang, P. E. Burrows, S. S. Mao and D. Wang, *Chem. Rev.*, 2014, **114**, 8662-8719.
3. K. Sun, M. T. McDowell, A. C. Nielander, S. Hu, M. R. Shaner, F. Yang, B. S. Brunschwig and N. S. Lewis, *J. Phys. Chem. Lett.*, 2015, **6**, 592-598.
4. S. Hu, M. R. Shaner, J. A. Beardslee, M. Lichterman, B. S. Brunschwig and N. S. Lewis, *Science*, 2014, **344**, 1005-1009.
5. N. C. Strandwitz, D. J. Comstock, R. L. Grimm, A. C. Nichols-Nielander, J. Elam and N. S. Lewis, *J. Phys. Chem. C*, 2013, **117**, 4931-4936.
6. D. Bélanger, J. P. Dodelet and B. A. Lombos, *J. Electrochem. Soc.*, 1986, **133**, 1113-1119.
7. A. Q. Contractor and J. O. M. Bockris, *Electrochim. Acta*, 1984, **29**, 1427-1434.
8. A. T. Howe, R. T. Hawkins and T. H. Fleisch, *J. Electrochem. Soc.*, 1986, **133**, 1369-1375.
9. S. Menezes, A. Heller and B. Miller, *J. Electrochem. Soc.*, 1980, **127**, 1268-1273.
10. S. M. Sze and K. Ng, K., *Physics of Semiconductor Devices*, John Wiley & Sons, Inc., Hoboken, NJ, 3rd edn., 2007.
11. Y. W. Chen, J. D. Prange, S. Dühnen, Y. Park, M. Gunji, C. E. D. Chidsey and P. C. McIntyre, *Nat. Mater.*, 2011, **10**, 539-544.
12. S. J. Fonash, *Solar Cell Device Physics*, Elsevier Inc., Amsterdam, 2nd edn., 2010.

13. A. Bansal and N. S. Lewis, *J. Phys. Chem. B*, 1998, **102**, 4058-4060.

14. A. Bansal and N. S. Lewis, *J. Phys. Chem. B*, 1998, **102**, 1067-1070.

15. J. M. Bolts, A. B. Bocarsly, M. C. Palazzotto, E. G. Walton, N. S. Lewis and M. S. Wrighton, *J. Am. Chem. Soc.*, 1979, **101**, 1378-1385.

16. S. Chen, L. Brown, M. Levendorf, W. Cai, S.-Y. Ju, J. Edgeworth, X. Li, C. W. Magnuson, A. Velamakanni, R. D. Piner, J. Kang, J. Park and R. S. Ruoff, *ACS Nano*, 2011, **5**, 1321-1327.

17. G. W. Flynn, *J. Chem. Phys.*, 2011, **135**, 050901-050908.

18. Y. Lee, S. Bae, H. Jang, S. Jang, S.-E. Zhu, S. H. Sim, Y. I. Song, B. H. Hong and J.-H. Ahn, *Nano Lett.*, 2010, **10**, 490-493.

19. D. Prasai, J. C. Tuberquia, R. R. Harl, G. K. Jennings and K. I. Bolotin, *ACS Nano*, 2012, **6**, 1102-1108.

20. J. W. Suk, A. Kitt, C. W. Magnuson, Y. Hao, S. Ahmed, J. An, A. K. Swan, B. B. Goldberg and R. S. Ruoff, *ACS Nano*, 2011, **5**, 6916-6924.

21. E. Sutter, P. Albrecht, F. E. Camino and P. Sutter, *Carbon*, 2010, **48**, 4414-4420.

22. A. C. Nielander, M. J. Bierman, N. Petrone, N. C. Strandwitz, S. Ardo, F. Yang, J. Hone and N. S. Lewis, *J. Am. Chem. Soc.*, 2013, **135**, 17246-17249.

23. S. Droscher, P. Roulleau, F. Molitor, P. Studerus, C. Stampfer, K. Ensslin and T. Ihn, *Appl. Phys. Lett.*, 2010, **96**, 152104-152103.

24. L. A. Ponomarenko, R. Yang, R. V. Gorbachev, P. Blake, A. S. Mayorov, K. S. Novoselov, M. I. Katsnelson and A. K. Geim, *Phys. Rev. Lett.*, 2010, **105**, 136801.

25. S. Bae, H. Kim, Y. Lee, X. Xu, J.-S. Park, Y. Zheng, J. Balakrishnan, T. Lei, H. Ri Kim, Y. I. Song, Y.-J. Kim, K. S. Kim, B. Ozyilmaz, J.-H. Ahn, B. H. Hong and S. Iijima, *Nat. Nano.*, 2010, **5**, 574-578.

26. R. R. Nair, W. Ren, R. Jalil, I. Riaz, V. G. Kravets, L. Britnell, P. Blake, F. Schedin, A. S. Mayorov, S. Yuan, M. I. Katsnelson, H.-M. Cheng, W. Strupinski, L. G. Bulusheva, A. V. Okotrub, I. V. Grigorieva, A. N. Grigorenko, K. S. Novoselov and A. K. Geim, *Small*, 2010, **6**, 2877-2884.

27. J. T. Robinson, J. S. Burgess, C. E. Junkermeier, S. C. Badescu, T. L. Reinecke, F. K. Perkins, M. K. Zalalutdniov, J. W. Baldwin, J. C. Culbertson, P. E. Sheehan and E. S. Snow, *Nano Lett.*, 2010, **10**, 3001-3005.

28. R. Stine, W.-K. Lee, K. E. Whitener, J. T. Robinson and P. E. Sheehan, *Nano Lett.*, 2013, **13**, 4311-4316.

29. N. Petrone, C. R. Dean, I. Meric, A. M. van der Zande, P. Y. Huang, L. Wang, D. Muller, K. L. Shepard and J. Hone, *Nano Lett.*, 2012, **12**, 2751-2756.

30. Y. Hao, M. S. Bharathi, L. Wang, Y. Liu, H. Chen, S. Nie, X. Wang, H. Chou, C. Tan, B. Fallahazad, H. Ramanarayan, C. W. Magnuson, E. Tutuc, B. I. Yakobson, K. F. McCarty, Y.-W. Zhang, P. Kim, J. Hone, L. Colombo and R. S. Ruoff, *Science*, 2013, **342**, 720-723.

31. R. H. Coridan, A. C. Nielander, S. A. Francis, M. T. McDowell, V. Dix, S. M. Chatman and N. S. Lewis, *Energy Environ. Sci.*, 2015, **8**, 2886-2901.

5.6 Appendix

5.6.1 Methods

5.6.1.1 Materials

Single-crystalline, Czochralski grown, (111)-oriented, planar, 380 µm thick, phosphorus doped, 1.1 Ω-cm resistivity (doping density, $N_D \approx 5x10^{15}$ cm^{-3}) single-side polished n-type silicon wafers were obtained from University Wafer, Inc. Water was obtained from a Barnstead Nanopure system and had a resistivity ≥ 18.0 MΩ-cm. Copper Etch Type CE – 100 ($FeCl_3$-based, Transene Company, Inc., Danvers, MA), and buffered HF(aq) (semiconductor grade, Transene Company, Inc., Danvers, MA) were used as received. Acetone (HPLC grade, Sigma-Aldrich) was used as received. Acetonitrile (99.8% anhydrous, Sigma-Aldrich) used in electrochemical measurements was dried over Al_2O_3 prior to use.

Ferrocene (Fc, bis(cyclopentadienyl)iron(II), 99%, Strem), cobaltocene ($CoCp_2$, bis(cyclopentadienyl)cobalt(II), 98%, Strem), and acetylferrocene (AcFc, (acetylcyclopentadienyl)-cyclopentadienyl iron(II), 99.5%, Strem) were purified via sublimation. Ferrocenium tetrafluoroborate ($Fc^+[BF_4]^-$, bis(cyclopentadienyl)iron(III) tetrafluoroborate, technical grade, Sigma-Aldrich) was recrystallized from a mixture of diethyl ether (ACS grade, EMD) and acetonitrile (ACS grade, EMD) and dried under vacuum. Cobaltocenium hexafluorophosphate ($CoCp_2^+$, bis(cyclopentadienyl)cobalt(III) hexafluorophosphate, 98%, Sigma-Aldrich) was recrystallized from a mixture of ethanol (ACS grade, EMD) and acetonitrile (ACS grade, EMD) and dried under vacuum. Acetylferrocenium ($AcFc^+$) was generated in situ via electrochemical oxidation of $AcFc^0$

with the concomitant reduction reaction occurring in a compartment that was separated by a Vycor frit from the working electrode compartment. Potassium ferricyanide ($K_3[Fe(CN)_6]$, 99.2%, Sigma-Aldrich) and potassium ferrocyanide ($K_4[Fe(CN)_6]•3H_2O$, ACS Certified, Fischer Scientific) were used as received. $LiClO_4$ (battery grade, Sigma-Aldrich) was used as received. Petri dishes used were Falcon Optilux™ branded and were cleaned with water prior to use. All other chemicals were used as received unless otherwise noted.

5.6.1.2 Electrode fabrication

Monolayer graphene was grown by chemical-vapor deposition (CVD) of carbon on Cu.[1] Additional CVD-grown monolayer graphene on Cu was purchased from Advanced Chemical Supplier Materials.

A 2.5 cm x 1 cm piece of monolayer graphene on Cu (from either source) was fluorinated using a home-built XeF_2 pulse chamber, with one pulse of XeF_2 (g) at 2 Torr for 90 s with a base pressure of <1 mTorr. The fluorinated graphene samples on Cu were then coated with 495K A4 polymethyl methacrylate (PMMA, MicroChem) by spinning at 2000 rpm (500 rpm s^{-1} acceleration) for 60 s, followed by a 5 min bake at 185 °C. This procedure was repeated twice to yield a PMMA/F-Gr/Cu stack.

Smaller pieces were cut from the PMMA/F-Gr/Cu and floated in $FeCl_3$ solution until complete removal of the Cu (~1 h) was observed. To remove the etchant residue, each stack was transferred between five consecutive ≥18MΩ-cm resistivity water baths. N-type Si was etched for 30 s in buffered improved HF (Transene) to yield n-Si–H surfaces, and any SiO_2 was removed using a modified SC1/SC2 cleaning method. SC-1 consisted of soaking the Si wafers in a 5:1:1 (by volume) solution of H_2O, NH_4OH (~30 wt.%, J.T. Baker) and H_2O_2 (~35 wt.%, Sigma) for 10 min at 75° C. After washing with H_2O, SC-1 cleaned wafers were exposed to SC-2 conditions, which consisted of soaking the Si wafers in a 5:1:1 (by volume) solution of H_2O, HCl (11.1 M, Sigma) and H_2O_2 (~35 wt.%, Sigma) for 10 min at 75 °C. A clean PMMA/F-Gr stack was then pulled gently onto the appropriate Si wafer and dried with a stream of $N_2(g)$ to remove any remaining water between the Si wafer and the graphene sheet. The final PMMA/F-Gr/wafer stack was baked at 80 °C for 10 min in air. The majority of the PMMA was detached with a 10 min acetone soak and the remaining PMMA residue was removed by an anneal (H_2:Ar v:v 5:95) for 2h at 350 °C.[2]

Si/F-Gr electrodes were fabricated using Ga:In (75:25) eutectic as an ohmic back contact. The wafers were attached to a Cu wire with Ag paint (high purity, SPI Supplies). All surfaces except the F–Gr layer were covered with insulating epoxy (Loctite Hysol 9460). CH_3-terminated Si(111) wafers were prepared using a previously reported procedure.[3] H-terminated Si(111) electrodes were etched with HF(aq) immediately before use.

5.6.1.3 Instrumentation

X-ray photoelectron spectroscopic (XPS) data were collected at $\sim 5 \times 10^{-9}$ Torr using a Kratos AXIS Ultra DLD with a magnetic immersion lens that consisted of a spherical mirror and concentric hemispherical analyzers with a delay-line detector (DLD). An Al Kα (1.486 KeV) monochromatic source was used for X-ray excitation. Ejected electrons were collected at a 90° angle from the horizontal. The CASA XPS software package v 2.3.16 was used to analyze the collected data.

Raman spectra were collected with a Renishaw Raman microscope at λ=532 nm through an objective with numerical aperture=0.75. The laser power was ~ 3 mW.

UV/Vis transmission spectra were collected with a Cary 5000 absorption spectrometer equipped with an external DRA 1800 attachment. The data were automatically zero/baseline corrected by the instrument before any additional processing was performed.

Electrochemical data were obtained using a Princeton Applied Research Model 273, Biologic SP-250, or a Gamry Reference 600 potentiostat. A Pt wire reference electrode (0.5 mm dia., 99.99% trace metals basis, Sigma-Aldrich) and a Pt mesh counter electrode (100 mesh, 99.9% trace metals basis, Sigma-Aldrich) were used for the electrochemical measurements. The cell potentials for the nonaqueous redox species were determined using cyclic voltammetry to compare the solution potential to the formal potential of the redox species. The potential difference between cells was calculated using the difference between the formal potentials for each redox couple in conjunction with standard reduction potentials from the literature. The CH_3CN-$CoCp_2^{+/0}$ solution ($CoCp_2$ [3 mM]/ $CoCp_2^+$ [50 mM]) was calculated to have a solution potential of $E(A/A^-)$ = -1.26 V vs Fc/Fc^+, the CH_3CN-$Fc^{+/0}$ solution (Fc [55 mM]/ Fc^+ [3 mM]) was calculated to have $E(A/A^-)$ = -0.10 V vs Fc^+/Fc, and the CH_3CN-$AcFc^{+/0}$ solution (pre-electrolysis AcFc concentration = [50 mM]) was calculated to have $E(A/A^-)$ = +0.40 V vs Fc^+/Fc. The nonaqueous electrochemical solutions each contained 1.0 M $LiClO_4$. The aqueous 50 mM $K_3[Fe(CN)_6]$ - 350 mM $K_4[Fe(CN)_6]$ solution contained no additional supporting electrolyte due to the high intrinsic salt concentration. The current under forward bias saturated at much larger values in the $Fe(CN)_6^{3-/4-}$ solution than in the Fc^+/Fc solution due of the increased concentration of electron-accepting species in the $Fe(CN)_6^{3-/4-}$ solution. $Fc[BF_4]$ is a highly colored species that, at high concentrations, absorbs a significant fraction of the light prior to photons striking the photoelectrode. The electrolyte solution was rapidly stirred with a small, Teflon-covered stir bar. Illumination was provided with an ENH-type tungsten-halogen lamp. Illumination intensities were set to provide ~10-11 mA cm^{-2} of light-limited current density. These intensities corresponded to ~1/3rd of a Sun (~33 mW cm^{-2}), respectively, as determined through the concurrent use of a Si photodiode (Thor Laboratories) that was calibrated relative to a secondary standard photodetector that was NIST-traceable and calibrated at 100 mW cm^{-2} of AM1.5G illumination. Nonaqueous electrochemistry was performed anaerobically in an Ar(*g*)-filled glovebox. Aqueous electrochemistry was performed in air. Electrodes were washed with H_2O and dried prior to transfer between electrolyte solutions.

The current density versus potential data in HBr(aq) were measured using a three-electrode setup with a Si working electrode, a Pt wire pseudo-reference electrode, and a large Pt mesh counter electrode. The electrolyte consisted of aqueous 0.4M Br_2 - 7.0 M HBr (pH=0) electrolyte under rapid stirring, and ~33 mW cm^{-2} of simulated solar illumination from an ELH-type W-halogen lamp.

Photoelectrochemical deposition of Pt was performed by immersing the electrode into an aqueous solution of 5 mM K_2PtCl_4 (99.9%, Alfa Aesar) and 200 mM LiCl. Using a three-electrode setup, with a saturated calomel reference electrode and a Pt mesh counter electrode, galvanostatic control was maintained at -0.1 mA/cm^2 in a stirred solution until -100 mC/cm^2 had passed. The samples were then rinsed with deionized water and were dried under a stream of N_2(g).

5.6.2 Supporting Data

5.6.2.1 Electrochemical behavior of np$^+$-Si/F–Gr electrodes in aqueous solution

Figure 5A.1 displays the stability data before normalization. The first and last CV for each electrode is also shown. The CVs are not corrected for loss of light-limited current. The current density decay seen in the original chronoamperograms is due to solution decay and fluctuations in the light source as the light-limited current at very positive potentials (+0.4 V) decreased over time, leading to the normalization present in the main text.. Overall, there is little change to the E_{OC}, J_{SC}, and *ff* for either the n-Si or np+Si electrodes before and after testing for 100 ks.

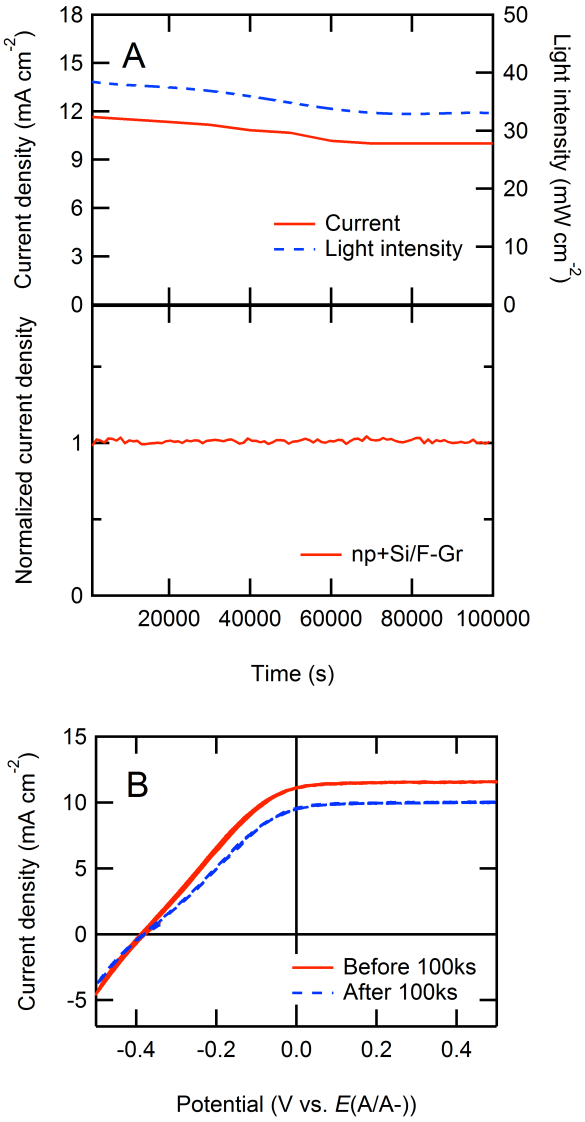

Figure 5A.1. Current density vs. time (*J*-*t*) and current density vs potential (*J*-*E*) behavior of np$^+$-Si/F–Gr electrodes in contact with aqueous 50 mM $Fe(CN)_6^{3-}$ - 350 mM $Fe(CN)_6^{4-}$ electrolyte under ~33 mW cm^{-2} of ENH-type W-halogen illumination. (A) The *J*-t behavior of np$^+$-Si/F–Gr at *E*= 0 V vs. *E*(A/A$^-$) over 100,000 s (>24 h). The normalized current density is reported to correct for any variations in the light intensity during the experiment. (B) *J*-*E* behavior of np$^+$-Si/F–Gr (3 scans at 50 mV s^{-1}) before and after exposure to the conditions depicted in (A). The current density decay in the original chronoamperograms is consistently ascribed to fluctuations in the light source, as well as to decomposition of the $Fe(CN)_6^{3-/4-}$ under illumination, which produced thin colored film on the electrochemical cell over the course of the experiment depicted in (A).

5.6.2.2 Comparison of graphene-imparted stability between graphene growths

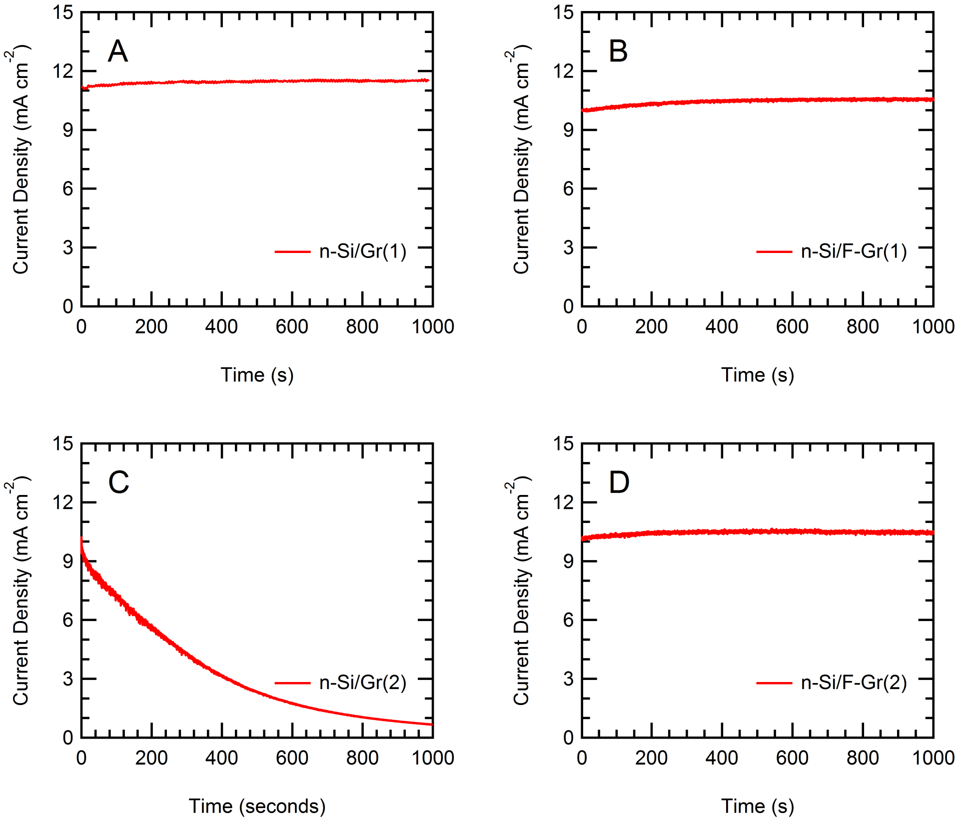

Figure 5A.2. *J-t* data for n-Si/Gr and n-Si/F–Gr electrodes from two different graphene growths in contact with aqueous 50 mM $Fe(CN)_6^{3-}$ - 350 mM $Fe(CN)_6^{4-}$ under ~33 mW cm^{-2} of W-halogen illumination. (A) The n-Si/Gr from the first graphene sheet (growth 1) exhibited stable current densities for > 1000 s. (B) Fluorination of graphene from growth 1 yielded n-Si/F–Gr electrodes that exhibited stable current densities for > 1000 s. (C) Another graphene growth (growth 2) yielded n-Si/Gr electrodes that did not exhibit stable current densities for > 1000 s. (D) When Batch 2 was fluorinated, the n-Si/F–Gr electrodes exhibited stable current densities for > 1000 s. The behavior is consistent with expectations for the stabilization of otherwise unstable graphene arising from fluorine termination of high-energy defect sites in the graphene lattice.

Figure 5A.2 shows that graphene from a CVD growth which exhibited fast decay of current density over the first 1000s of testing in the $Fe(CN)_6^{3/4-}$ couple, can be stabilized by fluorination. The same piece of graphene-covered copper foil was cut into multiple pieces, of which one was fluorinated and the other was not. Several of the electrodes made on n-Si-H from the graphene that was not fluorinated showed a rapid decay over 1000s. However, electrodes made on n-Si-H from the fluorinated graphene demonstrated stability over the same 1000s. We postulate that this ability to stabilize otherwise unstable graphene comes from fluorine termination of high-energy defect sites in the graphene lattice. This passivation of reactive sites increases the stability of the graphene sheet.

5.6.2.3 X-ray Photoelectron Spectroscopy of Fluorinated Graphene

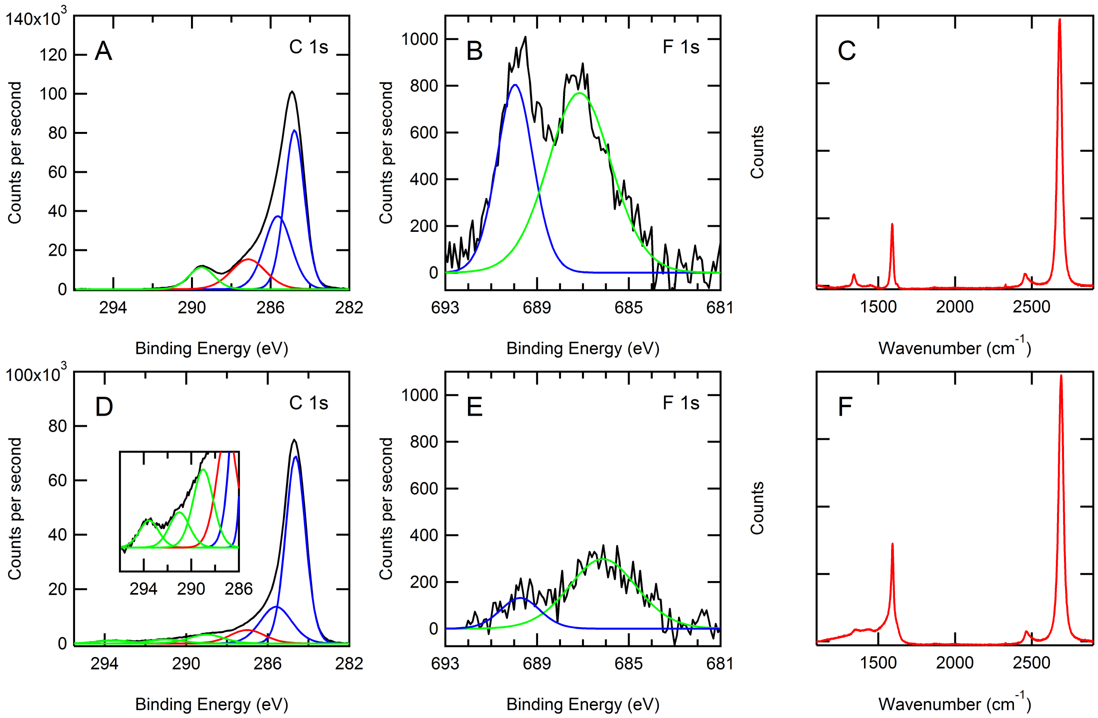

Figure 5A.3 Raman and X-ray photoelectron (XP) spectra of fluorinated graphene (F–Gr) before and after annealing. (A) The C 1s region before annealing displayed four peaks at binding energies of 284.8 eV, 285.6 eV, 287.2 eV, and 289.5 eV, respectively. Peaks attributed to carbon bound to fluorine are shown in green; peaks attributed to carbon bound to carbon are shown in blue; and peaks attributed to carbon bound to oxygen are shown in red. (B) The F 1s region displayed two peaks at binding energies of 687.1 eV and 690.0 eV, respectively. (C) The Raman spectra before annealing showed a prominent defect peak at 1350 cm^{-1}. (D) Two additional peaks, at 291 eV and 293.5 eV (inset), attributable to CF$_2$ and CF$_3$ groups, were observed in the C 1s XP spectra after annealing. (E) The positions of the peaks in the F 1s region were shifted slightly to 686.1 eV and 689.8 eV, respectively, and decreased in size. (F) The defect peak at 1350 cm^{-1} broadened after the anneal. These spectra are consistent with a lightly fluorinated (C$_X$F, x>10) graphene surface.[4] The change in fluorination profile after annealing is consistent with a reorganization of the fluorine on the surface, and the XPS spectra demonstrate the expected decrease in fluorine content after a two-hour 350 °C anneal under a H$_2$:Ar (5:95) atmosphere.[4]

5.6.2.4 Chemical stability of fluorinated graphene in aqueous solutions of varying pH (0,7,14)

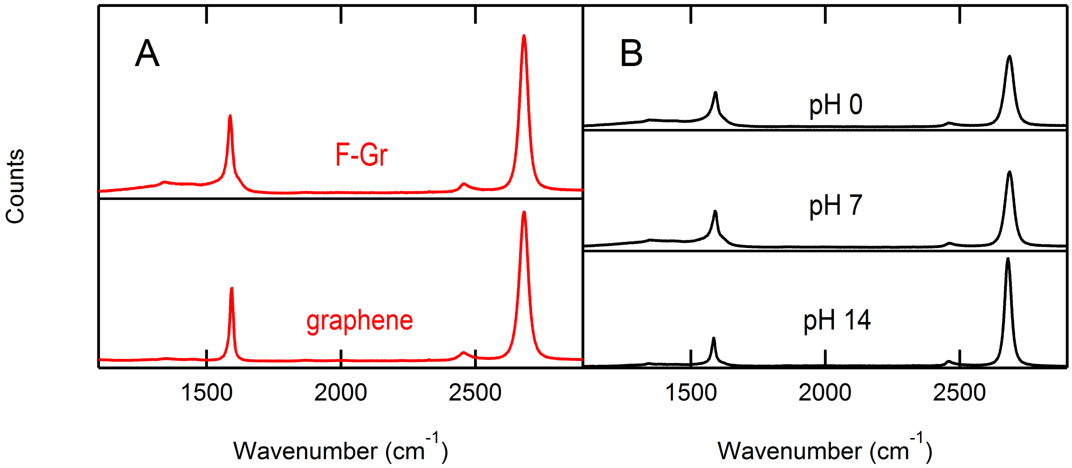

Figure 5A.4. Stability tests of F–Gr in acidic (1 M HCl), alkaline (1 M KOH), and neutral (deionized water) conditions. An initial Raman of the pristine graphene sheets before fluorination and after fluorination showed an increase in the size of the defect peak at 1350 cm^{-1}. This defect peak remained unchanged after 1 h in acidic or neutral solutions. In contrast, immersion for 1 h in alkaline media produced a decrease in the density of the defect peak.

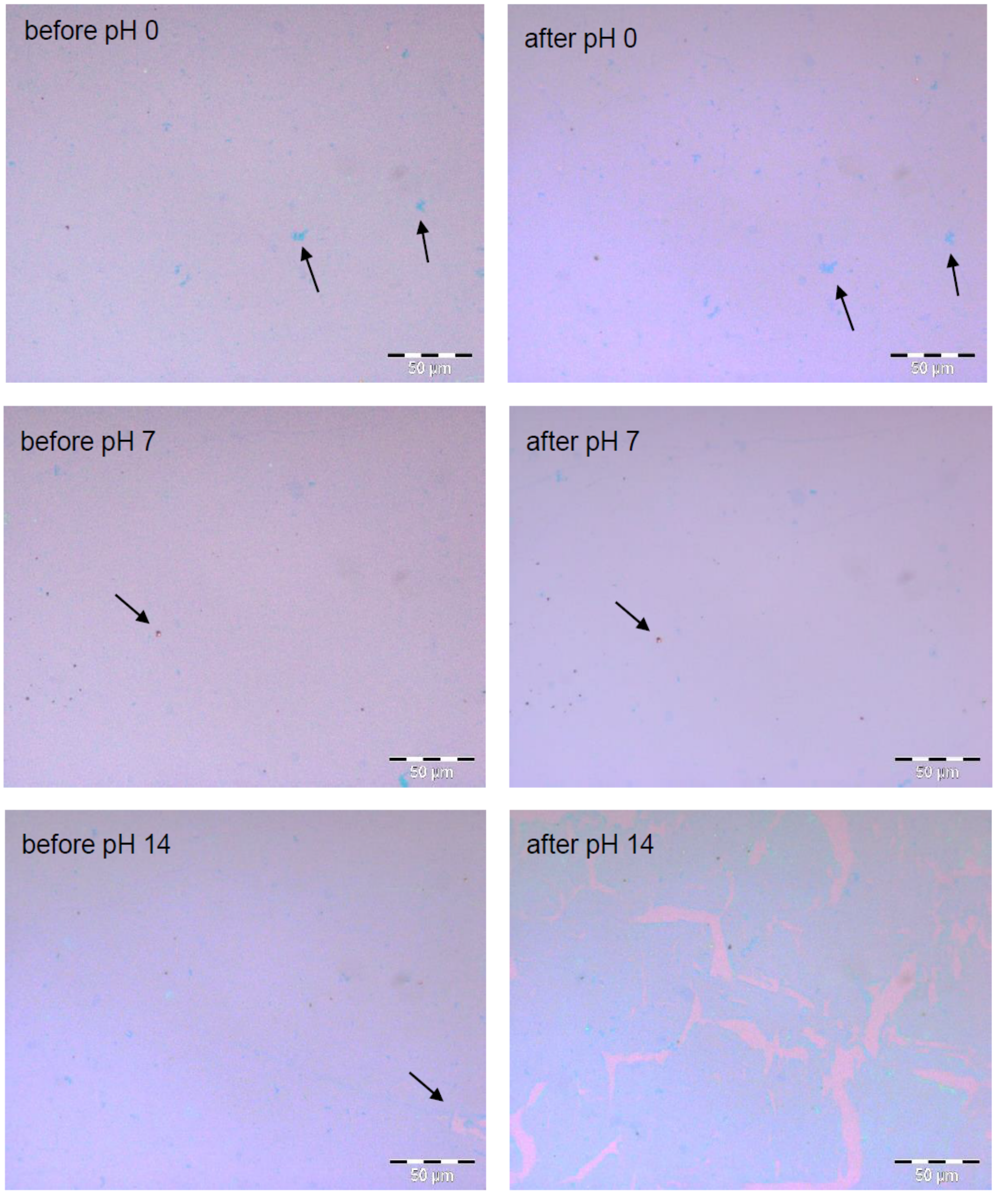

Figure 5A.5. Optical images of stability tests of F–Gr in acidic (1 M HCl), alkaline (1M KOH), and neutral (deioninzed water) conditions. Arrows indicate points of reference for the corresponding before and after images.

The stability of the fluorinated graphene was tested under acidic, neutral, and alkaline aqueous solutions, respectively. To insure that the same area was examined before and after testing, a small area on the graphene wafer was outlined with Hysol 9460 epoxy. Optical images along with Raman spectra were acquired, and wafers were then placed for 1 h in aqueous solutions at pH 0, pH 7, and pH 14. After carefully rinsing the samples with >18 MΩ-cm H_2O and drying the samples with a stream of $N_2(g)$, optical images along with Raman spectra were obtained from the same areas as before testing. The Raman spectra and optical images of the samples soaked in acidic and neutral solutions showed no change after testing (Figure 5A.4). The samples tested in alkaline solutions showed a marked decrease in defect density of the remaining sections of fluorinated graphene, closely mimicking the profile of pristine graphene. Repeated tests of fluorinated graphene in 1 M KOH(aq) showed large-scale delamination of the fluorinated graphene sheet, as observed in the images before and after exposure to the aqueous pH 14 solution.

5.6.2.5 UV-Vis Spectroscopy of Graphene and Fluorinated Graphene

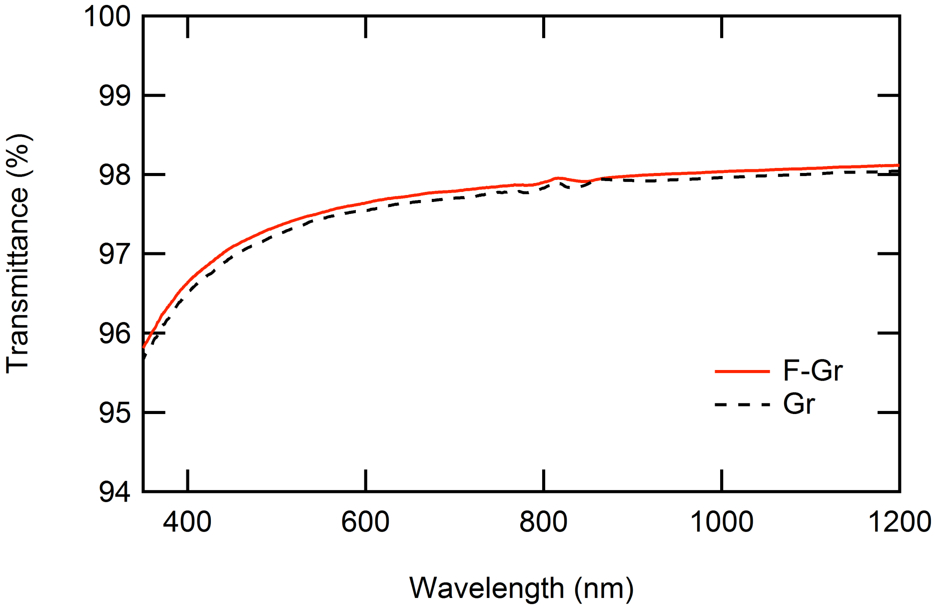

Figure 5A.6. UV/Vis spectra of Gr and F-Gr on glass. Graphene and fluorinated graphene were transferred to borosilicate glass slides using the standard transfer procedures (*vide supra*). The slightly increased transmission for F-Gr is consistent with the expectation of decreased visible light absorption upon fluorination of graphene.

5.6.2.6 Inhibition of platinum silicide formation

XP spectra of Si-Me/F-Gr/Pt and Si-Me/Pt surfaces were obtained to investigate the ability of F-Gr to inhibit platinum silicide formation. Pt was deposited at ~3 nm thickness via electron-beam evaporation on both F-Gr covered and bare Si surfaces. The 3 nm Pt thickness was chosen to allow for interrogation of the sample surface to a depth at which both Si and Pt ware observable by XPS. Methylated Si surfaces were used to inhibit the formation of Si oxide at the Si/Pt interface during sample fabrication, because Si oxide of sufficient thickness is also capable of preventing silicide formation.[6] Figure 5A.7a shows the XP spectrum of a pure Pt phase. A thicker Pt layer (20 nm) was used to interrogate only the pure Pt phase. Figure 5A.7b shows the Pt 4f XP spectrum of CH_3-terminated Si with a 3 nm Pt overlayer. The Pt 4f peak shifted to higher binding energy, indicative of platinum silicide formation.[5] The shoulder of the peak at low binding energy is consistent with a pure Pt phase overlayer. Conversely, 3 nm of Pt on F-Gr covered silicon showed essentially no change in the Pt 4f binding energy immediately after fabrication (Figure 5A.7c or after a 1 h anneal under forming gas at 300 °C (Figure 5A.7d). The data are thus indicative of little or no platinum silicide formation. Figure 5A.7e presents an overlay of the spectra in Figure 5A.7a-5A.7d and highlights the difference between the Pt 4f peak positions.

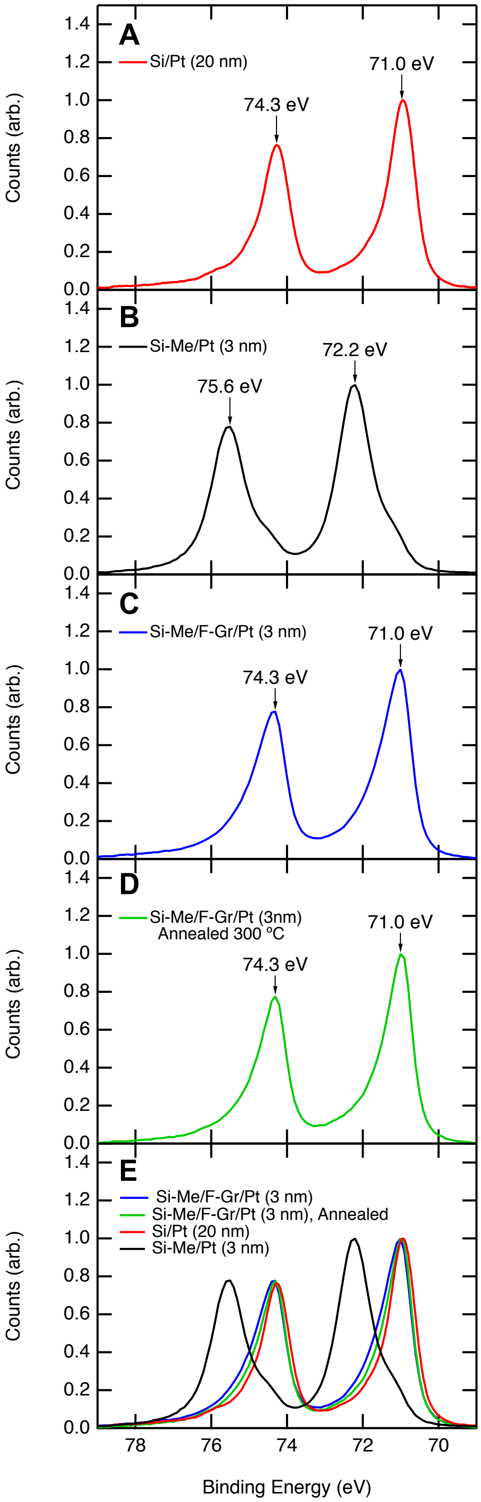

Figure 5A.7. The Pt 4f XP spectra of Pt on both F-Gr covered and Si surfaces. (A) XP spectrum of a thick (20 nm) layer of Pt on Si. This spectrum is representative of a pure Pt phase. (B) XP spectrum of a 3 nm layer of Pt on Si. The Pt 4f peak shifted to high binding energy (72.2 and 75.6 eV), characteristic of platinum silicide formation.[5] The shoulder to lower binding energy is attributed to a pure Pt phase. (C) XP spectrum of Si-Me/F-Gr/Pt (3 nm). The Pt 4f peak positions (71.0 and 74.3 eV) are consistent with pure Pt. (D) XP spectrum of Si-Me/F-Gr/Pt after annealing at 300 °C under forming gas. (E) Overlay of XP spectra (A)-(D).

5.2.6.7 n-Si/F–Gr non-aqueous photoelectrochemistry

Table S1. E_{oc} values for n-Si/Gr and n-Si/F–Gr electrodes in contact with non-aqueous redox couples under ~33 mW cm^{-2} of W-halogen illumination. The Nernstian potential, $E(\mathrm{A/A^{-}})$, of the contacting non-aqueous electrolytes were measured as follows: $E(\mathrm{CoCp_2}^{+/0}) = -1.26$ V vs. $E°'(\mathrm{Fc}^{+/0})$, $E(\mathrm{Fc}^{+/0}) = -0.1$ V vs. $E°'(\mathrm{Fc}^{0/+})$, $E(\mathrm{AcFc}^{+/0}) = +0.4$ V vs $E°'(\mathrm{Fc}^{+/0})$.

	$E_{\mathrm{oc,CoCp2+/0}}$ (V vs. $E(\mathrm{CoCp_2}^{+/0})$)	$E_{\mathrm{oc,Fc+/0}}$ (V vs. $E(\mathrm{Fc}^{+/0})$)	$E_{\mathrm{oc,AcFc+/0}}$ (V vs. $E(\mathrm{AcFc}^{+/0})$)
Gr	0	0.26	0.43
F–Gr	0	0.20	0.30

5.6.2.8 H-Br stability/efficiency over time

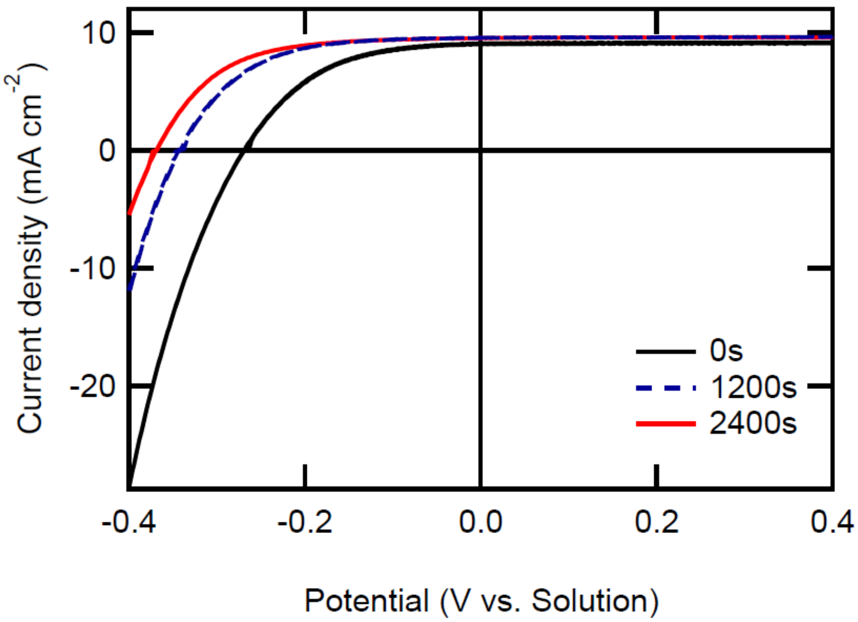

Figure 5A.8. Current density-potential (*J*-*E*) behavior of an n-Si/F-Gr/Pt photoanode before, during, and after 2400 s of photoelectrochemical stability testing in contact with 0.4M Br_2 - 7.0 M HBr (pH=0) aqueous electrolyte. Photoelectrochemical stability was measured by observing the *J*-*t* behavior at an initial current density of 10 mA cm^{-2} over the specified time period (see Figure 5.3). The behavior of the n-Si/F-Gr/Pt electrode improved over 2400 s, with improvements in E_{oc} (0.27 V to 0.37 V), J_{SC} (9.0 mA to 9.5 mA), and *ff* (0.51 to 0.59), resulting in an increase in the ideal regenerative cell conversion efficiency rom 3.5% to >5%.

5.6.2.9 XPS Oxide Analysis

XPS analysis was performed in order to determine the effect of electrochemical oxidation at the Si–Me surface on the oxidation state of the Si photoanode surface (Figure 5.2). Silicon oxide detected before and after electrochemical oxidation was quantified using a simple substrate—overlayer model described by equation 1:[7]

$$d = \lambda_{ov} \sin\theta \left\{ \ln\left[1 + \frac{I_{Si}^{o}}{I_{ov}^{o}} * \frac{I_{ov}}{I_{Si}}\right]\right\} \quad (1)$$

Where d is the overlayer thickness, λ_{ov} is the attenuation factor through the oxide overlayer (assumed to be 2.6 nm)[8], θ the angle from the surface of the sample to the detector (90°), $\frac{I_{Si}^{o}}{I_{ov}^{o}}$ is an instrument normalization factor related to the expected signal for a pure Si and a pure SiO_2 sample (taken to be 1.3 for this instrument), I_{ov} is the measured intensity of the silicon, and I_{ov} is the measured intensity of the silicon oxide overlayer. The thickness of a monolayer of oxide was taken to be 0.35 nm.[9] Negligible silicon oxide was detected on the bare methyl-terminated silicon surfaces prior to electrochemical oxidation (Figure 5.2a) and an oxide thickness of approximately 0.75 nm, or >2 monolayers of oxide, was observed after exposure of the Si–Me surface (Figure 5.2b) to the electrochemical oxidation conditions described in Figure 5.2. An oxide thickness of approximately 0.15±0.05 nm was detected on the Si–Me/F–Gr surfaces prior to electrochemical oxidation (Figure 5.2c) and an oxide thickness of approximately 0.17± 0.5 nm, was observed after exposure (Figure 5.2d) of the Si–Me/F–Gr surface to the electrochemical oxidation conditions described in Figure 5.2.

5.6.3 Appendix References

1. N. Petrone, C. R. Dean, I. Meric, A. M. van der Zande, P. Y. Huang, L. Wang, D. Muller, K. L. Shepard and J. Hone, *Nano Lett.*, 2012, **12**, 2751-2756.
2. A. Pirkle, J. Chan, A. Venugopal, D. Hinojos, C. W. Magnuson, S. McDonnell, L. Colombo, E. M. Vogel, R. S. Ruoff and R. M. Wallace, *Appl. Phys. Lett.*, 2011, **99**, -.
3. N. T. Plymale, Y.-G. Kim, M. P. Soriaga, B. S. Brunschwig and N. S. Lewis, *J. Phys. Chem. C*, 2015, **119**, 19847-19862.
4. R. Stine, W.-K. Lee, K. E. Whitener, J. T. Robinson and P. E. Sheehan, *Nano Lett.*, 2013, **13**, 4311-4316.
5. G. Larrieu, E. Dubois, X. Wallart, X. Baie and J. Katcki, *J. Appl. Phys.*, 2003, **94**, 7801.
6. J. R. Abelson, K. B. Kim, D. E. Mercer, C. R. Helms, R. Sinclair and T. W. Sigmon, *J. Appl. Phys.*, 1988, **63**, 689-692.
7. D. Briggs and M. P. Seah, *Practical Surface Analysis*, John Wiley & Sons Ltd, 2nd edn., 1990.
8. M. F. Hochella Jr and A. H. Carim, *Surface Science*, 1988, **197**, L260-L268.
9. J. A. Haber and N. S. Lewis, *J. Phys. Chem. B*, 2002, **106**, 3639-3656.

Chapter 6

Further Exploration of Graphene/Semiconductor Interfaces

6.1 Introduction and Background

Unlike the preceding chapters, which were presented in journal-like format insomuch as they covered a single topic, were composed of published data, and contained a single experimental description, this chapter is instead a collection of vignettes on topics that I explored but was unable to publish on prior to the completion of my doctoral degree. With this in mind, the sections that follow in this chapter are self-contained to the extent that it was reasonable to do so, including short, independent introduction, experimental, and discussion sections for each. Included topics in this chapter are:

- The effect of bilayer and trilayer graphene as protective layers for silicon surface protection
- The use of pristine monolayer graphene to prevent silicide formation
- The use of a home-built CVD to grow monolayer graphene
- The effect of different etch methods on the identity and concentration of impurities at the graphene/silicon interface
- The deposition of metal oxides on graphene surfaces using atomic layer deposition methods

6.2 Bilayer and trilayer graphene as protective layers for silicon surfaces

In chapter 4, pristine monolayer graphene is used as a protective coating to prevent the passivation of silicon surfaces in aqueous photoanodic conditions. However, this protective ability is clearly incomplete as noted by the lack of perfect stabilization over longer time periods as well as under high light intensity (~1 sun) conditions. We hypothesized that the reason for this imperfect stability is the polycrystalline nature of the CVD grown graphene as well as damage to the graphene coatings during transfer onto the silicon surface. For this reason, we proposed that a second or third layer of graphene transferred to the surface should make graphene more likely to cover any damaged or damage-prone sites on the graphene sheets below it and therefore translate to better stability. In order to test this hypothesis, we repeated the procedures described in chapter 4 with the modification that multiple sheets of graphene were transferred to the silicon electrodes prior to photoelectrochemical testing in aqueous electrolyte. The J-t behavior of mono-, bi-, and trilayer graphene under ~33 mW cm^{-2} illumination from an ENH bulb in aqueous 350 mM $Fe(CN)_6^{4-}$ – 50 mM $Fe(CN)_6^{3-}$ electrolyte is depicted in figures 6.1a-c.

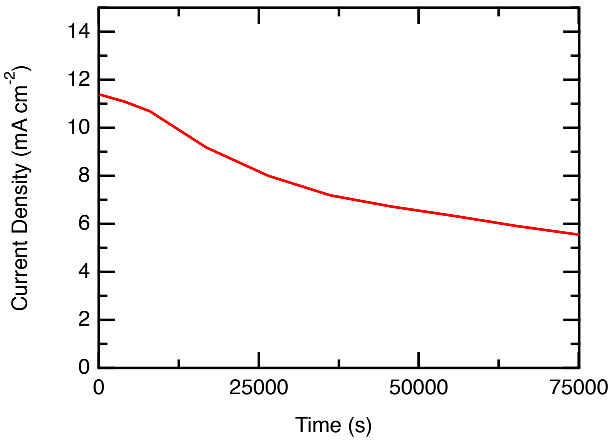

Figure 6.1a. J-t behavior of monolayer graphene-covered n-Si electrode in aqueous 350 mM $Fe(CN)_6^{4-}$ – 50 mM $Fe(CN)_6^{3-}$ electrolyte under ~33 mW cm^{-2} illumination from an ENH bulb. The loss of photocurrent over 75,000 s is suggestive of passivation of the silicon surface.

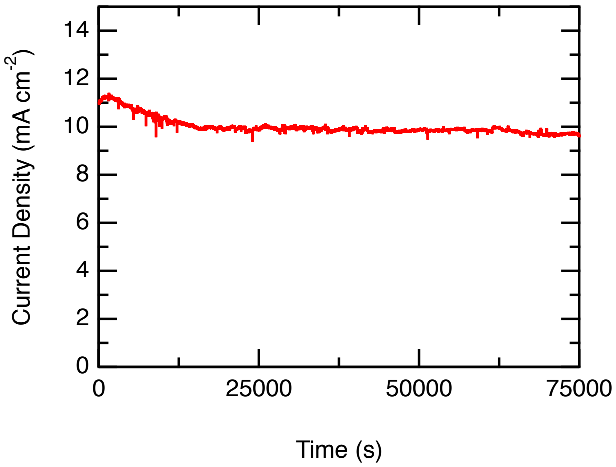

Figure 6.1b. J-t behavior of bilayer graphene-covered n-Si electrode in aqueous 350 mM $Fe(CN)_6^{4-}$ – 50 mM $Fe(CN)_6^{3-}$ electrolyte under ~33 mW cm^{-2} illumination from an ENH bulb. The stable photocurrent over 75,000 s is suggestive of a stable silicon surface.

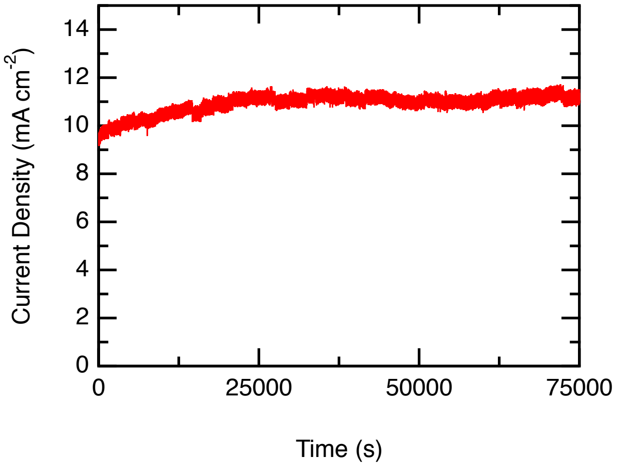

Figure 6.1c J-t behavior of trilayer graphene-covered n-Si electrode in aqueous 350 mM $Fe(CN)_6^{4-}$ – 50 mM $Fe(CN)_6^{3-}$ electrolyte under ~33 mW cm^{-2} illumination from an ENH bulb. The stable photocurrent over 75,000 s is suggestive of a stable silicon surface.

From the data in figures 6.1a-c, it appears that additional layers of graphene led to improved stability of the photocurrent when compared to monolayer graphene-covered silicon photoanodes. Additionally, the J-E behavior of trilayer graphene-covered np$^+$Si photoelectrodes was explored (figure 6.2).

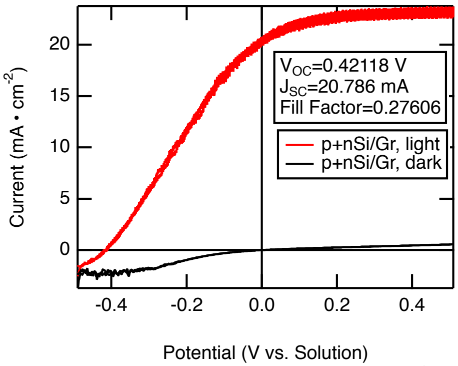

Figure 6.2. J-E behavior of a trilayer graphene-covered np$^+$Si photoelectrode in aqueous 350 mM $Fe(CN)_6^{4-}$ – 50 mM $Fe(CN)_6^{3-}$ electrolyte under ~1 sun illumination from an ENH bulb over 2 potential sweeps at 30 mV s^{-1}.

The data in figure 6.2 shows that the trilayer graphene imparts stability to graphene-covered Si photoanodes even under higher light intensity conditions and at higher current densities than those depicted in figure 6.1. The E_{oc} was consistent with bare np^+Si E_{oc} values and the fill factor was consistent with the fill factors for other graphene-covered silicon surfaces in aqueous 350 mM $Fe(CN)_6^{4-}$ – 50 mM $Fe(CN)_6^{3-}$ electrolyte.

These results are promising in suggesting that additional layers of graphene are useful in improving stability, but there are a number of questions that remain. While these results are interesting, I found it difficult to consistently reproduce these results. This may be because of weak adhesion between the graphene layers or because the additional transfer steps introduce additional damage to the graphene surface. Using as-grown multilayer graphene sheets to measure the protective ability of multiple layers of graphene would be a valuable experiment. Also, testing the stability of very small electrode areas would also be interesting insomuch as very small electrodes (<1 mm^2) would be less likely to include damaged or reaction-prone graphene sections that are the hypothesized 'weak points' in the protection scheme. Further, successfully obtaining consistent bilayer and trilayer graphene-covered silicon photoelectrodes would allow the examination of the energetics and electronics of the silicon/graphene interface.

6.3 Monolayer graphene to prevent silicide formation

In chapter 5, the ability to prevent the formation of platinum silicide during evaporation of platinum onto silicon surfaces was demonstrated with fluorinated graphene. Prior to this demonstration, similar experiments were undertaken using pristine monolayer graphene at the Pt/Si interface. Approximately 20 nm of Pt was deposited on monolayer graphene-covered n-Si and also on freshly HF etched n-Si. Each sample was loaded into a UHV chamber analyzed via XPS. Then, each sample treated with bombardment from an argon ion source. Using this sputtering method, a thin (~0.5 nm) section of the surface layer was removed, and the freshly exposed surface was analyzed via XPS. The hypothesis was that if graphene prevents silicide formation, depth profiling would indicate an abrupt junction and the absence of platinum silicide (PtSi) between the Pt and Si in the graphene-covered sample, but would indicate the presence of PtSi at the graphene-free junction. The results of this experiment are shown in in figures 6.3 and 6.4.

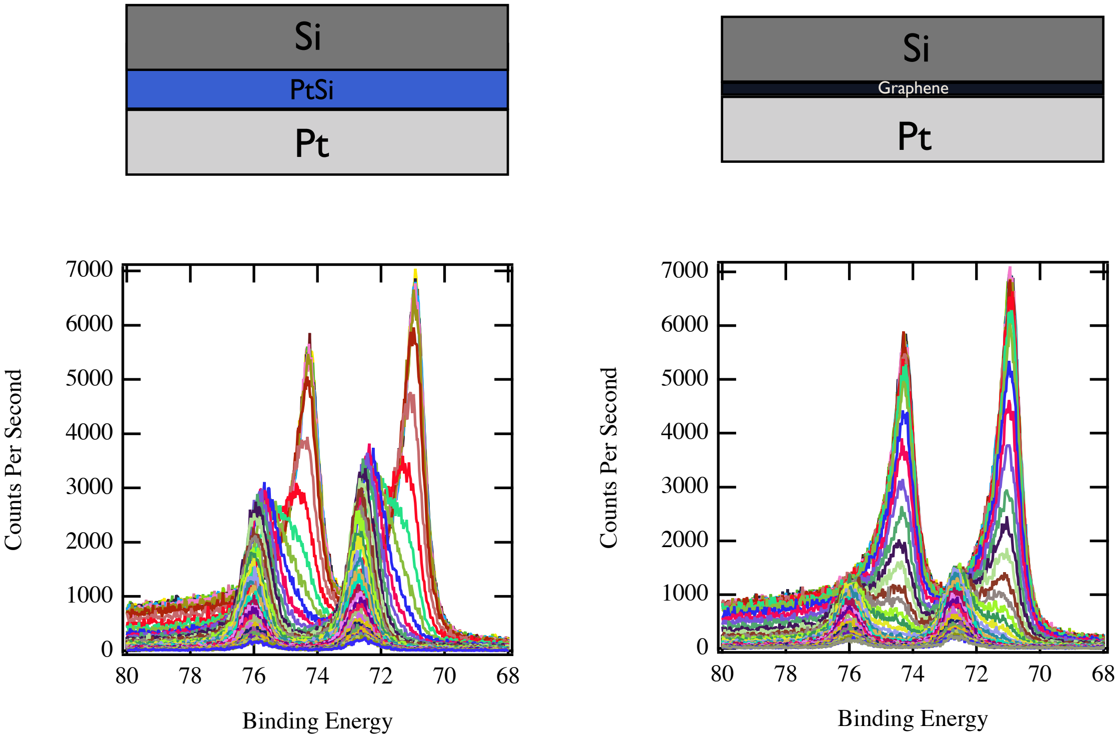

Figure 6.3 (bottom left) XP depth profiling spectrum of the Pt 4f region of an Pt/Si interface fabricated by Pt evaporation. The large peaks at 71 and 74 eV are indicative of a pure Pt species. The 71 eV and 74 eV peaks are the peaks early in the depth profiling and as the depth profile moves deeper into the sample, the Pt 4f doublet at 72 and 76 eV appears. Peaks at 72 and 76 eV are suggestive of a platinum silicide (PtSi).[1] (bottom right) XP depth profiling spectrum of the Pt 4f region of an Pt/Gr/Si interface fabricated by Pt evaporation. The large peaks at 71 and 74 eV are indicative of a pure Pt species. The 71 eV and 74 eV peaks are the peaks early in the depth profiling and as the depth profile moves deeper into the sample, the Pt 4f doublet at 72 and 76 eV appears. The PtSi peaks in this spectrum are smaller in ratio to the original Pt 4f doublet than the equivalent ratio in the graphene-free interface.

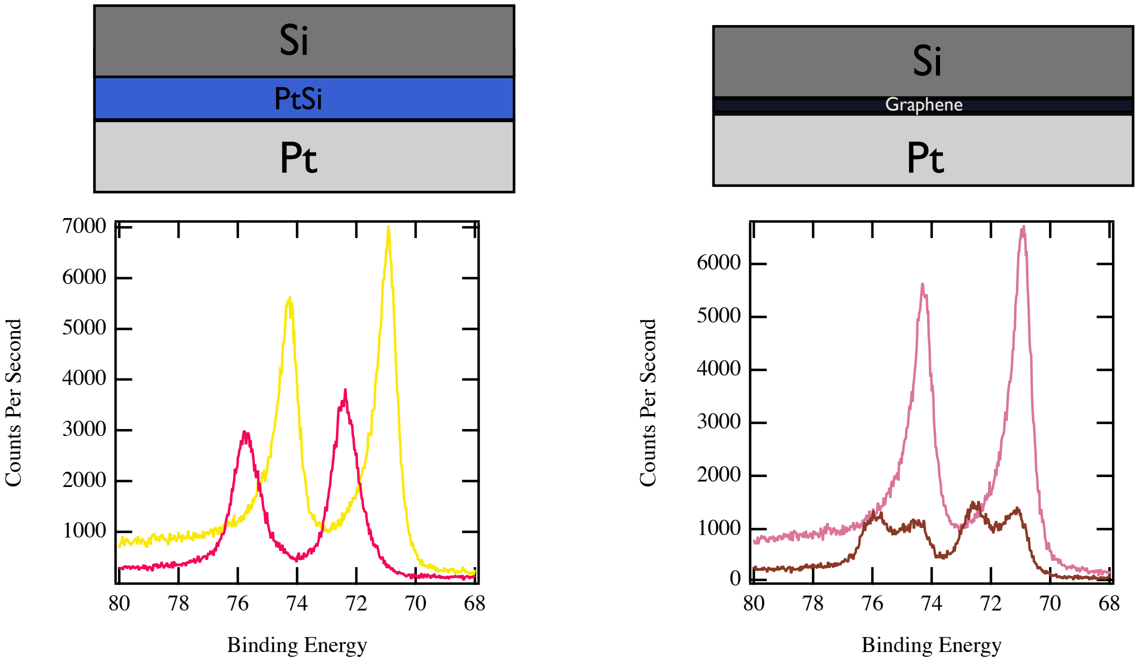

Figure 6.4. (bottom left) Representative Pt 4f XP spectra from the Pt/Si depth profiling experiment depicted in figure 6.3. The spectrum with large double at 71 and 74 eV is the pure Pt 4f phase after the initial sputtering step. The spectrum with the doublet at 72 and 76 eV is the PtSi phase at the point with the largest PtSi peak area. It is noted that there is no pure Pt phase in this spectrum, consistent with the formation of a pure silicide phase. (bottom right) Representative Pt 4f XP spectra from the Pt/Gr/Si depth profiling experiment depicted in figure 6.3. The spectrum with large double at 71 and 74 eV is the pure Pt 4f phase after the initial sputtering step. The spectrum with the doublet at 72 and 76 eV is the PtSi phase at the point with the largest PtSi peak area. At no point during depth profiling was a surface that had PtSi but no Pt phase present.

From the data in figures 6.3 and 6.4, it appears that graphene does prevent silicide formation to a certain extent based on the low ratio of PtSi to Pt peak area at the Pt/Gr/Si interface with respect to the PtSi to Pt peak area ratio in the graphene-free Pt/Si interface. It is not clear, however, whether it is capable of entirely preventing silicide formation as the XPS at the Pt/Gr/Si interface still indicates the presence of PtSi. The presence of the PtSi signal in the XP spectrum may also be the result of the high energy Ar^+ ions forcing Pt atoms past the graphene layer and forming PtSi via a knock-on effect of sputtering. In order to probe this possibility, the experimental procedure was modified. Instead of depositing 20 nm of Pt via evaporation, only ~3 nm of Pt was deposited. Because the sensitivity depth of the XPS instrument is approximately 8 nm, using a thin Pt layer allowed us to probe the Pt/Si and Pt/Gr/Si interface without need for depth profiling via sputtering. The experimental procedure was similar to that used to probe the ability of fluorinated graphene to prevent silicide formation described in chapter 5. Initially, two interfaces were compared: a Pt/Si-H interface where the Si sample had been etched in HF just prior to evaporation of Pt onto the surface, and a Pt/Gr/Si surface in which the Si had been etched in HF prior to graphene transfer to the Si surface (figure 6.5).

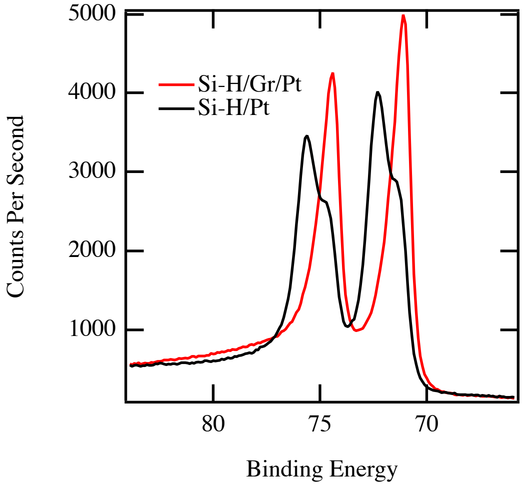

Figure 6.5. XP spectra of the Pt 4f region of Pt/Si-H and Pt/Gr/Si interfaces. The presence of two doublet sets of peaks in the Pt/Si-H interface spectrum as well as their peak positions (low binding energy doublet: 71 and 74 eV, high binding energy doublet: 72 and 76 eV), is consistent with formation of PtSi. The single set of doublet peaks in the Pt/Gr/Si interface spectrum is consistent with the inhibition of silicide formation.

The data in figure 6.5 suggests that pristine monolayer graphene does prevent silicide formation. However, silicon oxide layers are known to inhibit platinum silicide formation and the wet transfer methods used to transfer graphene to silicon are known to generate a thin oxide layer at the Si/Gr interface (chapter 4).[1, 2] The ability of thin layers of SiO_x to inhibit silicide formation was confirmed by taking a silicon sample, cleaning it with organic solvent (methanol, isopropanol, acetone), but not etching in HF prior to evaporation of Pt, giving a SiO_x/Pt interface. Figure 6.6 compares the XP spectra of SiO_x/Pt and Pt/Gr/Si interfaces.

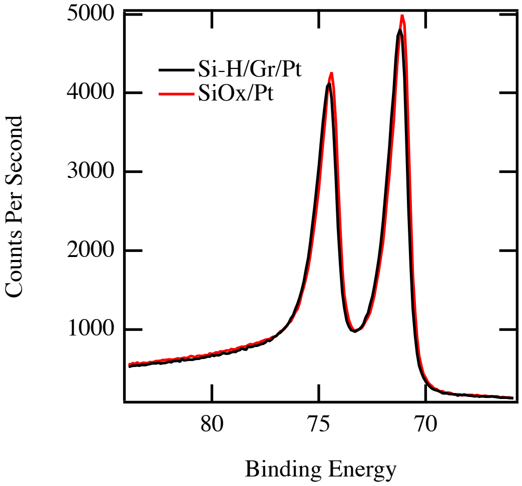

Figure 6.6. XP spectra of the Pt 4f regions of SiO_x/Pt and Pt/Gr/Si interfaces. In both spectra, the presence of a single doublet at 71 and 74 eV suggests that no PtSi phase was formed.

Because SiO_x was also effective at inhibiting PtSi formation, and it is known that SiO_x is present at the Gr/Si interface, it was no longer clear that graphene was the reason for the inhibition of PtSi formation at Pt/Gr/Si interfaces. In order to understand whether graphene was able to inhibit PtSi formation without the presence of a thin SiO_x layer, methylated Si (111) surfaces were employed. Unlike hydride-terminated surfaces, methylated silicon surfaces do not form a substantial oxide layer upon graphene transfer (chapter 5). Thus, the ability of Si-Me and Si-Me/Gr interfaces to prevent PtSi formation on evaporation of Pt onto the respective surfaces was probed via XPS (figure 6.7). This suggests that graphene does indeed inhibit silicide formation.

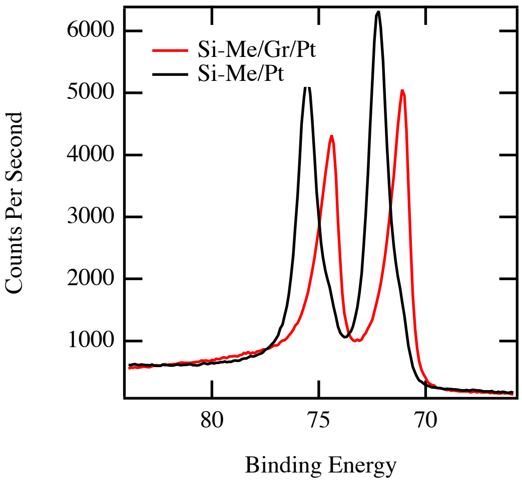

Figure 6.7. XP spectra of the Pt 4f region of Pt/Si-Me and Pt/Gr/Si-Me interfaces. The presence of two doublet sets of peaks in the Pt/Si-Me interface spectrum as well as their peak positions (low binding energy doublet: 71 and 74 eV, high binding energy doublet: 72 and 76 eV), is consistent with formation of PtSi. The single set of doublet peaks in the Pt/Gr/Si-Me interface spectrum is consistent with the inhibition of silicide formation.

Additional study of the generality of the ability of graphene to prevent Si/metal interactions should be explored, but I note here that some work in this vein has been done by other groups.[3-6] Study of the J-E behavior of these interfaces to understand the equilibrium energetics of the interface would constitute additional novel work.

6.4 Fabrication of graphene chemical vapor deposition (CVD) chamber and monolayer graphene growth

There has been an extensive effort by many research teams across the world to understand and improve graphene growth techniques.[7-10] While most of the CVD grown graphene used in this thesis was obtained from collaborators at Columbia University or purchased from ACS Materials Inc., we decided that it would be valuable to have our own graphene growth source in order to gain further control over the variables that may affect the results of our graphene based experiments. Thus, a home-built graphene chemical vapor deposition chamber was fabricated by Ron Grimm, Fan Yang, and myself (Figure 6.8).

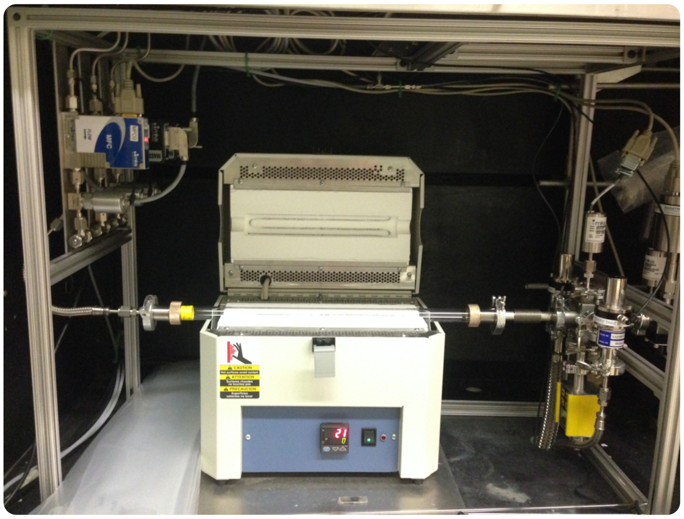

Figure 6.8. Home-built graphene CVD system (Toto). In the center of the image, the tube furnace and associated glass tube chamber are present. In the upper left, the MFCs used to control flow rates for Ar, H_2, and CH_4 can be observed. On the right, the pressure gauges can be seen.

The CVD system has a number of useful features, including the ability to attain pressures as low at 10^{-6} Torr and temperatures as high as 1100 ^{o}C. Flow rates for each gas are: CH_4 (0.3-200 sccm), H_2 (1-50 sccm) and argon (2-100 sccm). The ability to attain high temperature and low pressure make it useful in the graphene annealing steps noted in Chapters 4 and 5.

This home-built CVD system was used under a number of different conditions in order to grow monolayer graphene sheets. Using the conditions described in the appendix of chapter 4 and in Petrone, et. al, monolayer graphene was grown.[11] However, we desired to grow graphene with larger grain sizes. Following literature precedent, we lowered the CH_4 partial pressure during the initial phase of growth. This led to the graphene crystals observed via optical microscopy as seen in figure 6.9. Briefly, the recipe proceeded as follows: Cu foil was loaded into the growth chamber and the chamber was evacuated to <5x10^{-5} Torr. The chamber was then heated to 1000 ^{o}C while flowing 40 sccm H_2. After 30 minutes at 1000 ^{o}C, the H_2 flow rate was modified to 50 sccm and the CH_4 flow rate was set to 0.5 sccm while maintaining 1000 ^{o}C. This was the graphene growth. After one hour, the furnace was cooled quickly using a fan. During the cooling process, the flow rates used in the previous step were maintained (50 sccm H_2, 0.5 sccm CH_4) until the temperature reached <300 ^{o}C. Once the furnace was cooled below 300 ^{o}C, all flows were ceased and the furnace was allowed to cool to room temperature. Modifying this recipe to include a high flow rate CH_4 step (25 sccm H2, 100 sccm CH_4 at 1000 ^{o}C after the growth step noted above) led to continuous monolayer films with Raman spectra consistent with low defect, monolayer graphene (figures 6.10a, 6.10b).

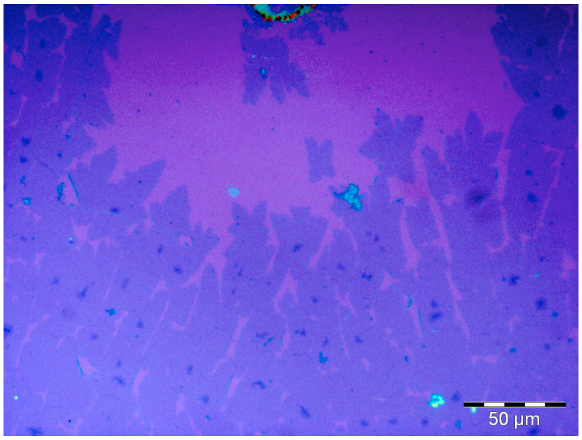

Figure 6.9. Optical image of graphene grown using a low CH_4 flow rate recipe. The grown graphene was transferred to 300nm SiO_2 using the PMMA transfer methods described in chapters 4 and 5. The large crystals visible in this image are suggestive of large (~50 µm on a side) single crystals of graphene. It is also clear that a continuous sheet of monolayer graphene was not formed during this growth.

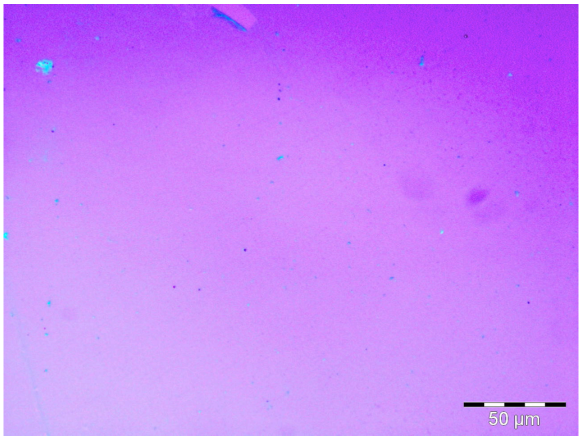

Figure 6.10a. Optical image of graphene grown using the modified low/high CH_4 flow rate recipe. The grown graphene was transferred to 300nm SiO_2 using the PMMA transfer methods described in chapters 4 and 5. A continuous sheet of monolayer graphene appears to be present. A small rip in the top center of the image gives contrast to highlight covered and uncovered sections of SiO_2. The Raman in figure 610.b confirms the monolayer nature of the graphene.

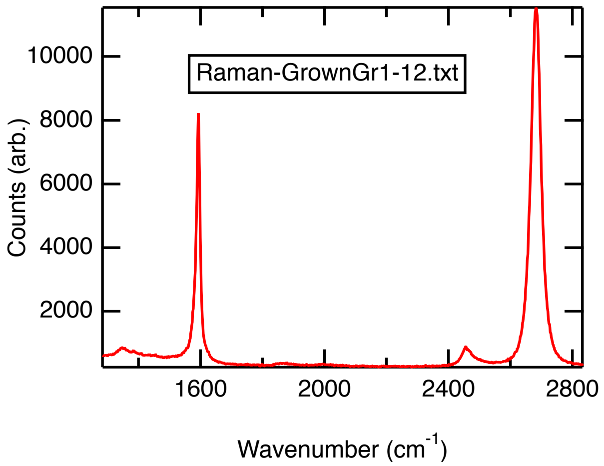

Figure 6.10b. Raman spectrum of graphene grown using the modified low/high CH_4 flow rate recipe. The grown graphene was transferred to 300nm SiO_2 using the PMMA transfer methods described in chapters 4 and 5. The large D/G peak ratio (~1350 cm^{-1} vs. 1580 cm^{-1} peaks) just low-defect graphene and the G/2D peak ratio (1580 cm^{-1} vs. 2680 cm^{-1}) suggest monolayer graphene.

The data in figures 6.9 and 6.10 suggest that the home-built graphene CVD is capable of producing high quality, continuous graphene sheets. Further study is needed to determine the consistency with which the CVD instrument produces high quality graphene. Assuming this can be determined, the ability to grow graphene with varying grain sizes in a polycrystalline sheet opens the possibility of correlating the ability of graphene to act as a protective layer with the grain size of the polycrystalline sheet. Additionally, bilayer and trilayer graphene should be growable as well, and can be used to compare the protective ability as well as the electronics of as-grown multilayer graphene sheets against protective ability and electronics of multilayer graphene sheets formed by multiple transfer processes.

6.5 Impurities at the graphene/silicon interface after different transfer procedures

A goal throughout this thesis was to understand how graphene and silicon interact in terms of the equilibrium energetics of the interface as well as the stability. One of the key challenges in probing this interface is the atomically thin nature of graphene. Because graphene is atomically thin and limited in electronic states, it is reasonable to assume that it is prone to transfer damage and susceptible to changes in electronic state or structure as a result of minute amounts of impurities. Compounding this problem is the fact that using CVD graphene requires that the graphene surface come in contact with a number of different chemicals from the etchants required to remove the copper foil, the polymer layer used to handle the graphene without the Cu foil, and residual Cu after etching. The focus of this section is to briefly understand the effects of modifying the transfer procedure on the graphene/silicon interface.

One of the most commonly employed etch steps to separate CVD-grown graphene from the copper growth substrate uses an aqueous $FeCl_3$ solution to oxidize the copper foil. Specifically, after graphene growth on the Cu foil, a PMMA layer was spincasted over the graphene layer, followed by a ~30 minute etch in $FeCl_3$ (aq), transfer of the resulting PMMA/Gr layer to three consecutive clean water baths. The H_2O washed PMMA/Gr layers were then transferred to the substrate of interest, baked at 80 ^oC for 10 minutes in air, followed by removal of PMMA by immersion in acetone, and finally an anneal under 95:5 Ar/H_2 gas for two hours (referred to the ‘standard’ transfer). This was also the most commonly employed etch step in this thesis. Common XP spectra of the resulting Gr/Si interface are depicted in figure 6.11 and an optical image of graphene transferred to 300 nm SiO_2/Si is shown in figure 6.12.

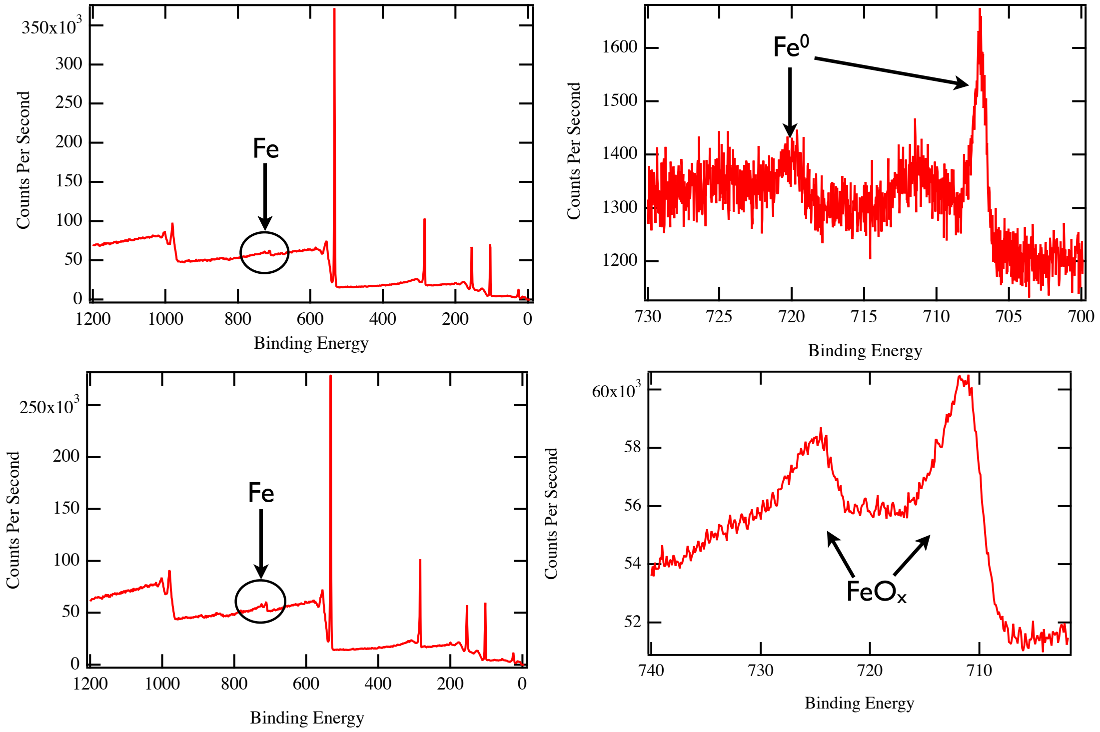

Figure 6.11. (Top left, bottom left) XP survey spectra of Gr/Si interfaces after the ‘standard’ transfer. The Fe 2p region of the survey spectra is highlighted. (Top right, bottom right). XP spectra of the Fe 2p region of the samples represented on the left. Both Fe^0 and FeO_x have been observed. Anecdotally, FeO_x is much more commonly observed that Fe^0.

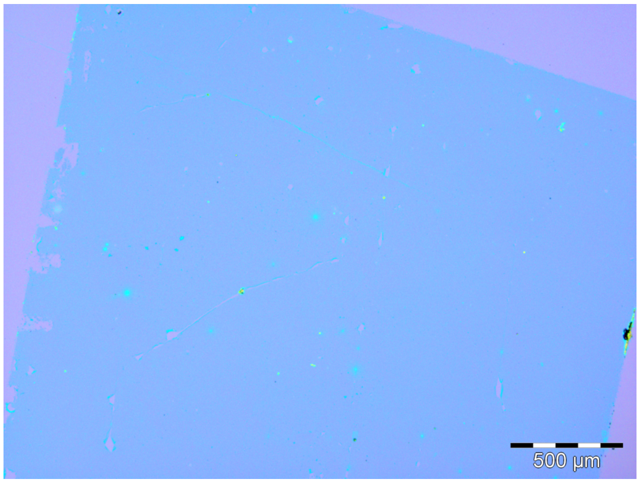

Figure 6.12. Optical microscopy image of graphene transferred to 300 nm SiO_2/Si using the 'standard' transfer method. The purple hue near the edges of the image are uncovered SiO_2.

From the data in figures 6.11 and 6.12, it is clear that the 'standard' transfer procedure results in graphene that is continuous on the scale of the substrate it is transferred to, but also that there are Fe impurities left at the surface. As these iron impurities are known to p-dope the graphene surface, we also explored another common etch technique that employs an aqueous ammonium persulfate (APS) solution instead of $FeCl_3$ to etch the Cu foil.[12, 13] The advantage in using APS is that because it is an organic oxidizer, it cannot leave metallic impurities at the Gr/Si interface, thus reducing the likelihood of doping of the graphene surface via an impurity left at the surface. Using the APS etching method, the XP spectrum of a Gr/Si interface in figure 6.13 was obtained. An optical image of a 300 nm SiO_2/Si interface is shown in figure 6.14.

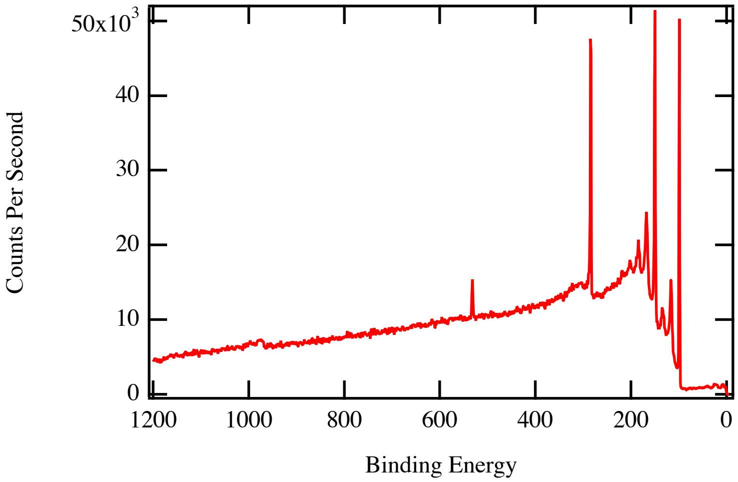

Figure 6.13 XP survey spectra of Gr/Si interfaces after the APS transfer.

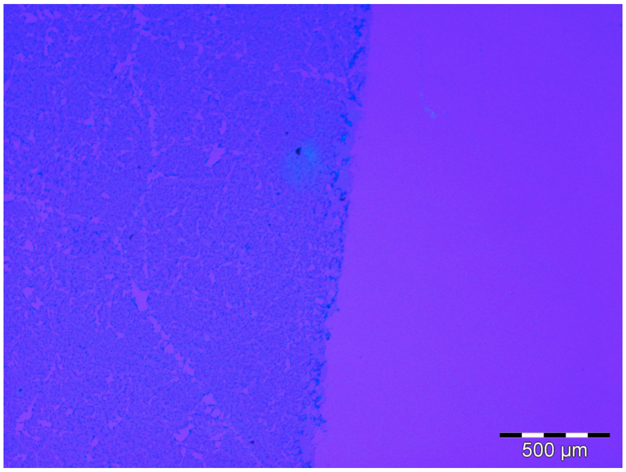

Figure 6.14. Optical microscopy image of graphene transferred to 300 nm SiO_2/Si using the APS transfer. The uncovered SiO_2 is predominantly on the right side of the image.

As seen figures 6.13 and 6.14, the APS transfer produces interfaces that are free of iron impurities, but the resulting graphene interface is heavily damaged. This has been attributed to interaction of the APS with the PMMA as APS is known to cross-link and thereby might cause the PMMA to strain the graphene as its morphology changes. It should be noted that APS has been reported as an etchant by other laboratories without reporting issues with cracked graphene.

In order to try and solve both the issues of removing Fe impurities while also ensuring transfer of a continuous layer of graphene, a 'modified $FeCl_3$' transfer procedure was explored. This procedure is outlined in scheme 6.1.

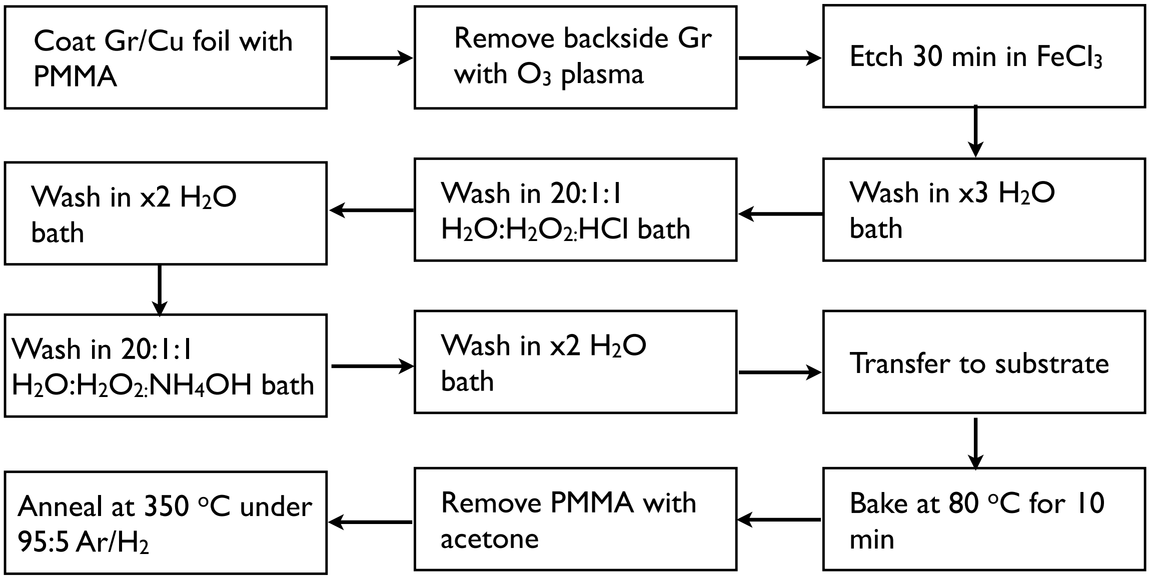

Scheme 6.1. 'Modified $FeCl_3$' transfer procedure. This procedure was modified from the procedure suggested by Liang, et. al.[12]

The rationale behind scheme 6.1 is the inclusion of dilute acidic and basic washes, akin to the well-known SC-1 and SC-2 clean procedures common in the semiconductor industry, to remove metallic impurities without damaging the graphene surface. The XP spectrum of the Gr/Si interface resulting from a ‘modified $FeCl_3$’ clean can be seen in figure 6.15 and an optical image of a 300 nm SiO_2/Si interface fabricated from a ‘modified $FeCl_3$’ is shown in figure 6.16.

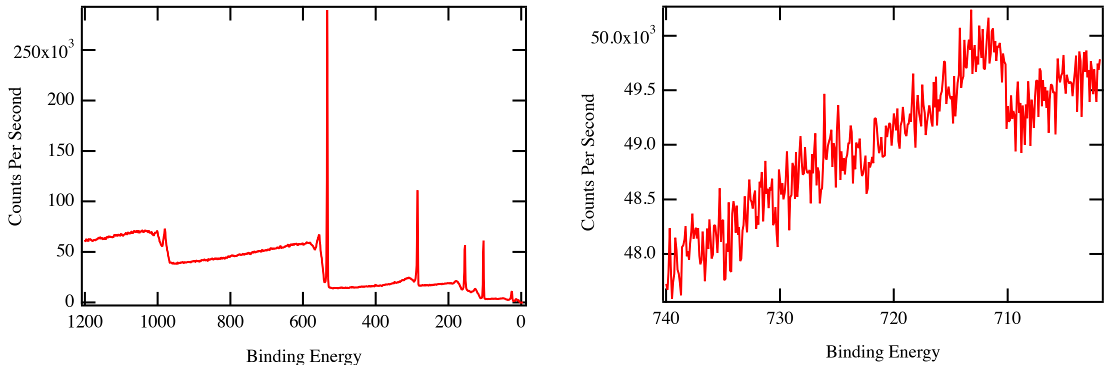

Figure 6.15. (left) XP survey spectra of Gr/Si interfaces after the ‘modified $FeCl_3$’ transfer. (right). XP spectra of the Fe 2p region of the samples represented on the left.

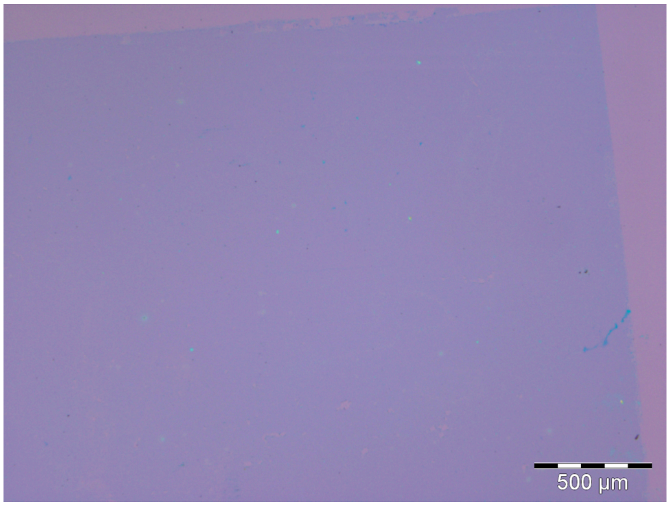

Figure 6.16. Optical microscopy image of graphene transferred to 300 nm SiO_2/Si using the 'modified $FeCl_3$' transfer method. The purple hue near the edges of the image are uncovered SiO_2.

From the data in figures 6.15 and 6.16, it is clear that the 'modified $FeCl_3$' transfer reduced the amount of Fe impurities at the Gr/Si interface with respect to the 'standard' transfer while also reducing the damage to the graphene surface with respect to the APS transfer method.

Transferring graphene to substrates cleanly while minimizing damage to the graphene itself is challenging and is an active area of research.[9, 10, 14, 15] With regards to future study of the Gr/Si interface, one should always take care to ensure that their graphene is transferring cleanly and without damage by utilizing XPS, Raman spectroscopy, and optical microscopy, particularly when CVD graphene is being employed. Many of the issues that one hopes to avoid (damage to the surface, unintended impurities) can be avoided through the use of single crystal graphene flakes obtained via micromechanical cleavage of an HOPG surface. While using single crystal graphene flakes is advantageous for the reasons noted above, it has the disadvantage of being significantly more challenging to obtain and manipulate said flakes, and it limits the size of the interface to the size of obtainable single graphene flakes, which can often be below 100 μm^2. That said, using single crystal graphene flakes to understand the inherent properties of the Gr/Si interface in tandem with CVD graphene to understand how the impurities left by the graphene transfer methods affect the Gr/Si chemical and electrochemical behavior on large scale interfaces is a promising future venue for this work.

6.6 ALD deposition on monolayer graphene

ALD deposition of metal oxides on pristine graphene surfaces has been demonstrated with a number of metals, including platinum, hafnium, and aluminum.[16-18] Without additional treatment, deposition is generally observed at defects in pristine graphene sheets, as these sites provide reactive centers to seed metal oxide growth.[18] This makes ALD deposition of graphene an interesting candidate method for 'sealing' the defective sites that may be the source of failure in graphene-based protective coatings. In order to test the hypothesis that ALD coatings may cover defect sites on graphene and improve the ability of the modified graphene to prevent passivation at silicon surfaces, I exposed monolayer graphene on Cu foil to the following ALD experimental procedure: The Gr/Cu foil was placed in the center of the reaction chamber, and the chamber was evacuated with a rotary vane pump. A valve connecting the reaction chamber to a TDMAT [tetrakis(dimethylamido)titanium] vapor source (source heated to 75 ^{o}C) was opened for 0.1 seconds. After a 15 second wait time, a valve connecting the reaction chamber to an H_2O source (source at room temperature) was opened for 0.015 seconds. This was followed by another 15 second wait time. The process of pulsing in TDMAT followed by H_2O was repeated for 22 cycles. We assumed this would produce approximately 1 nm of TiO_2 near reaction sites, as previous work in the group suggested that 5 nm TiO_2 was observed after 100 cycles. Analysis of the XP spectrum of the resulting Gr/Cu foil suggested that TiO_2 was deposited on the graphene surface (Figure 6.17).

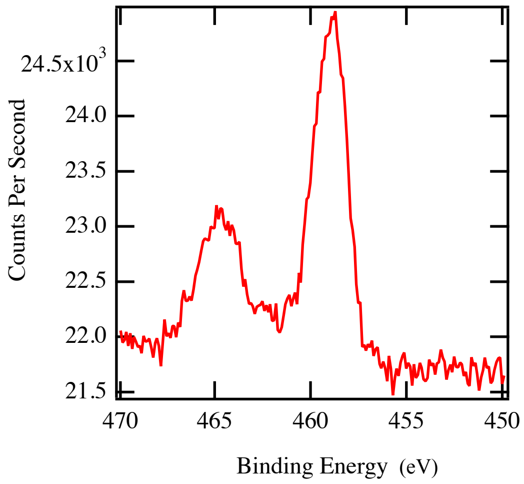

Figure 6.17. XP spectrum of the Ti 2p region of a Gr/Cu foil after exposure to ALD conditions. The presence of measureable Ti 2p counts at 459 and 464 eV suggests that the ALD method was successful at depositing TiO_2 on the graphene surface

Using the transfer methods described in Chapters and 5, the TiO_2 modified graphene was transferred to moderately doped n-Si and tested photoelectrochemically in aqueous 350 mM $Fe(CN)_6^{4-}$ – 50 mM $Fe(CN)_6^{3-}$ electrolyte for photoactivity and stability (Figure 6.18, Figure 6.19)

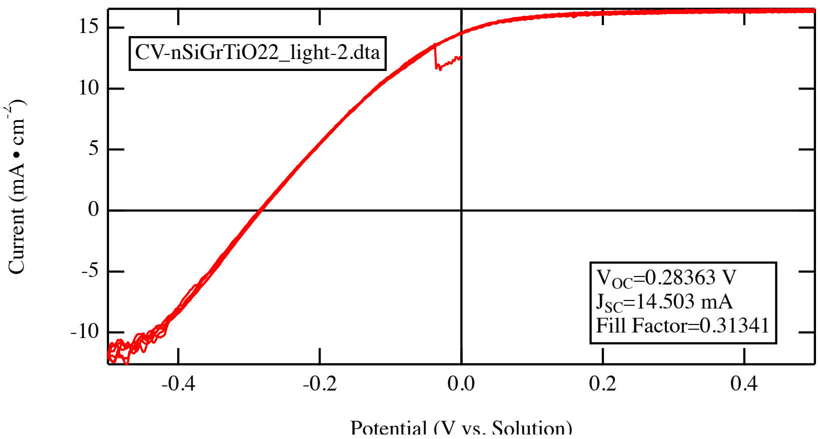

Figure 6.18. J-E behavior of ALD TiO_2 modified-graphene covering n-Si electrode in aqueous 350 mM $Fe(CN)_6^{4-}$ – 50 mM $Fe(CN)_6^{3-}$ electrolyte over 3 potential sweeps at 30 mV s^{-1} under ~33 mW cm^{-2} illumination from an ENH lamp.

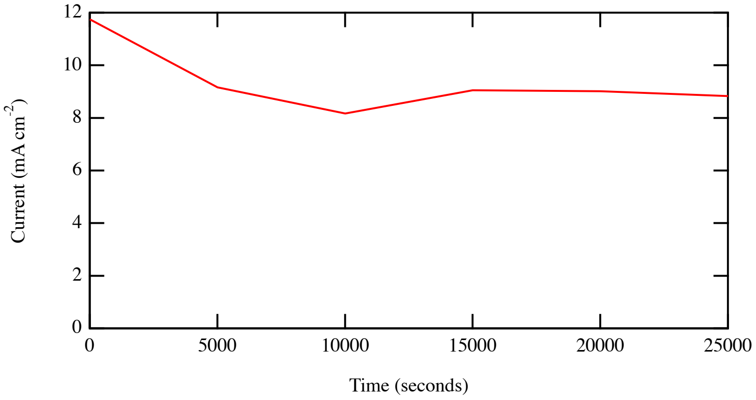

Figure 6.19. J-t behavior of ALD TiO_2 modified-graphene covering n-Si electrode in aqueous 350 mM $Fe(CN)_6^{4-}$ – 50 mM $Fe(CN)_6^{3-}$ electrolyte over 25,000 s under ~33 mW cm^{-2} illumination from an ENH lamp.

The data in figures 6.18 and 6.19 suggest that the TiO_2 does not destroy the photoactivity of the Si/Gr/electrolyte interface. Without additional experimentation and trials, it is yet unclear whether the TiO_2 improves the stability of this interface, but it does not prevent stability from being observed. Future work in this area should explore whether other metals are compatible with the ALD deposition method (XPS), explore whether the metals are deposited uniformly or at defect sites (SEM, AFM), and determine whether the deposition improves the ability of the graphene protective coating to inhibit deleterious reactions at semiconductor surfaces (electrochemistry, XPS). Additionally, the presence of graphene at the semiconductor surface could be used to probe the effect of preventing a $SiTiO_x$ or SiO_x interface from forming at Si/TiO_2 junctions that have been recently studied in our group.[19]

6.7 Conclusion

Graphene can be used for a myriad of purposes.[20-24] In this chapter, and in this thesis, I have explored just a small number of these purposes as they relate to the graphene/silicon interface under photoelectrochemical conditions. The key to understanding how graphene interacts with silicon under these conditions is to be fastidiously careful in device fabrication and to demand consistency in results. While I regret that I was not always able to live up to these rigorous standards, I believe time and effort will reveal the true nature of this interface, and I hope that in some small way I have helped lay the groundwork for future scientists to continue exploring this field.

6.8 References

1. G. Larrieu, E. Dubois, X. Wallart, X. Baie and J. Katcki, *J. Appl. Phys.*, 2003, **94**, 7801.
2. A. C. Nielander, M. J. Bierman, N. Petrone, N. C. Strandwitz, S. Ardo, F. Yang, J. Hone and N. S. Lewis, *J. Am. Chem. Soc.*, 2013, **135**, 17246-17249.
3. S.-h. C. Baek, Y.-J. Seo, J. G. Oh, M. G. Albert Park, J. H. Bong, S. J. Yoon, M. Seo, S.-y. Park, B.-G. Park and S.-H. Lee, *Appl. Phys. Lett.*, 2014, **105**, -.
4. X. Liu, X. W. Zhang, Z. G. Yin, J. H. Meng, H. L. Gao, L. Q. Zhang, Y. J. Zhao and H. L. Wang, *Appl. Phys. Lett.*, 2014, **105**, -.
5. W. K. Morrow, B. P. Gila and S. J. Pearton, *ECS Transactions*, 2014, **61**, 371-379.
6. W. Luo, W. H. Doh, Y. T. Law, F. Aweke, A. Ksiazek-Sobieszek, A. Sobieszek, L. Salamacha, K. Skrzypiec, F. Le Normand, A. Machocki and S. Zafeiratos, *J. Phys. Chem. Lett.*, 2014, **5**, 1837-1844.
7. C. Mattevi, H. Kim and M. Chhowalla, *Journal of Materials Chemistry*, 2011, **21**, 3324-3334.
8. J.-H. Lee, E. K. Lee, W.-J. Joo, Y. Jang, B.-S. Kim, J. Y. Lim, S.-H. Choi, S. J. Ahn, J. R. Ahn, M.-H. Park, C.-W. Yang, B. L. Choi, S.-W. Hwang and D. Whang, *Science*, 2014, DOI: 10.1126/science.1252268.
9. X. Li, W. Cai, J. An, S. Kim, J. Nah, D. Yang, R. Piner, A. Velamakanni, I. Jung, E. Tutuc, S. K. Banerjee, L. Colombo and R. S. Ruoff, *Science*, 2009, **324**, 1312-1314.

10. X. Li, C. W. Magnuson, A. Venugopal, R. M. Tromp, J. B. Hannon, E. M. Vogel, L. Colombo and R. S. Ruoff, *J. Am. Chem. Soc.*, 2011, **133**, 2816-2819.

11. N. Petrone, C. R. Dean, I. Meric, A. M. van der Zande, P. Y. Huang, L. Wang, D. Muller, K. L. Shepard and J. Hone, *Nano Lett.*, 2012, **12**, 2751-2756.

12. X. Liang, B. A. Sperling, I. Calizo, G. Cheng, C. A. Hacker, Q. Zhang, Y. Obeng, K. Yan, H. Peng, Q. Li, X. Zhu, H. Yuan, A. R. Hight Walker, Z. Liu, L.-m. Peng and C. A. Richter, *ACS Nano*, 2011, **5**, 9144-9153.

13. A. Pirkle, J. Chan, A. Venugopal, D. Hinojos, C. W. Magnuson, S. McDonnell, L. Colombo, E. M. Vogel, R. S. Ruoff and R. M. Wallace, *Appl. Phys. Lett.*, 2011, **99**, -.

14. Y. Huang, E. Sutter, N. N. Shi, J. Zheng, T. Yang, D. Englund, H.-J. Gao and P. Sutter, *ACS Nano*, 2015, DOI: 10.1021/acsnano.5b04258.

15. H. Choi, J. Y. Kim, H. Y. Jeong, C.-G. Choi and S.-Y. Choi, *Carbon Letters*, 2012, **13**, 44-47.

16. K. Kim, H.-B.-R. Lee, R. W. Johnson, J. T. Tanskanen, N. Liu, M.-G. Kim, C. Pang, C. Ahn, S. F. Bent and Z. Bao, *Nat Commun*, 2014, **5**.

17. S. C. O’Hern, D. Jang, S. Bose, J.-C. Idrobo, Y. Song, T. Laoui, J. Kong and R. Karnik, *Nano Lett.*, 2015, **15**, 3254-3260.

18. X. Wang, S. M. Tabakman and H. Dai, *J. Am. Chem. Soc.*, 2008, **130**, 8152-8153.

19. S. Hu, M. R. Shaner, J. A. Beardslee, M. Lichterman, B. S. Brunschwig and N. S. Lewis, *Science*, 2014, **344**, 1005-1009.

20. K. S. Novoselov, V. I. Falko, L. Colombo, P. R. Gellert, M. G. Schwab and K. Kim, *Nature*, 2012, **490**, 192-200.

21. D. A. C. Brownson, D. K. Kampouris and C. E. Banks, *Chemical Society Reviews*, 2012, **41**, 6944-6976.

22. F. Schwierz, *Nat Nano*, 2010, **5**, 487-496.

23. S. Navalon, A. Dhakshinamoorthy, M. Alvaro and H. Garcia, *Chem. Rev.*, 2014, **114**, 6179-6212.

24. V. Georgakilas, M. Otyepka, A. B. Bourlinos, V. Chandra, N. Kim, K. C. Kemp, P. Hobza, R. Zboril and K. S. Kim, *Chem. Rev.*, 2012, **112**, 6156-6214.

About the Author

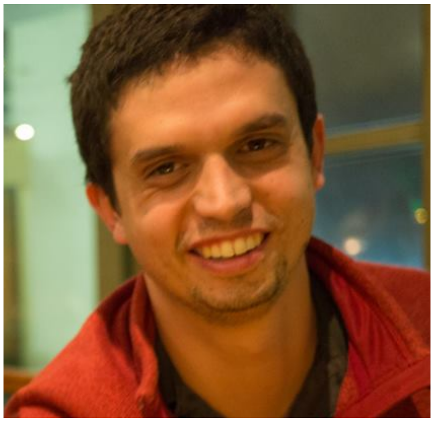

Adam Christopher Milan Nielander was born in Lafayette, Indiana on June 3, 1987 to Kimberly Ann Nunley and James Ralph Nielander. He was raised in Roanoke, Virginia with his younger sister, Caroline Ruth Nielander, and attended Cave Spring High School. After high school, he matriculated at the University of Virginia, and studied inorganic chemistry under the mentorship of Prof. W. Dean Harman. He obtained a B.S. and M.S. in Chemistry (2010) and moved to Pasadena, CA to attend the California Institute of Technology. He obtained his Ph.D. in 2016 after five years of study in the laboratory of Prof. Nathan S. Lewis. During this time he managed to achieve his true goal of securing free travel, including trips to Boston, San Francisco, Honolulu, and Berlin. Adam's interests include but are not limited to: playing tennis and basketball, spending time with and training his dog Grover, exploring Pasadena and Southern California, studying American history and energy sources, and rooting for the Ravens and Orioles.